Some Effects of Gas-induced Fluidization in Dry Granular Media

by
Anders Nermoen
Physics of Geological Processes
Department of Physics
University of Oslo
Norway

Thesis submitted for the degree
Philosophia doctor

June 2010

Series of dissertations submitted to the
Faculty of Mathematics and Natural Sciences, University of Oslo
No. 1003

ISSN 1501-7710

Cover: Inger Sandved Anfinsen.
Printed in Norway: AiT e-dit AS.

Produced in co-operation with Unipub.
The thesis is produced by Unipub merely in connection with the
thesis defence. Kindly direct all inquiries regarding the thesis to the copyright
holder or the unit which grants the doctorate.

Acknowledgement I thank my main supervisor Dag Dysthe for being an important discussion partner, teacher and mentor through my last years here on *Physics of Geological Processes* (PGP). I want to thank Adriano Mazzini for taking me to two field trips, the Lusi mud volcano on Java, Indonesia and the Salton Sea in California, USA. I thank my office partners, Espen Jettestuen and Simon Daniel deVilliers for always being helpful, supportive and open for discussions.

I thank Olivier Galland for sharing his inspiration and knowledge through discussions, experimental collaboration, and advices on writing. I wish to thank Christophe Raufaste and Joachim Mathiesen for all the co-operation and interesting discussions. I thank Anders Malthe-Sørenssen and Jens Feder for providing the funding of my initial phd-project. I thank Yuri Podladchikov for being a whole hearted teacher, always willing to share knowledge and ideas and his end-less belief in students. Thank you for your generosity!

I want to thank Galen Gisler for always being so positive, helpful and supportive throughout my period here on PGP. In addition I want to thank both Torstein Jøssang and Karin Brastad for their positiveness and cheerful spirits, cheering up me and the community. I thank Olav Gundersen for the help in the laboratory such that ideas could manifested themselves as running experiments. I want to thank Paul Meakin for interesting discussions and advices on writing.

I thank all my other discussion partners, friends and colleagues here on PGP and University of Oslo. In danger of forgetting someone, my thanks goes to Jostein R. Kristiansen, Torbjørn Bjørk, Anja Røyne, Karen Mair, Luiza Angheluta, Jan Ludvig Vinningland, Filip Nicolaisen, Bjørn Jamtveit, Øyvind Hammer, Henrik Svensen and of course the "wednesday club" (you know who you are). I am truly grateful for all the knowledge and friendliness you so generously have shared.

It has been a privilege for me to follow the paths that I have felt being right during my time here on PGP. Both for the good and bad that comes with it,- I could follow my ideas. I have not been bound to any specific, fixed project nor any particular persons such that I could chose my collaborators, and my collaborators have chosen me. This freedom is sometimes difficult to tackle. Every so often I have doubted my self. In some cases, all I had to rely on was my stomach-feeling when decisions had to be made. It is for certain that the freedom and the responsibility that comes with it has taught me a lot, on levels beyond the pure scientific method, during my time here. Along with freedom and responsibility a feeling of being on 'deep water' often has stroke me. I once said that taking this phd feels like being pushed off a tall cliff, with four years to learn how to fly.

Despite that, having freedom as a phd-student is something I wish others could have too. It has benefited me, and I am certain it could benefit others.

Early in life I started to think about, and question, what surrounded me. In the beginning, as a kid, I thought that I might as well could start out with the big things: Is there a God? Where do we come from? And, what is the history and the final destiny of the Earth and the Universe?

Extremely interesting questions. Quickly I figured out that mysticism, including religion, brought *nothing* of particular interest to the table. Then I thought that maybe philosophy was the thing for me. After taking the introductory course it seemed that philosophers were more concerned on 'semantic constructions' and 'the masculine objects in the drama of Henrik Ibsen', than

worrying about what really takes place out there in the dirty old world. Then I decided that physics could be a field best addressing the issues of my interest.

Studying physics has until now been both inspiring, interesting and fun, but also very challenging. During the studies my taste for questions changed[1]. I learned that asking correct questions are as important as the answers to the questions posed by others. The questions in life became more directed, with a clearer focus and with time more down to Earth.

Since I am present here on Earth it felt (and still feels) relevant to know something about this place on which I am living. I figured out that maybe PGP was the thing for me, so in January 2005 I started doing my master thesis here.

During my time here on PGP my attention and interest has been drawn more to the physics that surrounds us. We are *surrounded* by physics. Physics is important to humans in several ways, both culturally (e.g. to understand ourselves and our position in the universe), and technologically (e.g. to address how to improve our living conditions). My interest has been pulled towards the great variety of patterns, shapes and forms in Nature.

It is not a single day in which I do not think about, and let myself get fascinated by, the everyday patterns formed in front of my eyes. The patterns are out there. With a small *attention push* you can learn to open your eyes,- you will be fascinated! I have found this view-point enormously stimulating and inspiring. My most recent questions have therefore changed to: Which mechanism forms this fluvial pattern? How can such a cool dendritic pattern form when water freeze? How can it be that when water flows on the pavement it flows downward in such a step-like manner? Why does snow-flakes take form as they do? What is the origin of all the beautiful stripes, dots and waves around us? What can the pattern formed by map lichen on a rock tell us? How can they be understood? To my astonishment, these questions can actually be answered.

During my life the 'big' questions has changed. By analogy, I guess that they would change in the future too. Until then I happily observe the fabulous natural things surrounding me. This is a gift from PGP that I take with me further in life. This was so clearly formulated by Arne Næss in Morgenkåseriet (24/6 - 2009). I hope you read his words on "Patterns in nature - a philosophers view", translated to you on the following pages.

In the end I will give my greatest thanks to my parents, Allic and Bjørn, and to my siblings, Frøydis, Marius and Jonas. You have always supported me, helped me and believed in me. When that being said, I want to thank all of those who have believed and put their faith in me over the years! I want to quote the famous Norwegian fiddle player Knut Buen saying that: *"Den stysste gåva du kan gje dine medmenniskje' e true på dei!"*[2] When you so often doubt yourself, it is the faith of the others in you that brings you further!

Anders Nermoen
June 2010

[1] I do not know if it is because I gave up on the big questions or what. I realized that even physics could not tell me if God existed or not. Although, at the time of writing I find it highly improbable on the basis of the presented evidences, that any supernatural God can exist.

[2] English: *"The greatest gift you can give the people around you, is your belief in them!"*

Supervisors:
Dag Kristian Dysthe
Anders Malthe-Sørenssen
Yuri Podladchikov
Espen Jettstuen
Olivier Galland

Patterns in nature - a philosophers view

I came across this radio interview with Arne Næss (d. 2008) (in Morgenkåseriet 24/6-2009) where he was elaborating on what it means to be a human and how to live a good life. The moment I heard him, his words hit me, and I found his words both inspiring and meaningful. I translated his insights into English and share them here. His words were:

Today I wish to talk about bringing joy and gladness to life.

I think that all human beings want to be glad, or want to contribute in such a way that others can be glad. Unfortunately, quite often gladness seems both distant and unavailable. For many people gladness is something that others have. They think that they don't posses what is needed to experience real joy. They think that in their particular situation gladness or joy is not available. I've been thinking quite a lot about this, and found that it is more often (than not) our attitude that limits the availability of happiness. We are **too pretentious**.

We forget that joy and happiness is easily available. People tend to think that this is a strange attitude. It conflicts with their opinion on what joy really is. Joy and happiness is often considered to be something spectacular not occurring in the everyday life. The release of great, emotional, happy feelings should only be triggered by something grand, we think. The question is then, are you certain about this? Have you considered the little things right in front of you? Have you smelled the flowers or played with droplets of rain? Have you immersed yourself into the colours and shapes of a pattern? Have you allowed the senses to sink into the tinyest details? Think of the snow covering the landscape a winter day. Think of the waves washing onto the shore of the beach. Stop, take time, and look at things you are stepping on, look at the clouds and look at the trees.

Let us look at the waves together. You might say, this is completely normal waves flushing on shore,- what is the big deal? Then I laugh and answer,- completely normal waves? No no - look again, look closely at that specific wave. Look how it changes and develops. First it comes in breaking before it flows back out into the ocean again. Soon you will discover details in its movement and in its shapes, you will see how the waves reflects the sun and sky in all different kinds of ways. It is fabolous, isn't it? Fabolous that such form and movement occurs in nature! If you get there, you will, just like me, never again be bored. You will experience how the joy grows the more you percieve. You will understand that you will always have something that will enchant you. Neither age nor bad health can take the wavy-feeling away! There is no-one asking for

an entry ticket, and you will never think again that the little things only can bring you little joys. As a kid I could sit for hours and percieve the waves in my bath-tub or the tiny creatures in the grass. Children do only need a tiny 'attention-push' and they will become experts in experiencing the world around them. Soon they may see more than the grown ups and they need not to ask their parents to bring them experiences. Life is so full of wonders and oddness,- and full of joy!

In our culture we are too worried and conserned about what we don't posses. We have forgotten the miracles and wonders in what we think of as common, the everyday life. There is an underlying critique in what I have spoken of today. A critique of the culture in which we are living. In my opinion we fail to develop ourselves as human beings. We fail to develop our senses, our fantasy, and by that we become less human. When this attitude contaminates our work, our relation other people and to society, danger is near. Inhumanity may arise.

This was all I wanted to say, remember the joy is nearby, available and right in front of our eyes. It only waits for you to wake it up!"

Arne Næss
Morgenkåseriet, NRK P2
24/6 - 2009

Contents

A brief summary

The main body of this thesis consists of three papers in which aspects of fluid induced deformation in granular materials are studied. Insight from experiments, dimensional analysis, numerical modeling and analytic predictions are combined to interpret observations various aspects of piercement structures in the geological record. A fourth paper is included showing how analogue modeling has been used to understand a geological processes.

Paper 1 presents experimental work on the segregation pattern forming in partially fluidized, bi-modal sized granular mixtures. The experiments are performed on a vertically oriented Hele-Shaw cell (HS-cell), the narrow box between two parallel glass plates, filled with glass beads. Gas flow is imparted through the bottom of the bed causing fluidization[3] when the system is driven at velocities exceeding a critical limit. The co-existence of fluidized and static zones is termed partial fluidization and occurs when the imposed gas flux is insufficient to fluidize the whole system. Within the fluidized zones, the particles re-organize and the large particles sediment down while the small particles remains fluidized. The re-organization is caused by differences in the ratio of the weight to the viscous drag. A pipe-like pattern develops due to a feedback mechanism in which the flow is focused through domains dominated by large particles. The focusing of the flow localizes the fluidization, which in turn enables the sedimentation of the large grains [1].

Paper 2 presents an experimental and analytical study of the critical conditions for fluidization of a dry granular material. Based on the experiments, we find that the critical velocity of fluidization scales almost linear with the ratio of the filling height to the inlet width. An analytic model for the pressure field is obtained by solving the Laplace equation for the velocity boundary conditions given by the geometry of the experimental setup. By integrating the vertical component of the pressure gradient within a truncated wedge we estimate the total drag. A balance between the integrated seepage force and the weight of the truncated wedge, gives an analytic estimate of the imposed critical velocity. We found that the critical velocity attained a linear scaling with the sediment height to inlet width ratio, but slightly under-estimated the experimentally obtained values [2].

Paper 3 focus on the relation between the localization of tectonic stresses and the critical condition for fluidization. In this study we present a model for the causal relation between localization of shear stresses, i.e. strike-slip

[3]We define fluidization to occur when the previously static bed attains liquid-like properties. Liquid like properties include for example the relaxation of internal shear stresses (i.e. a zero angle of repose), buoyancy effects becoming increasingly important, the development of surface waves.

faulting, and the critical fluid pressure for the formation of seepage structures. The presented experiments and derivation of the critical pressure for fludization in the presence of shear stresses indicate the generality the pipe-formation along strike-slip faults. In [3] we apply this mechanism to the triggering of the Lusi mud volcano on Java, Indonesia.

Paper 4 presents an example of how ascending fluids induce localized deformation in partially consolidated geological materials. This paper deals with the complex plumbing system in the Dolgovskoy Mound (Black Sea) forming when fluids seep through alternating layers of clay and coccolithic sediments. A mound is a positive topographic feature on the sea bottom indicating focused vertical migration of fluids. The crusts sampled consists of carbonate cemented layered sedimentary units associated with several centimeters thick microbial mats. Different morphologies were observed, such as subsurface cavernous carbonates consisting of void chambers up to 20 cm^3 in size. We performed experiments on a vertically oriented HS-cell showing how seepage forces localize at layers with contrasting physical properties (here: permeability). In the experiments the ascending gas lifts up the low permeability layer, creating voids, enabling the development of a complex network of channels [4].

In addition to these projects, I have been fortunate to join in on other projects during my time here at PGP:
(a) The beautiful tessellation pattern of lichens forming when individuals grow radial from local seed-points [5],
(b) The formation of folds in thin elastic-plastic sheets [6],
(c) Point-pattern analysis of the spatial distribution of hydrothermal vent complexes in the Karoo Basin [7], and
(d) The formation of a Martian spider-like patterns in the laboratory by gas-expulsion through a deformable granular material [8].
(e) Linear Non-Equilibrium Thermodynamics with application to Earth Systems. Pictures from some of the article are shown in Fig. 1.

Chapter 1 introduces the coupling between fluid flow, granular materials and geology and how this coupling can be used to understand some selected examples and processes. In chapter 2 the field of fluid induced deformation of rocks with a special emphasis on pipe-formation in sedimentary basins is introduced. In chapter 3 the theoretical concepts needed to understand the relation between gradients in fluid pressure and stresses in granular materials are introduced. The papers are summarized and appended in chapter 4.

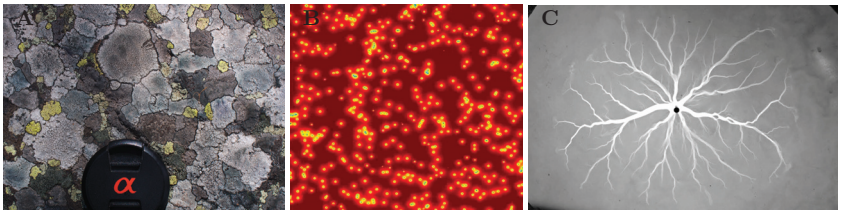

Figure 1: **A** Lichen mosaics growing on rock surfaces [5]. **B** Two-dimensional pressure model employed to understand the spatial distribution of Hydrothermal Vent Complexes in the Karoo Basin (South Africa). **C** The formation of ∼30 cm sized Martian spiders in laboratory [6].

Part I

Introduction

Chapter 1

Granular Matter, Fluid Flow and Geology

This chapter introduces the relation between granular physics, fluid flow and processes on Earth.

There has been increasing interest in the coupling between fluid flow, granular materials and geological applications in recent decades [9]. This interest arises both from its practical importance to the industry and from the pure curiosity of Nature. Understanding of the coupling between the collective behavior of granular particles and fluid flow has been important to a range of scientific disciplines such as geology, geomorphology, and chemical engineering.

The handling of grains and powders are of great importance to e.g. pharmaceutical, chemical processing, oil and gas refining, drying, solid fuel gasification and combustion and agricultural industries. Estimates say that the handling of granular materials, in all, consumes $\sim$10% of the energy produced on Earth [9]. Thus, any advance in understanding the physics of granular materials is bound to have major economic impact.

We live in a *granular world*. Granular matter, such as grains, rice, powders, sand, and glass beads amongst others, has been used as model materials to understand a wide range of physical processes on Earth. The physical laws governing the behavior of granular matter has been applied to cases in which the particle scale ranges from a few microns (in the lower limit) up to ice-bergs and the particles in the rings (made up of $\sim$ 1 cm icy particles in a band roughly 1 km thick) of Saturn (in the upper) [9]. Thus, the science of granular materials span over at least 12 orders of magnitude in size. An improved understanding of granular physics is of great importance to Earth Sciences and Planetary Sciences.

Granular matter is defined as a conglomeration of discrete particles sufficiently large such that thermally induced Brownian motion can be neglected. In granular systems the only particle-particle interaction is through repulsive and/or cohesive short-range contact forces. Since temperature induced fluctuations are irrelevant in these systems, except from a few examples [10], there is no internal drive towards a global equilibrium as in many other systems. Therefore, despite the inherent simplicity, static granular systems are unavoidably always out of equilibrium such that we must come up with new concepts in order to

understand and predict their physical behavior.

Within the papers appended this thesis, we have performed a range of experiments on fluid induced deformation in granular systems. An integrated understanding of fluid flow, granular physics and material strength is needed to both to understand the physics experiments themselves, but also for how to employ the concepts within a geological environment. As a background for our work I will in the following go through some selected geological examples, in which the coupling between fluid flow and granular physics plays an important role. The examples are grouped in two logical categories, the surface processes and the bulk processes. I will start by presenting some surface processes of fluid flow and dynamically evolving granular systems (sec. 1.1), before 'diving' into the bulk of the 'granular bed' (sec. 1.2) showing examples of fluid induced deformation.

After the examples are presented, we introduce the concept of *driven systems*, how dissipative systems are unavoidably out of equilibrium and how the dynamics has to be driven by an influx of externally induced energy. Then I will define the stress tensor of a granular system in sec. 1.3. Towards the end of the chapter I introduce the concept of rheology and discuss how granular matter is used as model materials for a wide range of geological materials (sec. 1.5). Depending of e.g. the rheology and the rate of the imposed power, I will show how pressurized fluids may deform a solid body and discuss the transition from fracturing to fluidization (sec. 1.5.3).

1.1 Some Surface Processes

This section presents three examples where a combined understanding of granular physics, fluid flow and geology is used to explain the observed surface phenomena. I will look at dune and ripple formation in sand and snow, geomorphology and erosive processes in rocks, and the formation of a V-shaped pattern on beaches.

1.1.1 Dunes and Ripple Formation

The most obvious case of granular material on Earth is found as sand in deserts, covering $\sim 10\%$ of the surface of the globe. Within deserts, a striking dynamic feature is the formation and movement of large (ten to hundreds of meter in size) sand dunes [11-13] and upon these small (centimeter sized) ripple marks (see Fig. 1.1A). Even though the scales between dunes and ripples are quite different, they both form due to the interplay between the wind (Eolian processes) and the erosive surface processes [14]. Given enough time and steady winds, the small scale ripples grow, eventually turning into dunes [15]. Depending upon the size, shapes and density of the grains, the temperature, humidity and speed of the air blowing over the sand, different patterns form as the wind 'pluck' grains off of the front-side[1] and deposits the particles on the down-wind or lee side. As the surface morphology changes, this feeds back onto the wind pattern creating eddies and turbulence effects which then, in turn, affects the erosion pattern. This phenomenon is an example of a highly non-linear system in which the flowing gas affects the granular bed.

[1] A process known as saltation.

An analogue to this pattern also occurs in snow, as is shown in Fig. 1.1B. In this picture the surface of the snow has developed into fascinating morphologies, formed due to interplay between the eroding wind and the deforming snow.

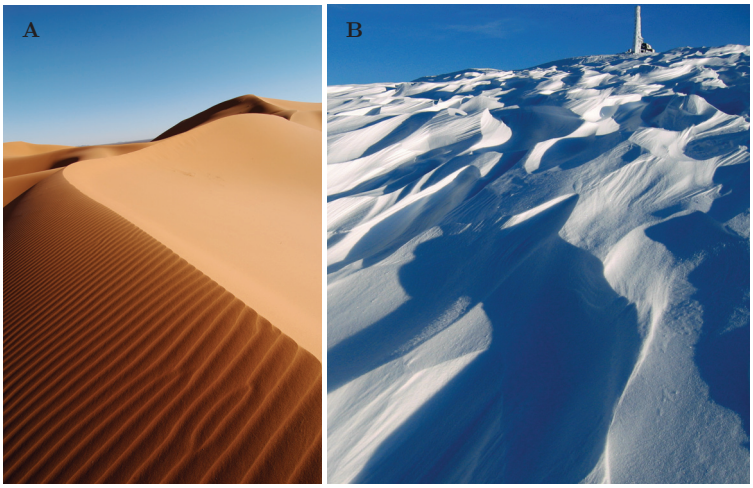

Figure 1.1: **A** Image of cm-scale ripples forming upon 10's to 100's of meter sized sand dunes (courtesy of the English Wikipedia, article on dunes). The dunes and ripples form as wind is blown over the sand, whilst the evolution in the surface morphology feeds back on the wind pattern generating eddies and turbulence effects. **B** Dune formation in snow. A fascinating surface pattern occurs when wind is blown above the eroding substrate (here snow). The image was taken in Etnedal close to Spåtind, 2007 (courtesy of Ola K. Eriksen).

As the ridge grows taller, wind-blown sand is more likely to be deposited on the upwind side. This effect gradually increases the slope angle on the downwind side. When the angle increases above a critical angle, surface avalanches are triggered. Within avalanches a range of interesting non-intuitive processes are at play. For example, variations in the surface humidity conditions may destabilize and trigger avalanches [e.g. 16-18].In addition, it is shown that the size-frequency distribution in the avalanche sizes follows a power law behavior indicating self-organized criticality (SOC). This effect was accurately shown in a slowly driven, two dimensional experiment with ball bearings [19]. Some numerical models of sand-pile dynamics show SOC in avalanching systems, but whether or not the behavior of real sand is controlled by SOC is ambiguous [16].

Avalanches of grain mixtures with contrasting properties (e.g. angularity and size) display other interesting, non-intuitive physical phenomena. In some cases the grains de-mix and a stratified pattern emerges [20]. Another observable phenomenon includes the size effect of the grain mobility. Experiments show that the mobility increases with increasing grain size such that the largest particles flow furthest and vice versa [21]. These natural segregation mechanisms (amongst several others) have large impact of patterns observed in Nature. In

addition these processes affects our understanding of sedimentary stratigraphy, which is important to the oil and gas industry (e.g. [22]).

In geo-technical engineering concepts of stability (of granular systems) are important. This concept is used to evaluate e.g. the snow avalanche risk in mountains and skiing resorts. A detailed knowledge of stability in relation to snow may be far more complicated than for sediments and sand dunes. This is due to the large number of physical effects playing a role in the calculations, and the dominating history dependence in snow. Effects such as the angle of repose, the temperature driven Marangoni effects, vapor transport, crystallization processes, snow metamorphism [23], wind conditions and temperature variations have been shown to be important to the mechanical stability [24].

1.1.2 Erosion and Geomorphology

Without the erosion by fluids, that being of water, avalanches, and wind, the face of our planet would be quite different than its present look. Erosion is responsible for shaping mountains, canyons, seacoasts, and rivers in a range of length-scales. Despite how common these patterns are to the human eye, our understanding of the physical mechanisms of fluvial erosion and granular physics is far from satisfactory. Geomorphology, the science of how the landscape is shaped has been influenced by insights gained from experiments on granular physics. Lague et al. [25] presented a beautiful landscape forming experiment where water was precipitated evenly over a bed of sand. In their experiments a complete drainage network developed due to growth erosion instabilities in response to the precipitated water and the tectonic uplift. A well-defined slope-versus-area power law consistent with erosion models that includes non-negligible thresholds for particle detachment characterized the steady state surfaces. Their drainage pattern, where small gullies meet to form larger gullies, showed structural and statistical similarities to the drainage patterns observed on Earth [26, 25].

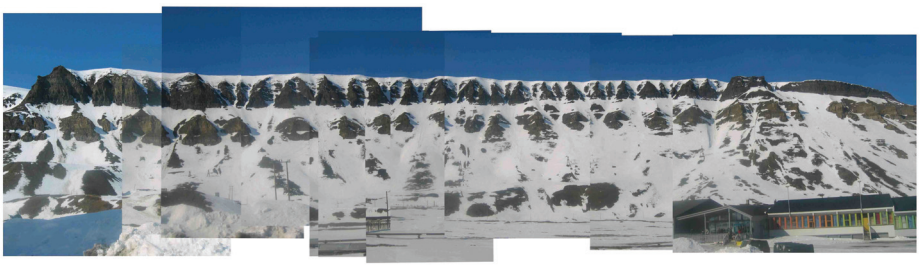

Figure 1.2: Erosion pattern in Longyearbyen (Svalbard) where the gullies are formed due to the erosion caused by avalanches of snow, slush and rock-falls.

Fig. 1.2 shows a picture from Longyearbyen (Nybyen) at Svalbard. Here, avalanches drive the erosion of the rock, mainly in the spring, containing a mixture of snow, slush and rocks. As the fluidized mixture erode the rock, a network of gullies form. The average distance between gullies increases further down the slope. This is a common trait of drainage driven erosion processes on Earth.

1.1.3 V-shape (Chevron) Pattern on a Beach

Sand is present in large quantities within shorelines and beaches along oceans and lakes. In these systems a wide range of interesting physical effects are observed. For example, as the water drains back into the ocean after being brought on-land by waves, a distinct pattern develops. Depending on the slope of the beach and the drainage velocity, a family of patterns form [27], one of which is the V-shaped Chevron like pattern seen in Fig. 1.3A and B.

As the mixture of water and grains flow back into the ocean the properties of the suspension changes with time in a rather non-intuitive way. The internal dynamics and pattern formation in this system occurs within seconds between each incoming wave. The V-shape forms when water is expelled from the suspension and localizes through erosive channels. The characteristic distance between the channels is in the order of $\sim$ 10 cm (see close-up in Fig. 1.3B). Between each the darker areas in the figure forming the V-shape the suspensions is stagnant. Which means that the amount of sand (within the suspension) is sufficient to locally jam the system. In the late stage of the process, just before a new wave flushes on-land, the only dynamics is localized in the darker V-shape structure as the water flows back into the sea.

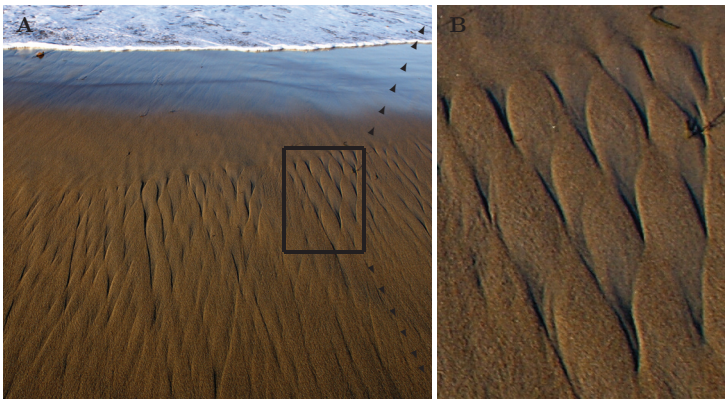

Figure 1.3: **A** Picture of the V-shape pattern forming on beaches as the water drains back into the ocean (San Diego, 2009) after water is flushed on-land by the incoming waves. The field of view is roughly three meter across. **B** Close-up of the pattern marked off in the box in **A**.

1.2 Some Bulk Processes

In the previous section, the coupling between granular physics and the hydrodynamic properties of fluids were used to understand processes on the Earths surface, was presented. Within this section, I will 'dive into' the bed and study bulk processes where the same coupling is important.

Sedimentary basins consist of vast quantities of silica particles and organic

materials that have been brought in by eroding rivers and oceanic currents. From a granular physics point of view such basins consist of individual particles with a varying degree of porosity and inter-particle degree cohesivity (the strength of the contact bonds between neighboring particles).

In this section some concrete examples are shown where concepts of fluid flow, granular physics and geology are integrated to understand the phenomenon under study.

1.2.1 The Brazil Nut Effect

Within agriculture the farmer annually experiences that 'new' stones appear on the surface of his field. This phenomenon is termed the 'Brazil nut effect' [28], from the observation that the largest nuts (the Brazil nuts) were often observed on the top within boxes of nut mixtures. Experiments were performed within vibrating granular beds showing that the largest particles migrate upwards through time [29, 30]. There are several theories (up to ten), not necessarily mutually exclusive, that may apply to the different cases in which this phenomenon occurs [31]. One of them applies to the case of the farmer. In this case temperature induced freeze-thaw cycles induce dilation in the soil as water freezes and ice-crystals forms. Since the dilation do not occur within the rocks, but in the surrounding soil (matrix), and the effect of the upper free surface, this collective behavior effectively pushes the large rocks upwards during the winter. When the summer comes, the ice-crystals melt and the water drains away forming cavities beneath the rocks. These cavities are then filled in with sand such that with time (a retching mechanism caused by void filling) this induces an upward drift of the large rocks accumulating them onto the surface.

Freeze-thaw cycles in rock-soil mixtures has been found to cause a range of intriguing patterns observed north of the polar circle in arctic regions on Earth. In these environments the accumulation of rocks into stripes (within slopes) and polygons (when the ground is flat) is a relatively commonly observed phenomena [32]. The large rocks accumulate basically because rocks are pushed around within the soil, but not, when rocks are grouped together with other rocks. Such a pattern is observed in Fig. 1.4 where a the rocks accumulate in stripes down the slope.

Nearly a decade ago an addition twist was added to the Brazil nut effect. M. Mobius *et* al. 2001 performed an interesting experiment where they studied how the weight effects of the rise-velocity of the large particles [33]. A rather unexpected result was obtained as they showed that both the lighter and heavier large particles rose faster to the surface than those large particles with a density equal to the surrounding matrix. The experiments told them that there is a causal link between the rise time of the large particle (by a retching effect), the density of the larger particles and the interaction with the interstitial air. They could know this since by re-doing the experiment when the air was vacuumed out of the system, the density effect in the rise-velocity of the large particles vanished. The definite answer to how the interstitial air couples to the rise time of light or heavy large particles in vertically shaken systems is highly non-linear and has triggered a vast number of articles in the physics literature during the last decade [e.g. 31, 34-38].

Figure 1.4: Freeze-thaw induced dilation in the ground pushes large rocks upward collecting them into a stripe-like fashion. In this picture you see Jostein R. Kristiansen and Nicolaas E. Groeneboum on a trip to the north of Finland during the summer of 2008. A glacier is seen in the bottom of the picture.

1.2.2 Intermittence effects, stick-slip behavior and the ticking hour glasses

Granular materials react differently to imposed shear than ordinary fluids. Cohesion-less powders, such as glass beads and sand, develop shear bands, that is narrow zones with large relative particle motion, rather than the uniform deformation obtained for Newtonian fluids. The adjacent regions are essentially left rigid [39]. This observation is similar to the formation of shear bands observed in fault gouges in shear zones. The fault gouges are the zones of fragmented grains that develops between two parts of the Earths crust that slides onto each other (e.g. as was showed to form in sandstone [40]). The internal processes occurring within a shear plane in three dimensions are not easy to observe directly. Making these observations calls upon either a complicated experimental setup [41, 39] or numerical modeling [42].

For sheared systems, a significant disturbance within the stress states is observed. Elevated contact forces seem to follow paths or chains that sometimes span the whole system size. This concept is termed force chains and arise from the inherent randomness in granular materials and the short-range-ness of the repulsive contact forces [43]. On a phenomenological level, these perturbations can simply be explained by; either two beads are in contact or they are not, but it is a concept difficult to include in mean field theories. Thus, constructing an effective medium theory based on the continuum approaches may be flawed even from the beginning.

P. Dantu [44] was the first to do experiments to directly observe the stress

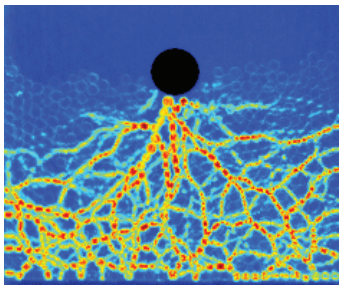

Figure 1.5: Image of a photo-elastic granular material subjected 'meteor' impacting on a granular bed. Image obtained from the 'Behringer Group' at Duke University (USA).

pattern in a two-dimensional granular material subjected to a directed localized compression force. By exploiting the photo-elastic effect he showed that stresses localized along an intricate network of stress paths, and that the stresses tend to be redirected laterally, as shown in Fig. 1.5.

Similarly, observations obtained by molecular dynamics models (e.g. [42]) and direct measurements of the distribution normal stresses at the base of a pile of sand show that static beds are held up by a 'skeleton' of force chains [45]. The force network represent the key grain-scale factor determining the macroscopic mechanical properties of stability, elasticity and sound transmission [43, 20, 46]. The chains of elevated stresses have been observed to span lengths up to 100's and 1000's of particles. Hence, it is problematic to define the mesoscopic length scale ϵ, the scale at which average material properties such as density, temperature, porosity and stress states are well defined. Typically, for a mean field model to apply the mesoscopic scale is required to be (1) much smaller than the typical distance with significant variations in the listed properties, and (2) much larger than the size of the individual phase elements (particles). For solids and liquids this is typically a few to ten nanometers, and involves averaging over a few thousands atoms or molecules. In granular matter, this length-scale is not easily defined, if possible at all, since force chains sometimes span the whole system under study.

In addition to the localization of stresses in sheared granular systems, these systems inhibit intermittency effects [47]. An example of such an intermittency effect is the stick-slip behavior, i.e. the sudden release of the imposed forces observed in dry granular materials [48]. In Earthquakes, the size-frequency distribution of slips follows a scale free behavior, i.e. that small quakes are more frequent than bigger ones (the Gutenberg-Richter law). In the Earthquake community, a wide range of processes is attributed to this behavior aiming at predicting earthquakes. Models are based upon the stik-slip instability coupled to a Mohr-Coulomb failure criterion (see sec. 1.5) along a pre-existing fault plane. Despite all the effort the last decades a unified earthquake model has not emerged yet. Another example of intermittency effect is observed in ticking hour glasses in which the fluctuations in the grain flux were caused by the incipient

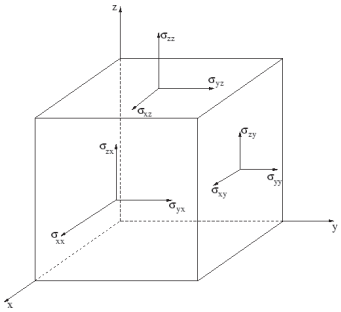

Figure 1.6: Definition of the components of the stress tensor.

motion of gas [49].

1.3 Driven Systems

All the cases discussed so far are examples of driven systems. Since the particle-particle interaction is dissipative in nature, this lead to a rapid decay in the internal dynamics when the imposed power is stopped. This has consequences to the dynamics, that is, granular systems need to be driven at imposed powers exceeding a critical rate in order to evolve through time. This critical limit may vary between the nature of the granules and how the energy is imparted to the system. In shaken systems the critical limit is given by the strain amplitude, that being, the product of the amplitude and frequency of shaking; In avalanching, or poured, systems, the external drive is associated with the angle of repose; In sheared systems, the dynamics is driven by shear stresses exceeding certain shear stresses; Whilst a fluidized systems needs to be driven with fluid pressure gradients (that being fluxes) exceeding certain limit limits. Driven systems are often referred to as being far out of thermodynamic equilibrium, so equilibrium considerations generally fail.

Systems that are driven far out of equilibrium attain several non-intuitive physical phenomena. Depending on the nature of the particles, how they interact and the properties of the interstitial fluids, granular beds can behave both like solids, with well defined cohesive and frictional strength, or like fluids, in which the imparted drive induces a flow of the grains [50, 51].

1.4 The Stress Tensor

In order to evaluate the critical limits for driven granular systems the stress tensor needs to be defined. The stress tensor is defined by the sketch shown in Fig. 1.6 where the subscripts $i, j = 1, 2, 3$ denote the three spatial directions x, y and z. The surface force T_j acting around the surface $\partial\Omega$ can be written as,

$$T_j = \sigma_{ij} n_i, \tag{1.1}$$

where σ_{ij} is the 3-dimensional stress tensor,

$$\sigma_{ij} = \begin{bmatrix} \sigma_{11} & \sigma_{12} & \sigma_{13} \\ \sigma_{21} & \sigma_{22} & \sigma_{23} \\ \sigma_{31} & \sigma_{32} & \sigma_{33} \end{bmatrix} \tag{1.2}$$

and n_i is the unit normal vector onto the surface $\partial\Omega$. The diagonal elements are the normal-pressure acting onto surfaces within the material, whilst the off diagonal elements are the shear stresses which (for normal fluids) induce strain ϵ_{ij} within the matrix.

1.5 Granular Matter and Geologic Materials

Some of the reasons why granular materials can be used as a model material for geological systems are discussed here. I will do this by defining the term rheology, that is, how a material responds to external load. The rheology is a material specific quantity that relates the imposed stresses to the measured strains (i.e. displacement gradients) in solids and/or strain rates (i.e. velocity gradients) in fluids. The family of rheologies in Geologic materials is vast, and complex rheologies are often called upon to explain any observed phenomenon. In the following, models for material strength are discussed, but first the concept of Mohr-circle is introduced.

1.5.1 The Mohr Circle

In order to quantify the stress state in a body at a specified point, the Mohr circle is a handy concept. This concept is a standard graphical representation, widely used in the geomechanical engineering, both to evaluate the components of the stress tensor and calculate if the stress state reaches plasticity and yielding-conditions or not. In a Mohr-Coulomb diagram the second invariant of the stress tensor, the stress deviator, τ is plotted along the y-axis and the normal stresses σ_{ii} along the x-axis. The stress deviator is caused by differences in the components of the stress tensor σ_{ij}. In 2 dimensional systems the stress deviator can be calculated according to [52, 53],

$$\tau = \sqrt{(\sigma_{xx} - \sigma_{yy})^2/4 + \sigma_{xy}^2}, \tag{1.3}$$

Each point on the circle identifies the normal and tangential components of the stress deviator (see Eqn. 1.3). The centre of the circle lies on the x-axis, between the minimal and maximal normal stresses, σ_{11} and $\sigma_3 3$ respectively. The diameter of the circle is defined as the difference between the maximal and minimal normal stresses.

1.5.2 Yielding

When the Mohr circle reaches any of the failure envelopes, that being the Mohr-Coulomb envelope, the von Mises envelope or the Griffiths failure envelope the material fails accordingly. I will go through the different failure criterions, or envelopes now.

Mohr-Coulomb Materials

A sedimentary rock is initially made up of grains, which have been brought into a basin by ocean currents and rivers. As time goes by the sediments undergo compaction and lithification welding the individual grains together. Thus, the rheology of a sedimentary rock spans the behavior of loose sand with no bond strength to cohesive rocks with high inter-particle bond strengths. From a granular physics viewpoint, sedimentary rocks are comprised of granular materials with varying degree of consolidation / cohesion (C)[2].

Granular materials, cheap and easily obtainable in the lab, can have rheological similarities to the rocks making up the Earths crust. For example, a range of rock-types and granular materials such as dry sand or glass beads are all examples of frictional materials. These materials are referred to as Mohr-Coulomb materials with a given shear strength τ_s, along a plane $\vec{n}$, proportional to the normal load $\sigma_{\vec{n}}$ onto the same plane. In addition, the shear strength increases for increasing C, such that the shear stress at failure (Mohr-Coulomb envelope) is summarized in,

$$\tau_s = C + \mu\sigma_{\vec{n}}, \tag{1.4}$$

where μ is the frictional coefficient (typically in the order of 0.5-0.7 for rocks and 0.4 for the glass beads in this study). Even though the coefficients C and μ may vary for different frictional materials they are, from a rheological viewpoint, equivalent. This exceedingly simple macroscopic law is rather surprising, given the complexity, heterogeneity and non-linearity observed on the microscopic level.

von Mises Materials

Another commonly observed geological material are von Mises materials. These are materials with constant shear strength, independent on the normal load. Clay is a common example of such a material found both in the lab and in geology. In this case the shear strength is simply associated with constant yield strength,

$$\tau_Y = Y. \tag{1.5}$$

Griffiths Materials

The last group of materials in the field geotechnical engineering is associated with the formation of tensile failure of a fluid-filled crack. The failure condition, or fracture toughness, can be calculated by the Griffiths criterion, describing how well materials resist fracturing. In this case the critical value of τ_G is given by,

$$\tau_G = \sigma_T + \sigma_m, \tag{1.6}$$

where σ_T the material dependent tensile strength and $\sigma_m = (\sigma_{xx} + \sigma_{yy})/2$ is the mean effective stress in 2 dimensions.

[2]The term consolidation is meant as the compaction of a sediment in which the granules compact. Cohesive bonds form between the granules. The concepts of consolidation and formation of cohesive bonds are associated with the word lithifaction, i.e. the process in which sediments compact under pressure, expel connate fluids, and gradually become solid rock.

1.5.3 Hydraulic Fracturing, Fluidization and Viscous Fingering

Other granular systems can attain completely different rheologies and thus their behavior can completely change from one system to another. An example is the case when air is injected into either a dry or wet bed of glass beads. In the case of the wet bed, water bridges form between the grains [54, 18], increasing the inter-particle cohesive forces. The increasing cohesion leads to significant changes of the bulk rheological response when subjected to pressurized air. As such the morphology of the response changes from a 'diffuse' deformation (i.e. fluidization where all 'bonds' between particles break) into a 'localized' deformation where tensile cracks form. This cross-over can be seen in Fig. 1.7. The glass beads are the same in both experiments.

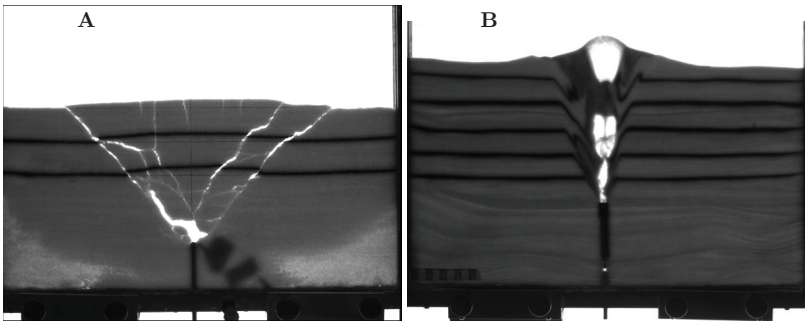

Figure 1.7: Morphology of the deformation patterns forming in response to air injection into wet and dry granular materials. **A** Localized deformation occurring in cohesive, water-wetted glass beads materials. Tensile fractures form. **B** A more diffuse deformation occur in dry glass beads. Every inter-particle 'bond' breaks (there are no bonds) and the matrix fluidize.

A similar crossover was studied as the transition from viscous fingering to hydraulic fracturing when a viscous fluid is injected into a colloidal gel. This was studied experimentally by e.g. Lemaire et al. 1991 and Hirata 1998 [55, 56] who showed that the cross-over was controlled by (1) the rate at which the low viscosity fluid is injected and (2) the elastic-plastic properties of the gel. By controlling the mixing concentration of powder and water, and tuning the injection rate, they developed a morphological phase diagram where this crossover was shown.

In Earth systems the particle-particle cohesion increases with increasing amount of consolidation (as sediments are buried and compacted through time). By analogy to the images shown in Fig. 1.7, the expected morphological response to the localization of high fluid pressures changes as the inter-particle cohesion increases. How, and when the transition from fracturing to fluidization occurs; if the transition is sharp, or if it is continuous, are extremely interesting questions, but are not studied quantitatively within this thesis. However, these issues could be of great relevance to the interpretation and understanding of a

range of geological systems.

1.6 Fluid Induced Deformation

It is well known in the geotechnical engineering that the effective strength of rocks are reduced by elevated fluid pressures [57]. This principle is modelled by subtracting the fluid pressure from the mean effective stress [e.g. 52] such that,

$$\sigma'_m = \sigma_m - P_f. \tag{1.7}$$

In addition to that, fluid pressure gradients within a porous material induces a fluid flow that affects the stress state in the solid matrix [58, 59], which is addressed in Sec. 3.1. Consequently, this effect changes both the position and the diameter of the Mohr-circle causing yielding in situations that would otherwise be stable (e.g. [60]).

1.6.1 Fluidization

The concept of fluidization, the phenomenological phase transition, where the previously static ('solid') bed starts flowing (with 'liquid-like' properties), is frequently used within this thesis [61, 62, 63, 64, 65]. Fluidization is often termed liquefaction, since the material starts flowing as a liquid when exposed to any non-zero deviatoric stresses, i.e. the shear strength $\tau_s \rightarrow 0$. The fluid like properties in fluidized granular systems include for example surface waves, buoyancy effects, a zero angle of repose and the material can move as a bulk in response to the interstitial fluid flow. We limit ourselves to discuss gas-induced fluidization of frictional, brittle materials. But we will in this thesis argue that the brecciated elements formed from consolidated rocks may fluidize if the pressure gradient is maintained after the initiation. Experiments and analytic calculations of the critical conditions for fluidization is addressed in Sec. 3.2 and in the appended papers.

1.6.2 Segregation in the Gas-Fluidized Phase

Fluidization caused by pumping gas into the bottom of a granular packing is for instance used in the pharmaceutical industries to mix powders [9, 66]. A good mixing of particles is also desired in other industrial applications such as the coal combustion and the food processing industry. In these cases, segregation may reduce the quality and integrity of the end product [67, 9]. On the other hand, segregation by fluidization is needed to separate one solid phase from another used in a variety of industrial agricultural, mining, and waste management applications.

Variations in either particle density, angularity, restitution coefficients or particle size give rise to segregation [68-75].We will here limit ourselves to segregation by size.

It is well known that size segregation in the fluidized phase is caused by the difference in the scaling with the particle diameter for the weight ($\propto d^3$) and gas-particle drag in both the laminar ($\propto d^1$) and turbulent regime ($\propto d^2$) [e.g. 76-93].As such a critical diameter exists where the larger particles falls down and the rising fluids draw up the smaller particles.

By adding an additional twist to this concept, that is, a flow focusing mechanism in which the flow is focused through areas with elevated permeability system evolves differently. In these cases fluidization and also the sedimentation of large particles are localized and a pattern with vertically oriented pipes may occur (paper 1 [1]). The Carman-Kozeny relation can estimate the permeability of a porous bed with a geometry made up by solid particles,

$$k = \frac{d^2}{45} \frac{\phi^3}{(1-\phi)^2} \tag{1.8}$$

where the permeability scales with the mean particle diameter squared. We argue in paper 1 that this feed-back mechanism causes the pattern seen in Fig. 1.8.

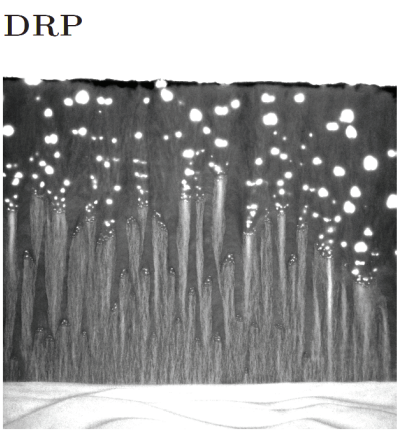

Figure 1.8: The segregation pattern occurring in dry bi-modal sized mixture of glass beads as the bed de-fluidize by sedimenting the large particles (paper 1). Within a limited range of imposed gas velocities pipes grow due to flow localization induced by perturbations in the permeability. The areas with larger particles focus the flow, the fluidization, and the subsequent sedimentation of the large particles. The image shows the deeply rooted pipe (DRP) [1].

Segregation by size can also occur in sediment systems in which the free fall velocity depends on the grains size. The free fall velocity can be calculated from the balance of the gas-particle viscous drag and the weight of the particle. Imagine the scenario in which an off-shore seep structure (a vertically oriented pipe with elevated permeability, e.g. a pockmark) is formed through the sea-bed. Whatever the formation mechanism, within this framework the seep structure could withstand erosion and in-fill of sediments since the ascending fluids inhibit the sedimentation of the smallest particles. Thus, only the larger particles will sediment into the pockmark and the large permeability pipe could prevail.

1.7 Fluidization in the Physics Literature

The coupling between gradients in fluid pressures to the stresses in a solid matrix is well known in the physics literature. The concept of minimum velocity of fluidization, that is the fluid velocity at which the viscous drag imparted onto a column of grains equals the buoyant weight of a bed, was introduced by Ergun in 1952 [94] and later followed up by Kunii and Levenspiel in 1969 [61]. Since then, a range of publications has addressed the issue of fluidization [62] (and references therein). The concept of fluidization has been used in the pharmaceutical industry e.g. to ensure mixing of powders. The industrial designs have been patented to optimize the operation of fluidized beds, e.g. the hierarchical fluid injection system [66].

Particle models, as model systems for granular matter, coupled to forces induced by the incipient fluid motion gives valuable insight into the understanding of fluid flow and granular physics [95, 96]. These models have been used with great success e.g. to study the Granular Rayleigh-Taylor Instability forming in systems where a bed of particles falls through a fluid. As one particle advances ahead of his neighbors it pulls along other particles forming jets with certain distances. Between these jets, gas-bubbles rise through the bed.

In principle, the particle dynamic models coupled to the fluid flow would solve all the physical aspects of granular-hydrodynamic systems. But these models are still in-efficient, so drawing any final conclusions from these models, which are highly limited by the system size, may be problematic. In addition, there are unresolved question on how to resolve the crossover from Darcian flow within a porous media to Stokes flow within a channel or a bubble. More explicitly, how does one calculate the permeability in the open void within these models? Moreover, how does one resolve the potential turbulence effects at high Reynolds numbers? and; what is the effect of the third dimension in these models? These are, in my view, some key issues to address within these models to fully resolve the problem, and coupling between fluid flow and particle dynamics.

Chapter 2

Pipe-Formation in Geology

Piercement structures, the structures forming when fluids are expelled through sediments and rocks, are common in Nature. They manifest themselves in a variety of settings, but are most commonly in sedimentary basins. Some examples include pockmarks, mud volcanoes, hydrothermal vent complexes and kimberlite pipes. These examples are discussed one by one in the following. I will address their origin, the materials involved, the geometries of the emplacement, what they have in common and what separates them. Despite the diversity in origin and spatial dimensions, piercement structures in Nature share a range of structural similarities consisting of circular pipes containing intensely deformed rocks [97-102].

2.1 Observations of Gas-Escape Structures

This section describes observations on fluid escape structures in different geological settings. The observations may give insight into how geologic materials, such as sedimentary rocks, rapidly expel fluids onto the surface.

2.1.1 Mud Volcanoes

Mud volcanoes are structures forming when gases (typically CO_2 and CH_4) and liquids (such as acidic or salty water and hydrocarbons) are rapidly expelled through sedimentary, clay rich, basins. Mud volcanoes are regularly observed in settings with organic rich, water bearing sediments with a high sedimentation rate and a low geothermal gradient [103-106].Volume changes associated with the maturation of organic rich sediments may increase the fluid over-pressure, at depth, given sufficiently high sedimentation rates. In addition it is proposed that mud volcanoes are often found in sedimentary basins with active tectonic processes. They are often formed in cases where both the tectonic plates converge, where the fluid pressure builds up due lateral compression of sediments, or diverge, where the basin opens, accelerating the sedimentation rate [98]. Geochemical analysis shows that fluids are often of a deep origin and are thought to migrate through the sediments through a complicated network of chambers and pipes [98] (see e.g. the schematic drawing Fig. 2.1). The surrounding stratum is sometimes bending upwards (as a diapir), indicating that the surrounding

materials are pulled along with the ascending fluids and rocks (termed mud breccias). In other cases the surrounding stratum bends downward due to gravity collapses when vast amounts of material is brought with the erupting fluids onto the surface.

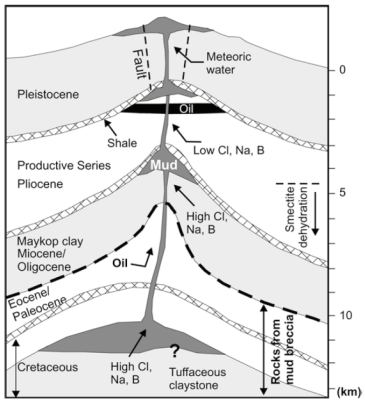

Figure 2.1: Schematic drawing of the complex plumbing system for the mud volcanoes in Azerbaijan. The sketch is from Fig. 10 in Planke et al. 2003 [98]. It is inferred that fluids have a deep origin (up to 10 km), they focus along vertical channels, and the surrounding sediments are pushed upwards together with the ascending fluids (diapir).

Mud volcanoes are found both off-shore and on-shore sediments and on a variety of scales [107]. The largest mud volcanoes are found in Azerbaijan with sizes up to 10 km in diameter, reaching up to 700 m in height. Another example is the Lusi mud volcano (Java, Indonesia) described and discussed in Sec. 3.2.2 and in paper 3 (and in references therein). The Lusi mud volcano is the first mud volcano whose birth and dynamic evolution has been documented. Initially, the main eruption site was one out of several seeps along a fault plane. The fault plane was reactivated prior to the triggering of the eruption, the 29th of May 2006 where the boiling mud started to erupt. This is a commonly observed phenomenon, at least for mud volcanoes [3]. During the days and weeks after the initiation, the eruption structure grew in size and evolved into the catastrophe it is today; with peak eruption fluxes up to $\sim$180 000 m^3 per day and a main eruption crater of 70-80 meter in diameter [106]. Currently the mud volcano has flooded three villages, and up to 30 000 people have lost their homes.

Since the birth of the Lusi mud volcano, the triggering mechanism has been debated in the Earth science literature during the last years. The controversy is related to the drilling of a nearby exploration well some 150 meter away from the main eruption site where errors in the drilling procedure, and the lack of steel-casing, may have caused the collapse of the bore-hole and the eruption of pressurized fluids at depth [108, 109].

Other mud volcanoes are significantly smaller in scale. Within the Salton

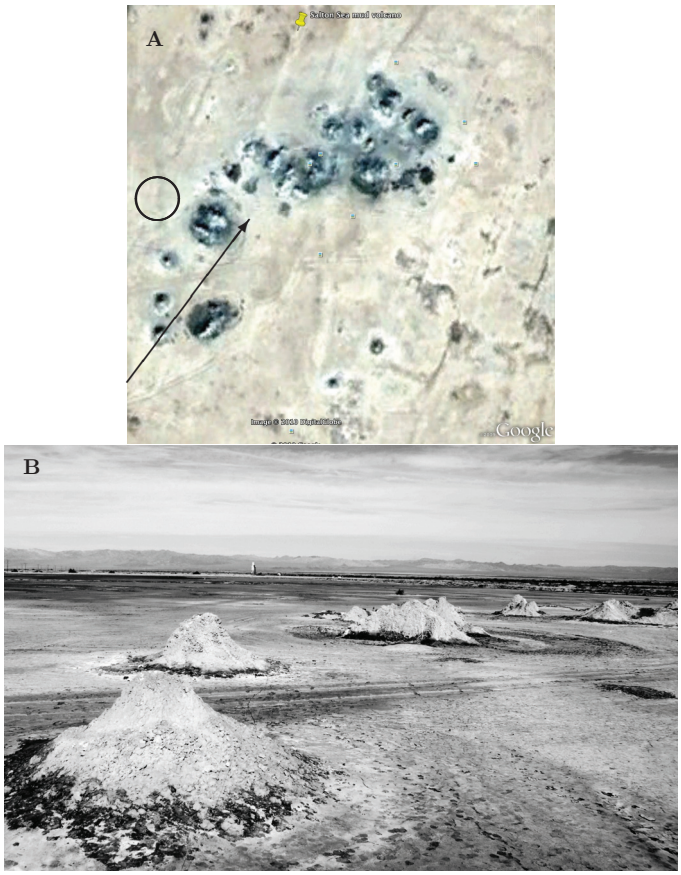

Figure 2.2: **A** Google Earth image of the Salton Sea seep structure (W115°35:40 - N33°12:10, approximately 300 m across). Localized fluid escape structures are observed as darker spots distributed within the bulk of the seepage structure. The circle indicates the position of the picture shown in Fig. (2.6**B**). **B** Picture of the gryphon field (positive topographic structures) where gases, water and hydrocarbon mixed with mud are expelled. As the water vaporize, the mud stops flowing and the volcano grows until a new pathway is formed at the shoulder of the pre-existing gryphon. Image is taken in the direction indicated by the arrow in **A**.

Sea geothermal system, water, mud, gas and hydrocarbons are seeping through meter-scaled gryphons and pools [105]. In Fig. 2.2A a Google Earth picture of the spatial distribution of gryphons (positive features) and pools are seen as darker spots. A close-up of these structures are shown in Fig. 2.2B where gryphons are the positive features (heaps of mud) growing as the erupted mud

dries and solidifies. In this seep field there are approximately 50 seeps within an area of 300 by 300 meter.

The geometry and origin of these structures is not fully understood but it is proposed that these volcanoes are fed by pipe-like structures draining the pressurized sediments.

2.1.2 Hydrothermal Vent Complexes

Hydrothermal vent complexes (HTVC) are vertical pipe-like structures formed by the transport of hydrothermal fluids in sedimentary basins during the emplacement of magmatic[1] sills [e.g., 99, 110, 111]. The heat from the sill induces rapid maturation of organic compounds and boiling of pore water. This leads to a rapid build-up of the fluid over-pressure at depth [112]. Observations indicate a direct association between HTVC and the emplacement of the magmatic sills. See Fig. 2.3 for a schematic drawing of the causal link and the seismic interpretation of the structure.

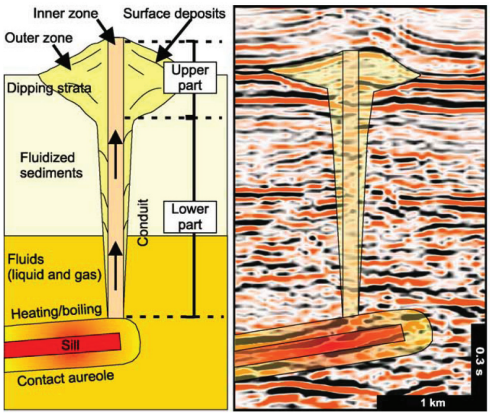

Figure 2.3: Sketch and seismic example of a hydrothermal vent complex from Planke et. al 2005 [111]. The complex consists of an upper and a lower part. The upper part is crater-, dome, or eye-shaped and is connected to the termination of a sill by a cylindrical conduit zone (pipe) with disturbed seismic data (the magmatic sill) in the lower part.

The dating of the large igneous provinces[2], e.g. the Vøring and Møre Basin (North Sea, 55 Mya), the Karoo basin (South Africa, 183 Mya) and the Siberian Traps (Russia, Siberia, 251 Mya), correlate well in time with major mass extinction episodes through the geological record [110]. This suggests that the HTVCs have transported large amounts of fluids into the atmosphere, causing

[1] Magmatic sills are the tabular igneous intrusions into layer parallel sediments. They are commonly approximately horizontal, but may have transgressive segments that cross-cut the stratigraphy.

[2] In this case an igneous province is a sedimentary basin containing significant volumes of magmatic intrusions (sills).

global climatic changes in the past. Two dimensional numerical modeling of the heat transport around the sill and the chemical reaction rates suggests that a 100 meter thick sill is cooled off within 500 years and that as much as 100 kg/m^3 of CH_4 and CO_2 is released from the affected surrounding rocks[113][3]. This suggests that the pressure build-up, and the eruption of hydrocarbons occur roughly within this 500-year time frame.

The close association between the emplacement of magmatic sills and the HTVC are seen several places on Earth [110]. In the Karoo Basin (South Africa), both sills and pipes are observable on outcrops today. This represents then an ideal natural laboratory to study the causal link between the magmatic sills, the aureole processes and the gas escape structures [99]. An aerial photograph of one of these HTVCs is presented in Fig. 2.4A. The typical diameters of the vertically oriented cylindrical pipes are on the order of 100-400 meter and they have a spatial nearest neighbor distribution on the order of 500 meter. Within the HTVC there is evidence of gas escape structures, these are vertically oriented sand-stone pipes on sub-meter scale, and they form within the main large scale hydrothermal vent complex [99].

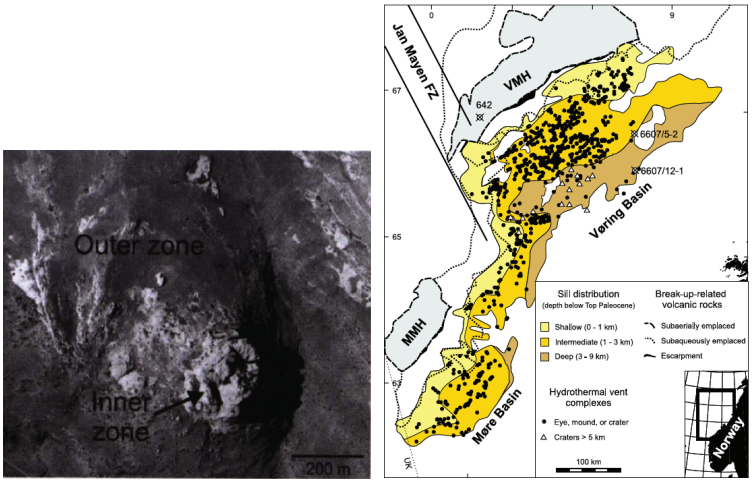

Figure 2.4: **(Left)** An example of a Hydrothermal Vent Complex outcropping in the Karoo Basin (South Africa). Significant erosion of the basin has occurred so the lithified cylindrical pipe we see today was deep during the formation of the HTVC [99]. **(Right)** The spatial distribution of sill intrusions and the localization of HTVC (black dots) in the Vøring and Møre Basin, North Sea. From Fig. 7 in [98].

HTVC, that formed 55 mya, are also observed in the Vøring and Møre basin (North Sea) [111]. These structures have been mapped by seismic surveys indicating that the pipes are rooted in sill complexes at depths up to 7-8 km. In the seismic images the HTVCs are recognized as vertical zones, with a large height

[3]The surrounding rocks that are affected by the heat from the sills are termed aureoles. These rocks are mainly recognized by the *lack* of organic carbon-rich compounds.

to width ratio, and disrupted internal structure (seismic reflectors) compared to the surrounding seismic reflectors. In addition, the surrounding sediments are often observed to be dipping inwards toward the vertical pipe, and a crater-like morphology is observed on the upper paleosurface[4]. The spatial distribution of HTVC in the North Sea is shown as black dots in Fig. 2.4B.

In summary, HTVC form when magmatic sills intrude into sedimentary rocks containing water and organic matter. The heating of the sediments causes rapid maturation of the organic compounds and boiling of the pore fluids. The areas in which piercement structures form are well correlated with the emplacement of magmatic sills at depth. Within a HTVC brecciated rocks are observed. Both the structural and mineralogical observations (e.g. the occurrence of zeolites) indicate the involvement of large quantities of hydrothermal fluids.

2.1.3 Kimberlite Pipes

Going up in scales, Kimberlite pipes form when ascending volatile-rich[5] kimberlitic magma is decompressed, causing exsolution of fluids out of the magma leading to magmatophreatic[6] eruptions through the crust. This results in deeply rooted (150 km or more) explosions [102, 114-118].A schematic sketch of a Kimberlite pipe is seen in Fig. 2.5A and B.

Kimberlite structures are of economic interest since they contain diamonds that are brought up by the explosion. Detailed understanding of Kimberlite pipes is still in its infancy [118] when it comes to e.g. the underlying triggering mechanism. The depth of the pipes is inferred from the diamond stability zone [7] which is at pressures corresponding to depths exceeding 150 km and relatively low temperatures (i.e. typically not within the mantle which is too hot for diamonds).

Kimberlite magma rises through the crust through vertically oriented cracks (dikes). When it reaches a certain depth, of roughly a couple of kilometers, the inferred morphology of the eruption changes. There is a transition from the vertically oriented feeder dikes to a diverging cone-shaped structure [102]. Within the diverging conduit, fluidization of the rock fragments is identified to be the main deformation process of the eruption [114]. Identifying this morphological cross-over, from the penny-shaped cracks to the cylindrical fluidized zone, may be of great importance to understanding the eruption dynamics. It is proposed that as the magma de-compresses, chemical reactions and de-gassing accelerating the eruption rates. Thus the morphological response could be a function of the rate at which the system is driven and the physical properties of the fluids involved.

The morphology of the diverging conduit has traditionally been explained through fluidization experiments [e.g. 114, 102], although some 3 dimensional mapping has also been performed [101]. The diameter of the crater is up to $\sim$ 1km. Within the main Kimberlite crater a range of smaller meter and centimeter scale fluid escape structures are observed [119]. This indicates that fluidization

[4] A paleo-surface is the surface of the sedimentary package at the formation of the volcano.

[5] Volatility is a measure of the tendency of a substance to vaporize and undergo a volume increasing phase transition.

[6] A phreatic eruption occurs when rising magma makes contact with water that vaporizes creating massive volume changes accelerating of the fluids as they rise through the sediments.

[7] Sadly, diamonds do *not* last forever since pure carbon is unstable at atmospheric pressures.

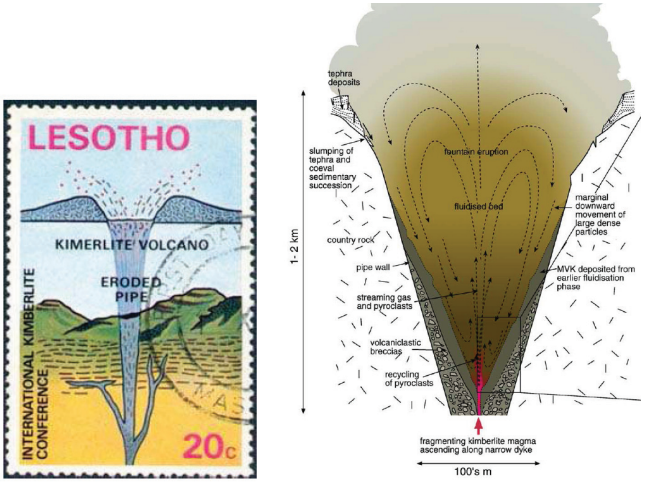

Figure 2.5: **(Left)** Schematic drawing of a Kimberlite pipe rooted at depth, from the 1973 Kimberlite congress in Lesotho. The stamp became famous because of its misspelling of the word Kimberlite. **(Right)** Sketch of the interpreted fluidization processes within the diverging conduit in the uppermost parts (upper km) of Kimberlite pipes. From Walters et. al 2006 Fig. 15 [102].

have led to sorting of the rock fragments after the main eruption. In Sec. 2.2.1 and in paper 1 we follow up on the pipes within pipes model first proposed Gilbertson and Eames 2001 [72] and Gernon et. al 2008 [119].

2.1.4 Pockmarks

Pockmarks, the round crater-like depression in the sea bed are widely recognized in offshore sedimentary basins throughout the world [120]. Pockmarks form when fluids, such as CH_4- and CO_2-gases and liquids, such as fresh ground water and pore water, are rapidly expelled through loose offshore sediments [97,121-123].The pockmarks may provide important information about the fluid flow on continental margins. Despite this, their formation mechanism is poorly understood [124]. The origin of the fluid over-pressure is debated and a number of triggering hypothesis have been proposed. For example, it is proposed that the pore-collapse of water bearing quick clay could generate rapid expulsion of the pore water [121]. Another formation mechanism is related to the de-stabilization of gas hydrates caused by either warmer water or the de-pressurization during the retreat of the ice cap after the last ice-age [124, 120], whilst a third formation mechanism may be expulsion of pressurized ground water through cracks in the under-lying bed-rock [122, 123].

Whatever the cause of the pressure build-up mechanism, which may be different from case to case, it seems likely that pockmarks are formed by sudden eruptions of gas, water and sediments and followed by long periods of micro-

seepage. There are at least two ways in which pockmarks may prevail sediment in-fill, one of which is mentioned in Sec. 1.6.2 where the ascending liquids prevents the sedimentation of fine particles within the pockmark. A second mechanism is related to the three-dimensional flow field in the water column above the pockmark. In this case vertical jets are formed when the water flows out of the depression downstream [125].

In addition to being interesting features from the physical and geological point of view, pockmarks have also been shown to be important for biological diversity because they act as refugees for benthic animals and fish in the North Sea [126]. The diameter of pockmarks ranges from 20-50 meter in size and depths of 2-10 meter [120]. In addition, pockmarks are often aligned, possibly indicative of a causal association between faults and flow localization in the underlying bedrock. The spatial density varies greatly from case to case, but pockmarks observed e.g. offshore Norway is on the order of 10-50 pockmarks forming pr. km^2.

The study of Pockmarks represents a very interesting cross-disciplinary field. Pockmark studies may include interaction between concepts from palaeontology, geology, ecology, biology and physics. There are several questions yet to be answered. Understanding the coupling between fluid flow, granular physics and the material strengths of sediments with varying degree of consolidation, are needed to study the triggering and the formation mechanisms.

2.1.5 Escape Pipes in Mud

Fig. 2.6A shows another example of the formation of pipe-like gas-escape structures in mud. The lens-cap, and the foot in the lower right corner, is included for scale. The image was taken during a field-work campaign to the Salton Sea gryphon field during December 2008. The location of this image is indicated by the circle in Fig. 2.2A. In the image $\sim$ 100 cylindrical black holes are interconnected by surface desiccation cracks (dark lines). Measurements on site shows the escaping gas is mainly CO_2. From the image it seems like distance to the nearest neighbor is controlled by the size of the gas escape structure; the larger holes drain a larger area around compared to the smaller ones. The drainage area inhibits the nucleation of new pipes in the vicinity of a pre-existing pipe. This shadowing effect can, presumably, explain the spatial distribution of pockmarks and HTVC in sedimentary basins, in general.

2.1.6 A Boiling Pot of Rice

Another example of pipe formation (this case a within a non-geological setting) which we are all familiar with, is observed in boiling pots of rice. Preliminary experiments have been performed and is shown in Fig. 2.6B. The volume expansion induced by vaporization of the water at the bottom of the pot increases the flow rate sufficiently to form cylindrical pipes or piercement structures. In Fig. 2.6B this is shown where $\sim$ 10 pipes are formed within the 15 cm diameter pot. The 'sediment thickness' is in this case four centimeter. Observations of the spatial distribution of 'gas escape pipes' indicate that the number of pipes decreases as the depth of the system increased.

Figure 2.6: **(Left)** Pipes forming as CO_2-gas is forced through mud in the Salton Sea seep localization (California, USA). The position of the image is indicated by the circle in Fig. 2.2**A**. **(Right)** Preliminary experiments showing how pipes form in a boiling pot of rice.

2.1.7 Summary of the observations

When fluids are expelled through sedimentary rocks piercement structures commonly forms. A variety of terms are used to describe these structures in the geological literature depending of the geological setting, the fluids and rock-types involved. In the examples above, HTVC, mud volcanoes, kimberlite pipes and Pockmarks are discussed. These structures form when the pressure build-up mechanism at depth is more rapid than the rate at which the pressure is released through undisturbed rocks. In this case, an unstable situation arises, where the fluid over-pressure increases, reaching a critical limit where the overlying sediments yield. Cylindrical pipes form with high permeability enabling rapid expulsion of pressurized fluids onto the surface.

A list of common properties of the observed piercement structures in nature is:

1. They are vertically oriented along the main pressure gradient with a large height to width ratio.

2. They are cylindrical in shape and have a sharp contact between the undisturbed solid rock matrix, and the pipes, containing intensely deformed rocks.

3. The piercement structures show a lack of internal structure. This trait is used to find them in seismic investigations [e.g. 98, 127].

4. They have an elevated permeability such that the bulk seepage occurs through these structures. The piercement structures may thus represent the primary source of fluid migration through sediments. For example, the HTVC in Karoo are used as aquifers and a source of ground water today, nearly 255 mya after their formation.

5. The surrounding matrix sometimes show inward dipping or upward bended (diapir) strata (especially for mud volcanoes and HTVC). These observations indicate that pressurized fluids are transported up while affecting the rock matrix. In the inward dipping case, material is brought up by the fluids through the central pipes, leaving voids behind causing the marginal sediments to collapse down by gravity. A convection-like pattern may thus be inferred.

Going from the km-scale Kimberlite volcanoes, via the tens of meter scale Pockmarks, to the cm-scale boiling pot of rice, suggest that this behavior occurs across scales. In the different systems the observed internal morphology is sometimes repeated, as pipes may form within pipes. This behavior has been documented within mud volcanoes [105], HTVC [99] and in Kimberlite volcanoes [119], giving further support for a general scale-independent mechanism for pipe formation.

2.2 Pipe Formation From a Physicists Point of View

Piercement structures in Nature have much in common. When facing these phenomena several questions arise that touches upon the physics of the formation of these structures:

1. Given that these structures are similar across scales, is there a common underlying physical mechanism forming them? If so, what is it?

2. What are the relevant physical parameters determining the critical conditions for pipe-formation in sedimentary basins? What is the relation between the 'internal properties' (permeability, viscosity, material strength etc.) and the 'external' conditions such as geometry (depth of the pressure source (i.e. sediment thickness) and lateral size of the pressure anomaly)?

3. Why is the contact between the cylindrical pipe and the undisturbed surrounded material so sharp?

4. Why are the pipes cylindrically shaped when the expected rheological response of crustal rocks or consolidated sediments to elevated fluid pressure would be the formation of penny-shaped hydraulic cracks?

5. Can fluidization of deformed rocks only occur if the pressure gradient is maintained? Is this a mechanism that could form the cylindrical geometry? See the Fig. 2.7 and Rigord et. al 2005 [65] where circular objects form when fluids (gas or water, respectively) forms gas escape structures in lab.

6. Can fluidization occur at pressures far less than the lithosthatic weight? In that case, how?

7. What is more important to pipe-formation in geology,- fluid pressures or fluid pressure gradients?

8. What is the association between faulting (the localization of tectonic stresses) and the formation of fluid escape structures? This issue is discussed in Sec. 3.2.2 and paper 3 [3].

In the appended papers some of these questions are discussed, other questions are touched upon in the remainder of this chapter, whilst others are not discussed beyond being raised here.

Figure 2.7: Preliminary experiment on the sublimation of dry-ice within a bed of fine particles triggered by heating through resistor treads. The image is 7 cm across. Circular gas-escape structures form.

2.2.1 Pipes within pipes

As mentioned in Sec. 1.6.2, gas escape structures are frequently observed within larger gas escape structures [99, 105, 119]. Gernon *et* al. [119] explained these observations by a feedback mechanism that was shown in experiments by Gilbertson and Eames in 2001 [72]. As a follow up on this work we did experiments showing how a family of vertical pipes formed in the partially gas-fluidized phase (Paper 1) [1]. A sketch of the feedback mechanism is seen in Fig. 2.8. Geological materials always have spatial variations in their physical properties. The pipes within pipes are proposed to form when flow is localized due to perturbations in the underlying permeability field. This causes a focusing of the fluidization such that size-segregation occurs only where the flow is sufficient to induce fluidization. As the large particles sediment down and the fine particles are expelled upwards, this enables further growth of the initial underlying permeability perturbation, which again leads to a subsequent flow localization and segregation. As this process continues, vertical pipes are proposed to form, which can later be observed in geological settings.

2.2.2 Under-fluidization

Is it really necessary to have a fluid pressures exceeding the lithostatic weight at the source of the fluids to form piercement structures in Nature? [1]

It has been argued that water vapor may induce fluidization only down to a certain depth, in the case of HTVC. In this case the weight of the overlying

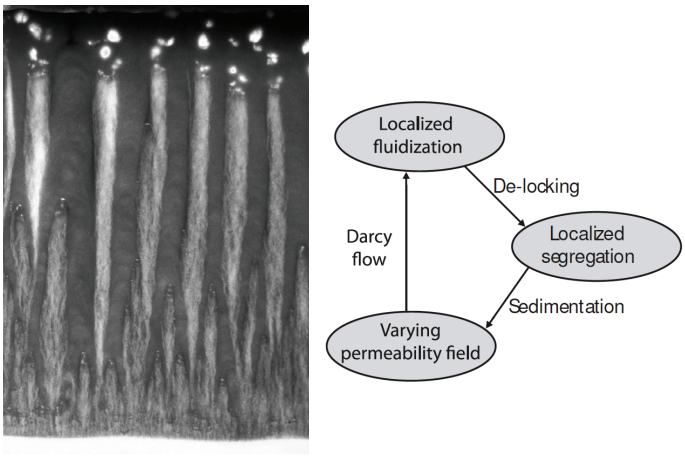

Figure 2.8: **(Left)** Picture of the Deeply Rooted Pipe-pattern (Paper 1). The experiment is performed on a vertically oriented HS-cell illuminated from behind. The HS-cell contains a mixture of large and small particles. Within areas where the number of reflected and refracted surfaces are reduced (associated with the large particles) the transmitted light intensity is increased. Flow is focused through the vertical, bright, high permeable zones. Fluidization (the white bubbles on top) is localized above the bright pipes. Within the fluidized zones segregation occur [1]. **(Right)** Sketch of the proposed feed back mechanism.

column of rocks exceeds the pressure of the critical point of water[8] [99]. For the deep HTVC, it is therefore said that boiling of water cant be the formation mechanism since the pressure at the critical point is insufficient to lift the bed. Thus, fluidization driven by vaporized water can only form the shallow HTVC. In the following I take a critical look at this fluidization criterion.

The question of what the critical conditions for fluidization might be is touched upon in both paper 1 and 2 [1, 2]. In paper 2 we show that in the presented experiments, the critical conditions for fluidization depends on imposed gas velocity v_f[9] instead of the fluid pressure [2]. From the experiments we showed that v_f scaled with the ratio of the filling height to the size of the inlet (h/w). Combining this result with the analytic solution of the Laplace pressure field with corresponding conditions, we calculated the critical over-pressure for fluidization at the pressure source,

$$P_c^{op} = (\rho_b - \rho_f) g \beta \left(\frac{h}{w}\right)^{\xi} \frac{2}{\pi} \int_0^{\infty} \frac{\sin(\tilde{k}w)\tanh(\tilde{k}h)}{\tilde{k}^2} d\tilde{k}, \tag{2.1}$$

This equation is discussed deliberately in paper 2, and it is re-stated here to

[8]The critical point of water occurs at 647 K and 22.1 MPa which roughly corresponds to the pressure below ∼1.1 km of rocks.

[9]In that case we considered the Darcian flow velocity which was calculated from the flux (Q) through the inlet, divided by the cross sectional area (wb) and the porosity (ϕ), $v_f = Q/(bw\phi)$.

show that the critical pressure is not only given by the weight of the overlying sediments [2].

Moreover, in the case with spatial variations in the permeability, the nucleation of pipe pattern (NP-pattern, see Fig. 2.9A and paper 1)[10] occurred at pressures less than the weight of the particles [1]. The onset of this pattern occurred at the critical velocity v_{f1} , a decreasing function of the mixing concentration of small particles. The corresponding bulk permeability k was estimated using Darcys law from the ratio of the measured pressure and imposed gas velocity. Re-scaling the critical velocity by the bed permeability, the fluid viscosity and the weight of weight of the bed, we defined the reduced pressure ($\tilde{P}$) as,

$$\tilde{P} = \frac{v_{f1}\eta}{k\rho g}. \tag{2.2}$$

We found that the triggering of the NP-pattern occurred at $\tilde{P} \simeq 0.76$ (see Fig. 2.9**(B)**) which indicate that the pressures needed to induce the NP-pattern is significantly less than the weight of the overlying sediments.

The phenomenon that fluidization may be triggered at pressures less than the weight of the overlying sediments, is termed under-fluidization. We propose that this mechanism may be relevant for a wide range of piercement structures in geology. In the underfluidized phase, fluidization occurs locally triggered by heterogeneities in the permeability and the corresponding flow field. In that case the gradients in the fluid pressures, and its effect on the local stress tensor, needs to be considered (see Chapter 2). Under-fluidization and the localization of fluidized zones may be the dominating system scale behavior before any full-scale fluidization occurs. When a pipe-like feature forms, it effectively drains the basins, preventing the fluid over-pressure to reach the weight of the overburden [1].

2.2.3 Pressures or Pressure Gradients - Seepage Forces in Geology

Seepage forces, that a fluid seeping through a porous matrix imparts a force onto the solid body, are here treated equivalent to the effect of fluid pressure gradients. This issue is discussed in chapter 3. Using the pressure gradients in relation to the solid matrix is commonly done in the physics literature, cf. Sec. 1.7. But including pressure gradients in the evaluation of the total stress tensor is seldom done to explain geological phenomena [59, 128]. There are a few important exceptions such as [53,58,59,129] where they included the effects of fluid pressure gradients.

In geo-technical engineering the weakening of rocks is understood through the Mohr-circle where the circle shifts down for increasing fluid pressure. In the case of no fluid pressure gradients, the size of the circle remains constant since the radius was given by difference $\sigma_{33} - \sigma_{11}$. When fluid pressure gradients are important, however, this is no longer the case. Gradients of the pressure field, is a vector quantity, a normal force that affects the normal stresses in the stress tensor. Any gradients in the fluid pressure field will change the radius of the

[10]The NP-pattern was one of the family of segregation patterns forming in the gas-fluidized phase documented in paper 1.

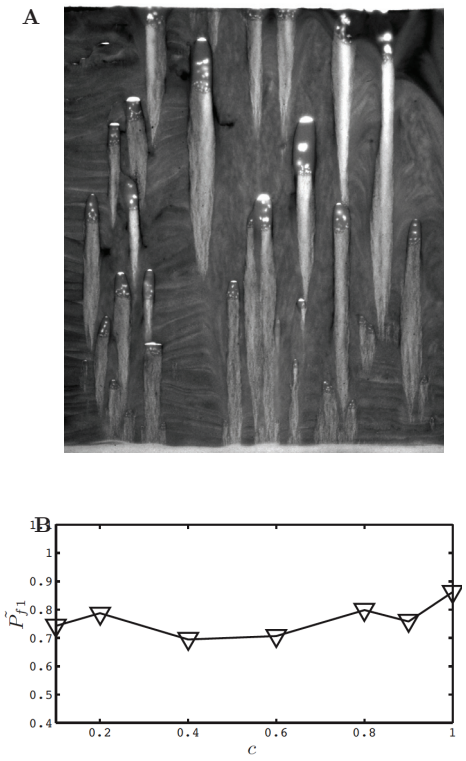

Figure 2.9: **A** Image of the nucleation of pipe pattern forming in the partially gas-fluidized phase. **B** The reduced pressure at formation.

Mohr-circle and cause yielding in situations that would otherwise be considered to be stable.

Depending on the specific situation, the fluids involved, the rate at which the system is driven, and the deformed matrix a range of fluid induced deformation mechanisms are available. Examples include the formation of porosity waves [e.g. 130][11], hydraulic fracturing[12] and fluidization where the matrix starts behaving in a liquid-like manner. In the experiments presented in paper 1 and 2, the fluid pressure gradient is the critical parameter for fluidization [1, 2]. It is likely that seepage forces plays an important role in the emplacement of piercement structures in Nature, and that the commonly used proxy for fluidization, that the fluid pressure must exceed the lithostatic weight (at the source), needs to be re-considered.

[11] Porosity waves occur when the pore space increases in response to the fluid over-pressure due to a compaction of the solid component of the continua.

[12] Hydraulic fracturing occur when fluid pressure exceeds the tensile strength of a material. Tensile cracks grow in the direction of the largest principal stress.

Chapter 3

Relating Fluid Pressures to Rock Deformation

In this chapter the relation between fluid pressures, fluid pressure gradients and rock deformation in geology is discussed. The discussion is based on Mourgues and Cobbold 2003, where they show some of the tectonic consequences of fluid over-pressure and seepage forces in sand box models [59]. Concepts from continuum mechanics are used to develop a general coupling theory of fluid pressures (P_f), fluid flow v driven by pressure gradients, and the solid stress tensor (σ^s). In the laminar (Darcian) regime, the flow velocity within a porous bed is proportional to the gradient in the fluid pressure, the permeability of the bed and inversely proportional to the viscosity of the fluid. We will calculate the momentum balance despite the non-linear effects of force chains and Jansen wall effects observed in static granular beds. These non-linear effects have shown to introduce significant perturbations to the stress tensor. As such, writing down the stress tensor in granular material with continuum models may therefore flaw from the beginning without playing with funny rheologies and complicated feed back mechanisms (see Sec. 1.2.2). Despite that, *we try anyway*, such that we can evaluate the relative importance. The non-linear effects do not need to be important in the case when a vertically flowing fluid imparts a force onto the solid skeleton in the opposite direction to gravity. We propose a scenario where, as the vertical flow velocity increases, and the system approach fluidization conditions, the apparent weight of the bed is drastically reduced such that the importance of e.g. force chains may vanish.

We make the simplifying assumption that fluidization conditions are met in the quasi-static limit. The quasi static limit is in this case defined when the buoyant weight of the bed is counteracted by the total drag (on the solid component) of the fluids flowing through the packing (see Fig. 3.1). Now, the drag is proportional to the incipient flow velocity, and fluid viscosity and inversely proportional to the permeability of the bed. Through Darcy's law this is equivalent to the pressure gradient, on local form. This concept is used to predict the minimum velocity of fluidization, as first shown by Ergun [94] and Kunii and Levenspiel [61]. This concept is employed to evaluate of the critical velocity of fluidization. In paper 2 this concept is used to predict the scaling of the critical velocity as a function of the ratio of the filling height and the inlet

width, h/w [2]. As described above, we did dimensional analysis and discussed the critical conditions for fluidization. In addition, we found a semi-analytical solution for the critical velocity in static conditions as the geometry of was changed. A good correspondence between the experimental measurements and the model was obtained.

We used the same concept in paper 3 of this thesis [3], where the analytic form of the critical velocity of fluidization was calculated both as a function of the buoyant weight and the presence of shear stresses. The presented model captured the observed dynamic, i.e. that pipes tend to form along faults (which represent the localizations of shear stresses) in over-pressured sediments. The observations presented in chapter 2, paper 2 and paper 3, indicate that the concept of fluid induced deformation may represent a promising tool in earth sciences and geology to predict the critical conditions of fluidization. In the coming section the derivation is shown.

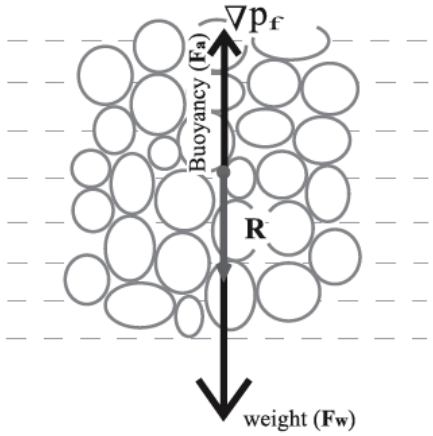

Figure 3.1: Sketch of the mesoscopic scale in which the mean field concept apply. The buoyant weight and the viscous drag induced by the gradients in fluid pressure are included into the drawing. The interior of the circle represents the incremental volume Ω_t bounded by the surface $\partial\Omega$. The image is from Mourgues et al. 2003 [59].

3.1 Momentum Conservation in a Two Phase Granular Media

This section deals with the coupling of the momentum equations of a two-phase media consisting of a solid phase with an interstitial fluid phase (see Fig. 3.1). The force balance is performed at a scale in which the fluctuations in the material properties, that being e.g. porosity (ϕ), densities (ρ^s and ρ_f)

and stresses (σ^s), are less important than the mean quantity[1]. We define the incremental volume (Ω_t) as a volume in which this approximation is valid. Its size will vary from case to case[2], and obtaining a precise general definition of the mesoscopic scale in granular materials is beyond the scope of this work. This incremental volume, whatever it may be, is meant to bring the discussion from a 'microscopic' granular picture, in which each particle is considered, to a macroscopic 'grey-scale' picture where mean field concepts apply. This volume is enclosed by a surface with an area $\partial^f\Omega$.

It is interesting to check to what extent models based on a simple momentum balances can predict the critical conditions of fluidization. I will derive the momentum equation of a two-phase media where the total stress state is considered to be a superposition of two continuum phases, the solid and the fluid. The two phases interact through a momentum exchange factor R where each continua moves with distinct kinematics. We make the assumption that the fluid continuum is connected, i.e. what is termed drained systems. Superscripts are associated with the phase and the subscripts indicate indexes in the tensorial objects.

Considering the momentum balance of the volume Ω_t containing the two phases. The acceleration (dv/dt) of a fluid within Ω_t is given by the total (integrated) body force (over dV) and the surface forces (over dA), and can be written,

$$\frac{d_f}{dt}\int_{\Omega_t}\rho^f\phi v_j^f dV = \int_{\Omega_t}\rho^f\phi f_j dV + \int_{\partial^f\Omega}\sigma_{ij}^f n_i da + R_j^{sf}, \tag{3.1}$$

where the left hand side (lhs) represents the acceleration induced by the sum of all body forces and surface forces on the right hand side (rhs). Here, ϕ is the porosity, ρ^f is the fluid density, v_j^f is the fluid velocity vector, f_j is the body forces acting on the centre of mass, σ_{ij}^f is the fluid stress tensor and R_j^{sf} is the force acting from the solid onto the fluid. Similarly, the solid momentum balance states,

$$\frac{d_s}{dt}\int_{\Omega_t}\rho^s(1-\phi)v_j^s dV = \int_{\Omega_t}\rho^s(1-\phi)f_j dV + \int_{\partial^s\Omega}\sigma_{ij}^s n_i da - R_j^{fs}, \tag{3.2}$$

where $(1-\phi)$ is the fraction of solid particles within the incremental volume, ρ^s is the solid density, v_j^s is the velocity of the solid, σ_{ij}^s is the solid stress tensor, and $\partial^s\Omega$ is the surface of the solid around the incremental volume. The force exchange vector R_j^{fs} is equal but opposite directed to the one in the fluid equation ($R_i^{sf} = -R_i^{fs}$).

We make the assumption that the total surface $\partial\Omega$ of the incremental volume is related to the partial surfaces through,

$$\partial\Omega = \frac{\partial^s\Omega}{1-\phi} = \frac{\partial^f\Omega}{\phi}, \tag{3.3}$$

such that the limits of the surface integral in Eq. 3.1 and Eq. 3.2 change to,

$$\int_{\partial(1-\phi)\Omega}\sigma_{ij}^s n_i da \quad \text{and} \quad \int_{\partial\phi\Omega}\sigma_{ij}^f n_i da. \tag{3.4}$$

[1] See Sec. 1.2.2 for a discussion on the mesoscopic scale in granular materials. Since e.g. force chains, that introduce significant perturbations to the stress field, may span the whole system, such a length scale may not exist.

[2] In paper 2 the incremental volume is the whole truncated wedge forming above the inlet [2].

The surface integrals ($\partial\Omega$) is replaced by a volume integral (Ω_t) via,

$$\int_{\Omega_t} \frac{\partial(1-\phi)\sigma^s_{ij}}{\partial x_i} dV \quad \text{and} \quad \int_{\Omega_t} \frac{\partial \phi \sigma^f_{ij}}{\partial x_i} dV \tag{3.5}$$

Adding the fluid and solid momentum equation gives,

$$\frac{d_s}{dt}\int_{\Omega_t} \rho^s(1-\phi)v^s_j dV + \frac{d_f}{dt}\int_{\Omega_t} \rho^f \phi v^f_j dV = \int_{\Omega_t} \rho f_j dV + \int_{\Omega_t} \frac{\partial \sigma_{ij}}{\partial x_i} dV, \tag{3.6}$$

where we have used the stress partitioning theorem and defined the total stress as $\sigma_{ij} = \phi\sigma^f_{ij} + (1-\phi)\sigma^s_{ij}$, where the bulk density $\rho = \rho^f\phi + \rho^s(1-\phi)$ is introduced.

Assuming that the momentum balance holds for any choice of Ω_t, the total momentum balance reads,

$$\frac{d_s}{dt}\left(\rho^s(1-\phi)v^s_j\right) + \frac{d_f}{dt}\left(\rho^f\phi v^f_j\right) = \rho f_j + \frac{\partial \sigma_{ij}}{\partial x_i}. \tag{3.7}$$

To limit the discussion I make the simplifying assumption that $\partial\phi/\partial t = \partial\rho^s/\partial t = \partial\rho^f/\partial t = 0$. By using Reynolds transport theorem for the full derivatives, the momentum balance equation of a two-component media attains the form,

$$\rho^s(1-\phi)\left(\frac{\partial v^s_j}{\partial t} + v^s_j\frac{\partial v^s_i}{\partial x_i}\right) + \rho^f\phi\left(\frac{\partial v^f_j}{\partial t} + v^f_j\frac{\partial v^f_i}{\partial x_i}\right) = \rho f_j + \frac{\partial \sigma_{ij}}{\partial x_i}. \tag{3.8}$$

The left hand side denotes the acceleration of the solid and fluid induced by the sum of the body forces and surface forces acting on the volume elements.

3.2 Fluidization Conditions in Density Controlled Systems

I propose that mean field concepts may provide an approximate understanding of the stress state in a granular bed when a fluid is injected into a bed in a direction opposite to gravity. The mechanical behavior of dry, non-cohesive granular materials depends upon the interaction between the particles, the gas-particle interaction and the effects of the body forces such as Earths gravitational field. In the following we assume that the frictional strength of dry, cohesion less, non-fluidized granular beds are described by the Mohr-Coulomb rheology (see sec 1.5.2). Fluidization (or liquefaction) occurs when the granular bed has negligible shear strength and is not able to resist any shear stresses (this is in it self a definition of a fluid). In this case density effects become increasingly important and the material 'acts' as a fluid. The normal stress onto an arbitrary plane directed along $\mathbf{n}$ at an angle α versus the horizontal direction can be calculated from the vertical stresses under plane strain conditions,

$$\sigma_{\mathbf{n}} = \sigma_{33}(\kappa \sin^2\alpha + \cos^2\alpha), \tag{3.9}$$

where κ is the coefficient of side stresses related to the Poisson ratio (ν), through,

$$\kappa = \frac{\nu}{1-\nu} \tag{3.10}$$

Here, ν is a material property measuring how a sample stretches (or contracts) perpendicular to the applied strain.[3] The vertical stress can thus be included into Eq. 1.4 such that the shear strength attains the form of,

$$\tau = \mu\sigma_{33}^{s}(\kappa \sin^2\alpha + \cos^2\alpha). \tag{3.11}$$

The quasi-static approximation states that the fluid or grain acceleration on the left hand side of Eq. 3.8 is zero. In this case the body forces and the stress gradients balance out such that Eq. 3.8 simplifies to,

$$\rho f_j = -\frac{\partial \sigma_{ij}}{\partial x_i}. \tag{3.12}$$

When gravity is the only body force and the coordinate system is directed such that $f_j = (0, 0, -g)$ I can evaluate the equation in the $j = 3$-direction,

$$\rho g = \frac{\partial \sigma_{i3}}{\partial x_i}. \tag{3.13}$$

By using the stresses for the two components separately, i.e. using Eq. 1.2 for the solid and assuming that the fluid component of the stress tensor can be written $\sigma_{ij}^{f} = -P^{f} I_{ij}$, where I_{ij} is the identity matrix I get,

$$\rho g = -\phi\frac{\partial P^{f}}{\partial x_3} + (1-\phi)\frac{\partial \sigma_{i3}^{s}}{\partial x_i}. \tag{3.14}$$

3.2.1 Fluidization Without Shear Stresses

In a system with (initially) negligible shear stresses, the off diagonal elements are set to zero. Considering the force balance in the $j = 3$-direction Eq. 3.14 simplifies to,

$$\rho g = -\phi\frac{\partial P^{f}}{\partial x_3} + (1-\phi)\frac{\partial \sigma_{33}^{s}}{\partial x_3}. \tag{3.15}$$

The normal stress in the vertical direction at depth h can now be found by integration,

$$\sigma_{33}^{s}(h) = \int_0^h \left(\frac{\rho g}{1-\phi} + \frac{\phi}{(1-\phi)}\frac{\partial P^{f}}{\partial x_3}\right) dz'. \tag{3.16}$$

At the onset of fluidization the shear strength in Eq. 3.11 is zero, implying that both $\sigma_{\mathbf{n}}^{s}$ and σ_{33}^{s} are zero. Now σ_{33}^{s} is zero only if the integrand of Eq. 3.16 is zero. This occurs when following condition is met,

$$\rho g = -\phi\frac{\partial P^{f}}{\partial x_3}. \tag{3.17}$$

This equation enables us to quantify the critical pressure gradient of fluidization on a local form as,

$$\frac{\partial P^{f}}{\partial x_3} = -\frac{\rho g}{\phi}. \tag{3.18}$$

[3]The Poisson ratio is defined as the ratio of the translator and axial strains as $\nu = -\epsilon_{trans}/\epsilon_{axial}$.

The gradient in the fluid pressure is associated with the flow velocity through Darcys law within a porous permeable media,

$$v_f = -\frac{k}{\eta}\nabla P^f \tag{3.19}$$

In the case when the main pressure gradient is vertical the ∇ operator can be replaced by $\partial/\partial x_3$. Combining Eq. 3.19 with Eq. 3.18 enables us to calculate the critical velocity of fluidization v_c as,

$$v_c = \frac{k\rho g}{\phi\eta}, \tag{3.20}$$

which we recognize is equivalent to the Kunii and Levenspiels [61] minimal velocity of fluidization.

3.2.2 Fluidization With Shear Stresses

In geology, piercement structures have often been observed in association with shear zones [3] (paper 3 in this thesis). This relation may have implications to the understanding of the triggering mechanism for the Lusi mud volcano (Java, Indonesia) that was 'born' the 28th of May 2006 [106]. The triggering mechanism for this evolving catastrophe in which three villages were flooded and ∼30 000 lost their home has been debated in the Earth science literature. Two main hypotheses for triggering mechanism were raised in the period after the eruption. In the first hypothesis, the triggering was caused by errors in the drilling procedure. Specifically the lack of casing, a cylindrical steel pipe used to strengthen the structural stability of a borehole, would make the borehole more susceptible to breaking and developing into a non-stopping volcanic feature. The detailed arguments for this hypothesis were addressed in a range of articles [e.g. 108, 109].

Here the discussion is focused on the hypothesis that the triggering of the eruption was caused by re-activation of a strike-slip fault crossing the area prior or simultaneously to the formation of the eruption [106]. It is in that context interesting to study the relation between the critical conditions for fluidization and the localization of shear stresses. In paper 3 we did an integrated study including fieldwork, analogue experiments, analytic and numeric modeling of this concept [3]. Here I will go through a similar analysis as in paper 3, within the framework that we have developed previously in this chapter. We will do this analysis in the same way as for Eq. 3.18, but here we will simply keep one of the off-diagonal terms in the σ^s_{ij}-tensor and evaluate its importance to v_c.

Considering the quasi static approximation, where the gravitational body force is balanced by the gradients in stresses and fluid pressure, Eq. 3.14 attains,

$$\rho g = -\phi\frac{\partial P^f}{\partial x_3} + (1-\phi)\left(\frac{\partial \sigma^s_{33}}{\partial x_3} + \frac{\partial \sigma^s_{23}}{\partial x_2}\right). \tag{3.21}$$

See Fig. 3.2A for a conceptual picture. In a density controlled, frictional system the shear strength can be estimated using Eq. 3.11 such that at fluidization, the shear strength drops to zero. This implies that the normal load $\sigma_{\mathbf{n}}$, and correspondingly σ^s_{33}, both are zero. Similarly to above, I solve Eq. 3.21 with respect to σ^s_{33}, integrate and set its value to zero at fluidization. σ^s_{33} is zero only

if the integrand is zero such that the functional form of the critical velocity at fluidization is attained by Darcy's law,

$$v_c = \frac{k}{\eta}\frac{(1-\phi)}{\phi}\left(\frac{\rho g}{(1-\phi)} - \frac{\partial \sigma_{32}}{\partial x_2}\right). \tag{3.22}$$

In this case we see that the critical velocity of fluidization is reduced in the presence of shear stresses.

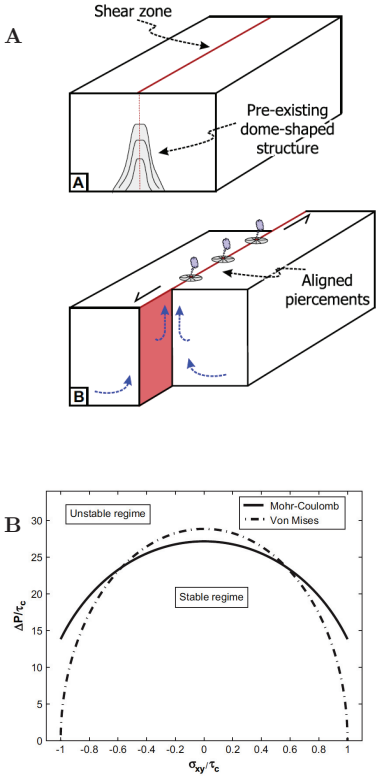

Figure 3.2: **(A)** Schematic cartoon of eruptions along strike-slip faults. A shear zone crossing through a region with pressurized fluids. **(B)** Localization of shear stresses reduces the critical pressure of fluidization, triggering fluidization and pipe-formation in situations that could otherwise be stable. Both figures are from paper 3 [3].

3.2.3 Effective Stresses and Terzaghis Principle

Terzaghi's principle (see sec. 1.6), that the effective stress within a porous packing equals the solid stress minus the fluid pressure

$$\sigma' = \sigma_m - P^f, \tag{3.23}$$

is implicitly included in the presented theory by integrating the momentum balance in Eq.3.14 in the one dimensional case. In density controlled systems, the effective stress is simply the buoyant weight minus the difference in pressure difference across the sand pile with depth h,

$$\sigma^s = \frac{\rho g h}{(1-\phi)} - \frac{\phi}{(1-\phi)}\Delta P^f. \tag{3.24}$$

As such, the shear strength ($\tau = \mu\sigma^s$) at depth h, is reduced when the fluid pressure is increased within the packing compared to the cases without fluid over-pressure.

3.3 Mission Statement and Overview

The interplay between fluid flow and granular material coupled to deformation of the material has been the topic of this thesis. The purpose of this work has been to gain an integrated understanding of granular physics and fluid flow with applications to geological examples. Despite all the non-linearitys and intriguing and rich phenomena in granular physics, my approach to the topic has been different than the usual now days in the physics community. I have taken a step back to evaluate the effectiveness of medium theories to simple experiments on granular matter.

Chapter 1 included examples which gave an over-view of surface processes and internal 'bulk' processes. The articles in the thesis focus on the internal processes, i.e. how the fluid pressure and fluid flow, imparts deformation onto the solid body. More specifically, how pressurized fluids fluidize the granular material and form piercement structures both in laboratory experiments and in the geological environment. In chapter 2 observations from several geological examples were presented. The different cases displayed significant similarities despite the wide range of scales, fluids, and materials involved. This suggests that a general underlying formation mechanisms are at play. In chapter 3 how a two-phase media, each phase moving with distinct kinematics, may be coupled using of the momentum conservation equation. The phase-field approach, of using conservation equations (of mass, momentum and energy) and the non-conservation of the entropy equation, to couple n phases is widely used in poromechanics literature.

In the appended papers, which are the main body of the thesis, the interaction between incipient fluid flow and its effect on the solid skeleton of grains are studied through a series of experiments and theoretical mean field models. The physical insight gained has been used to understand a range of phenomena observed in the geological record.

Within the papers special emphases have been on:

(a) The pipes within pipes forming when mixtures of particles de-mix in the partially fluidized regime, as discussed in paper 1 [1].

(b) Evaluation of the critical conditions for the formation of piercement structures. This was discussed in paper 2 for static conditions [2]. In addition, it is partially discussed in paper 1 where the concept of under-fluidization, i.e. that fluidization can occur at fluid pressures far less than the lithostatic weight previously used as the proxy for pipe formation, is introduced.

(c) The relation between strike-slip faulting and fluidization. How does the localization of shear stresses affect the critical pressure for gas-induced fluidization? In paper 3 this concept is addressed to the birth of the Lusi mud volcano, Java (Indonesia) [3].

3.3.1 The Way Forward

There is nearly an in-exhaustive amount of geological and geomorphology examples in which the coupling between granular physics and fluid flow can be employed. Based on the presented work, further work could focus upon some key, unanswered questions such as:

(a) What is the importance of the cross-over from Darcian flow in porous beds to Stokes- and Navier-Stokes flow in open cracks, bubbles or chimneys?

(b) What determines the cross-over from fluidization to fracturing, the "morphological phase transition", in the material response to localized elevated fluid pressures?

(c) Why are pipes observed in geology often cylindrical in shape, with such a sharp transition between an intensively deformed interior and a presumably undisturbed surrounding? How can the cylindrical shape form when fluids are expelled through the brittle crust?

(d) What is the underlying mechanism for the formation of Pockmarks in offshore sediments? Why do they resist erosion?

(e) What is the physical mechanism determining the spacing of piercement structures in geological systems?

(f) What is the meso-scopic scale in granular materials, the scale in which fluctuations in mean field quantities are negligible? Does a mesoscopic scale exist at all? If not, what are the implications?

(g) Can we accurately model the pipe-formation observed in paper 1? More work is needed to quantify the pattern and the rates at which it grows.

(h) More work is needed to quantify the concepts of *under-fluidization* and *partial fluidization* discussed in paper 1. What is the importance of heterogeneities at various scales?

(i) As a development on the model in paper 2, I suggest estimating the critical fluidization pressure difference in a three dimensional model. This may provide more realistic values to estimates of critical pressures in geological settings.

(j) What role do chemical processes play, if any, in the formation of pipes in geology?

(k) The relation between localization of shear stresses and the critical pressure of fluidization needs to be understood (paper 3). Controlled experiments quantifying this relation are needed.

When facing a natural phenomena[4], some of which mentioned in the previous chapters, a cross-disciplinary approach is needed. For example in the case of pipe formation a combined knowledge is needed to fully understand the processes at play. In addition to having the combined knowledge, this knowledge has to be applied correctly to the practical examples, both in experiments and in the 'dirty old world'. Experimental, numerical and analytic investigations are still in its infancy when facing a complete understanding of a wide range of geological cases.

[4]As a physicist, geophysicist, geologist or whatever I may be called, I will defend the viewpoint that *everything is physics* and that *Nature is my laboratory*.

Bibliography

[1] A. Nermoen, C. Raufaste, S. D. deVilliers, E. Jettestuen, P. Meakin, D. K. Dysthe. Morphlogical Transitions in Partially Gas-Fluidized Granular Mixtures *Phys. Rev. E,* **81***, 061305, 2010*

[2] A. Nermoen, O. Galland, E. Jettestuen, K. Fristad, Y. Y. Podladchikov, H. Svensen, A. Malthe-Sørenssen Experimental and Analytic Modelling of Piercement Structures. Accepted in *J. of Geophys. Res., 2010.*

[3] A. Mazzini, A. Nermoen, M. Krotkiewski, Y. Podladchikov, S. Planke, and H. Svensen. Strike-slip faulting as a trigger mechanism for overpressure release through piercement structures. Implications for the Lusi mud volcano, Indonesia. *Mar. Pet. Geol.*, 26(9):1751–1765, NOV 2009.

[4] A. Mazzin, M. K. Ivanov, A. Nermoen, A. Bahr, G. Bohrmann, H. Svensen, S. Planke Complex plumbing systems in the near subsurface: Geometries of authigenic carbonates from Dolgovskoy Mound (Black Sea) constrained by analogue experiments. *Mar. Pet. Geol.*, 25 (6):457–472, 2008

[5] E. Jettestuen, A. Nermoen, G. Hestmark, E. Timdal, and J. Mathiesen. Competition on the rocks: Community growth and tessellation, 2010. Accepted in *PLoS ONE.*

[6] S. deVilliers, A. Nermoen, L. Angheluta, and E. Jettestuen. Fold formation in a non axially confined thin walled cylinder, 2010. Submitted to *Experimental Mechanics.*

[7] H. Svensen, E. Jettestuen, A. Nermoen, and Ø . Hammer. Distribution of vents constrained by numerical modelling in the Karoo basin, South Africa, 2010. *In prep.*

[8] S. deVilliers, A. Nermoen, and S. Werner. Experimental Constraints on the "Spiders on Mars", 2010. *In prep.*

[9] J. Duran. *Sands, Powders and Grains*, vol. 391. Springer-Verlag New York, Inc., 2000. ISBN 0-387-98656-1, Sec. Ed.

[10] T. Divoux, H. Gayvallet, and J.-C. Geminard. Creep motion of a granular pile induced by thermal cycling. *Phys. Rev. Lett*, 101(14), OCT 3 2008.

[11] R. A. Bagnold. *The physics of blown sand and desert dunes*, volume 391. London: Methuen, 1941.

[12] B. Andreotti and P. Claudin Selection of dune shapes and velocities. Part 2: A two-dimensional modelling. *Eur. Phys. J. B*, Jan 2002. arXiv:cond-mat/0201105v1.

[13] B. Andreotti, A. Fourriere, F. Ould-Kaddour, B. Murray, and P. Claudin. Giant aeolian dune size determined by the average depth of the atmospheric boundary layer. *Nature*, 457(7233):1120–1123, FEB 26 2009.

[14] H. Nishimori and N. Ouchi. Formation of ripple patterns and dunes by wind-blown sand. *Phys. Rev. Lett.*, 71(1):197–200, Jul 1993.

[15] A. Betat, C. A. Kruelle, V. Frette, and I. Rehberg. Long-time behavior of sand ripples induced by water shear flow. *Eur. Phys. J. E*, 8(5):465–476, AUG 2002.

[16] V. Frette, K. Christensen, A. Malthe-Sørenssen, J. Feder, T. Jossang, and P. Meakin. Avalanche dynamics in a pile of rice. *Nature*, 379(6560):49–52, JAN 4 1996.

[17] J. D. Pelletier, B. D. Malamud, T. Blodgett, and D. L. Turcotte. Scale-invariance of soil moisture variability and its implications for the frequency-size distribution of landslides. *Eng. Geol.*, 48(3-4):255 – 268, 1997. Fractals in Engineering Geology.

[18] T. C. Halsey and A. J. Levine. How sandcastles fall. *Phys. Rev. Lett*, 80(14):3141–3144, APR 6 1998.

[19] E. Altshuler, O. Ramos, C. Martinez, L. E. Flores, and C. Noda. Avalanches in one-dimensional piles with different types of bases. *Phys. Rev. Lett*, 86(24):5490–5493, JUN 11 2001.

[20] H. A. Makse, N. Gland, D. L. Johnson, and L. M Schwartz. Why effective medium theory fails in granular materials. *Phys. Rev. Lett*, 83(24):5070–5073, DEC 13 1999.

[21] B. Cagnoli and G. P. Romano. Effect of grain size on mobility of dry granular flows of angular rock fragments: An experimental determination. *J. Volc. and Geotherm. Res.*, In Press, Accepted Manuscript:–, 2010.

[22] Y. M. Zhao and L. B. Wei. Rheology of gas-solid fluidized bed. *Fuel Proc. Tech.*, 68(2):153–160, NOV 2000.

[23] S. C. Colbeck. An overview of seasonal snow metamorphism. *Revs. of Geophys. and Space Phys.*, 20(1):45–61, Feb 1982.

[24] K. Kristensen. Håndbok for observatører. vær-, snø-, og snøskredobservasjoner, 2007. Norges Geotekniske Institutt, Internal Report.

[25] D. Lague, A. Crave, and P. Davy. Laboratory experiments simulating the geomorphic response to tectonic uplift. *J. Geophys. Res.*, 108((B1)), 2003.

[26] A. D. Howard. A detachment-limited model of drainage-basin evolution. *Water Resources Research*, 30(7):2261–2285, JUL 1994.

[27] A. Daerr, P. Lee, J. Lanuza, and E. Clement. Erosion patterns in a sediment layer. *Phys. Rev.E*, 67(6, Part 2), JUN 2003.

[28] C.F. Harwood. Powder Segregation due to Vibration. *Powder Technol.*, 16(1):51–57, 1977.

[29] E. Clement and J. Rajchenbach. Fluidization of Bidimensional Powder. *Europhys. Lett.*, 16(2):133–138, SEP 7 1991.

[30] A. Kudrolli, M. Wolpert, and J. P. Gollub. Cluster formation due to collisions in granular material. *Phys. Rev. Lett*, 78(7):1383–1386, FEB 17 1997.

[31] M. Schroeter, S. Ulrich, J. Kreft, J. B. Swift, and H. L. Swinney. Mechanisms in the size segregation of a binary granular mixture. *Phys. Rev.E*, 74(1, Part 1), JUL 2006.

[32] M. A. Kessler and B. T. Werner. Self-organization of sorted patterned ground. *Science*, 299(5605):380–383, JAN 17 2003.

[33] M. E. Mbius, B. E. Lauderdale, S. R. Nagel, and H. M. Jaeger. Size separation of granular particles. *Nature*, 414(270), 2001.

[34] M. Alam, L. Trujillo, and H. J. Herrmann. Hydrodynamic theory for reverse Brazil nut segregation and the non-monotonic ascension dynamics. *J. of Stat. Phys.*, 124(2-4):587–623, AUG 2006.

[35] Q. Shi, G. Sun, M. Hou, and K. Lu. Density-driven segregation in vertically vibrated binary granular mixtures. *Phys. Rev.E*, 75(6, Part 1), JUN 2007.

[36] L. Chang-Hong, S. Qing-Fan, Y. Lei, and S. Gang. Air-driven segregation in binary granular mixtures with same size but different densities. *Chinese Phys. Lett.*, 25(7):2542–2545, JUL 2008.

[37] J. J. Wylie, Q. Zhang, H. Y. Xu, and X. X. Sun. Drag-induced particle segregation with vibrating boundaries. *EPL*, 81(5), MAR 2008.

[38] C. Liu, L. Wang, P. Wu, and M. Jia. Effects of Gas Flow on Granular Size Separation. *Phys. Rev. Lett*, 104(18), MAY 7 2010.

[39] D. M. Mueth, G. F. Debregeas, G. S. Karczmar, P. J. Eng, S. R. Nagel, and H. M. Jaeger. Signatures of granular microstructure in dense shear flows. *Nature*, 406(6794):385–389, JUL 27 2000.

[40] A. Aydin. Small faults formed as deformation bands in sandstone. *Pure and Appl. Geophys.*, 116(4-5):913–930, 1978.

[41] B Miller, C OHern, and RP Behringer. Stress fluctuations for continuously sheared granular materials. *Phys. Rev. Lett*, 77(15):3110–3113, OCT 7 1996.

[42] S. Abe and K. Mair. Effects of gouge fragment shape on fault friction: New 3D modelling results. *Geophys. Res. Lett.*, 36, DEC 1 2009.

[43] S Ostojic, E Somfai, and B Nienhuis. Scale invariance and universality of force networks in static granular matter. *Nature*, 439(7078):828–830, FEB 16 2006.

[44] P. Dantu. Recently formed methane-derived carbonates from the North Sea floor. *Proc. of the Fourth International Conf. on Soli Mechanics and Foundation Eng.*, 1:144, 1957. London: Butterworths Scientific.

[45] G. Løvoll, K. J. Måløy, and E. G. Flekkøy. Force measurements on static granular materials. *Phys. Rev.E*, 60(5, Part B):5872–5878, NOV 1999.

[46] J. W. Landry, G. S. Grest, L. E. Silbert, and S. J. Plimpton. Confined granular packings: Structure, stress, and forces. *Phys. Rev.E*, 67(4, Part 1), APR 2003.

[47] C. T. Veje and P. Dimon. Two-dimensional granular flow in a small-angle funnel. *Phys. Rev.E*, 54(4):4329–4337, Oct 1996.

[48] W. Losert, L. Bocquet, T.C. Lubensky, and J.P. Gollub. Particle dynamics in sheared granular matter. *Phys. Rev. Lett*, 85(7):1428–1431, AUG 14 2000.

[49] T. Le Pennec, K. Måløy, A. Hansen, M. Ammi, D. Bideau, and X. Wu. Ticking hour glasses: Experimental analysis of intermittent flow. *Phys. Rev.E*, 53(3):2257–2264, Mar 1996.

[50] H. M. Jaeger, S. R. Nagel, and R. P. Behringer. Granular solids, liquids, and gases. *Revs. of Mod. Phys.*, 68(4):1259–1273, OCT 1996.

[51] P. G. de Gennes. Granular matter: a tentative view. *Revs. of Mod. Phys.*, 71(2, Sp. Iss. SI):S374–S382, MAR 1999.

[52] M. S. Paterson and T.-F. Wong. *Experimental rock deformation: The brittle field*. Springer, Berlin, 2006.

[53] A. Y. Rozhko, Y. Y. Podladchikov, and F. Renard. Failure patterns caused by localized rise in pore-fluid overpressure and effective strength of rocks. *Geophys. Res. Lett.*, 34, 2007.

[54] D. J.Hornbaker, R. Albert, I. Albert, A. L. Barabasi, and P. Schiffer. What keeps sandcastles standing? *Nature*, 387(6635):765, JUN 19 1997.

[55] E. Lemaire, P. Levitz, G. Daccord, and H. Vandamme. From Viscous Fingering to Viscoelastic Fracturing in Colloidal Fluids. *Phys. Rev. Lett*, 67(15):2009–2012, OCT 7 1991.

[56] T. Hirata. Fracturing due to fluid intrusion into viscoelastic materials. *Phys. Rev.E*, 57(2, Part A):1772–1779, FEB 1998.

[57] R. O. Davis and A. P. S. Selvadurai *Plasticity and Geomechanics*. Cambridge University Press, 2002. ISBN 0 521 81830 3 hardback.

[58] P. R. Cobbold and L. Castro. Fluid pressure and effective stress in sandbox models. *Tectonophys.*, 301(1-2):1–19, JAN 15 1999.

[59] R. Mourgues and P. R. Cobbold. Some tectonic consequences of fluid overpressures and seepage forces as demonstrated by sandbox modelling. *Tectonophys.*, 376(1-2):75–97, NOV 20 2003.

[60] R. H. Sibson. Brittle-failure controls on maximum sustainable overpressure in different tectonic regimes. *AAPG Bulletin*, 87:901–908, 2003.

[61] D. Kunii and O. Levenspiel. *Fluidization Engineering*. Wiley and Sons, New York, 1969.

[62] D. Gidaspow. *Multiphase flow and fluidization: Continuum and Kinetic Theory Descriptions*. Academic Press, Inc., 1994.

[63] M. P. Dudukovic, F. Larachi, and P. L. Mills. Multiphase reactors - revisited. *Chem. Eng. Science*, 54:1979–1995, 1999.

[64] T. Wilhelm. *Piping in Saturated Granular Media*. PhD thesis, Leopold-Franzens-Universitet Innsbruck, 2000.

[65] P. Rigord, A. Guarino, V. Vidal, and J. C. Geminard. Localized instability of a granular layer submitted to an ascending liquid flow. *Gran. Matt.*, 7(4):191–197, NOV 2005.

[66] M.-O. Coppens. Method for operating a chemical and/or physical process by means of a hierarchical fluid injection system, 2000. Pub. No: W0/2000/066257.

[67] P. Tang and V. M. Puri. Methods for minimizing segregation: A review. *Particulate Sci. and Tech.*, 22(4):321–337, OCT-DEC 2004.

[68] K. M. Hill, J. F. Gilchrist, J. M. Ottino, D. V. Khakhar, and J. J. McCarthy. Mixing of granular materials: A test-bed dynamical system for pattern formation. *Int. J. of Bifurc. and Chaos*, 9(8):1467–1484, AUG 1999.

[69] K. M. Hill, D. V. Khakhar, J. F. Gilchrist, J. J. McCarthy, and J. M. Ottino. Segregation-driven organization in chaotic granular flows. *Proceedings of the National Academy of Sciences of the United States of America*, 96(21):11701–11706, OCT 12 1999.

[70] N. Lecocq and N. Vandewalle. Stripes ordering in self-stratification experiments of binary and ternary granular mixtures. *Phys. Rev.E*, 62(6, Part B):8241–8244, DEC 2000.

[71] J.M. Ottino and D. V. Khakhar. Mixing and Segregation of Granular Materials. *Annual Rev. of Fluid Mech.*, 32:55–91, 2000.

[72] M. A. Gilbertson and I. Eames. Segregation patterns in gas-fluidized systems. *J. of Fluid Mech.*, 433:347–356, APR 25 2001.

[73] J. M. Valverde, A. Castellanos, P. Mills, and M. A. S. Quintanilla. Effect of particle size and interparticle force on the fluidization behavior of gas-fluidized beds. *Phys. Rev.E*, 67(5, Part 1), MAY 2003.

[74] R. V. Daleffe, M. C. Ferreira, and J. T. Freire. Effects of binary particle size distribution on the fluid dynamic behavior of fluidized, vibrated and vibrofluidized beds. *Brazilian J. of Chem. Eng.*, 25(1):83–94, JAN-MAR 2008.

[75] A. B. Ezersky and F. Marin. Segregation of sedimenting grains of different densities in an oscillating velocity field of strongly nonlinear surface waves. *Phys. Rev. E*, 78(2):022301, Aug 2008.

[76] M. L. de Souza-Santos. Comprehensive modelling and simulation of fluidized bed boilers and gasifiers. *Fuel*, 68(12):1507 – 1521, 1989.

[77] R. Jullien, P. Meakin, and A. Pavlovitch. Particle Size Segregation by Shaking in Two-Dimensional Disc Packings. *Europhys. Lett.*, 22(7):523–528, 1. June 1993.

[78] M. Mourad, M. Hemati, and C. Laguerie. Hydrodynamics of a Fluidized-Bed Flotation Dryer - Determination of the Characteristic Fluidization Rates of Corn and Sand Mixtures. *Powder Tech.*, 80(1):45–54, JUL 1994.

[79] L.H. Shen, M.Y. Zhang, and Y.Q. Xu. Model for Solids Mixing in a 2-Dimensional Gas-Fluidized Bed. *Chem. Eng. Sci.*, 50(11):1841–1844, JUN 1995.

[80] S. Y. Wu and J. Baeyens. Segregation by size difference in gas fluidized beds. *Powder Tech.*, 98(2):139–150, AUG 1 1998.

[81] D. Gauthier, S. Zerguerras, and G. Flamant. Influence of the particle size distribution of powders on the velocities of minimum and complete fluidization. *Chem. Eng. J*, 74(3):181–196, JUL 19 1999.

[82] A. Marzocchella, P. Salatino, V. Di Pastena, and L. Lirer. Transient Fluidization and Segregation of Binary Mixtures of Particles. *AIChE J.*, 46(11):2175–2182, NOV 2000.

[83] N. Thomas. Reverse and intermediate segregation of large beads in dry granular media. *Phys. Rev.E*, 62(1, Part B):961–974, JUL 2000.

[84] B. G. M van Wachem, J. C. Schouten, C. M. van den Bleek, R. Krishna, and J. L. Sinclair. Cfd modeling of gas-fluidized beds with a bimodal particle mixture. *AIChE J*, 47(6):1292–1303, 2001.

[85] B. Formisani, G. De Cristofaro, and R. Girimonte. A fundamental approach to the phenomenology of fluidization of size segregating binary mixtures of solids. *Chem. Eng. Science*, 56(1):109–119, JAN 2001.

[86] M. J. Rhodes, X. S. Wang, M. Nguyen, P. Stewart, and K. Liffman. Study of mixing in gas-fluidized beds using a DEM model. *Chem. Eng. Science*, 56(8):2859–2866, APR 2001.

[87] H. L. Lu, Y. R. He, G. Dimitri, L. D. Yang, and Y. K. Qin. Size segregation of binary mixture of solids in bubbling fluidized beds. *Powder Tech.*, 134(1-2):86–97, AUG 5 2003.

[88] G. Felix and N. Thomas. Evidence of two effects in the size segregation process in dry granular media. *Phys. Rev.E*, 70(5, Part 1), NOV 2004.

[89] Y. Q. Feng, B. H. Xu, S. J. Zhang, A. B. Yu, and P. Zulli. Discrete particle simulation of gas fluidization of particle mixtures. *AIChE J.*, 50(8):1713–1728, AUG 2004.

[90] H. Umekawa, S. Furui, Y. Oshima, M. Okura, M. Ozawa, and N. Takenaka. Quantitative measurement of segregation phenomena in a binary-mixture fluidized bed by neutron radiography. *Nuclear Instruments & Methonds in Physics Research Section A-Accelerations, Spectrometers, Detectors and Associated Equipment*, 542(1-3):219–225, APR 21 2005. 5th International Topical Meeting on Neutron Radiography, Munich, GERMANY, JUL 26-30, 2004.

[91] O. Roche, M. A. Gilbertson, J. C. Phillips, and R. S. J. Sparks. The influence of particle size on the flow of initially fluidised powders. *Powder Tech.*, 166(3):167–174, AUG 28 2006.

[92] J. Leboreiro, G. G. Joseph, C. M. Hrenya, D. M. Snider, S. S. Banejee, and J. E. Galvin. The influence of binary drag laws on simulations of species segregation in gas-fluidized beds. *Powder Tech.*, 184(3):275–290, JUN 2 2008.

[93] K. G. Palappan and P. S. T. Sai. Studies on segregation of binary mixture of solids in continuous fast fluidized bed - Part II. Effect of particle size. *Chem. Eng. J.*, 139(2):330–338, JUN 1 2008.

[94] S. Ergun. Fluid flow through packed columns. *Chem. Eng. Prog.*, 48(2):89–94, 1952.

[95] S. McNamara, E. G. Flekkøy, and K. J. Måløy. Grains and gas flow: Molecular dynamics with hydrodynamic interactions. *Phys. Rev. E*, 61(4, Part B):4054–4059, APR 2000.

[96] J. L. Vinningland, Ø. Johnsen, E. G. Flekkoy, R. Toussaint, and K. J. Måløy. Granular rayleigh-taylor instability: Experiments and simulations. *Phys. Rev. Lett*, 99(4), JUL 27 2007.

[97] M. Hovland, M. Talbot, S. Olaussen, and L. Aasberg. Recently formed methane-derived carbonates from the North Sea floor. *In: Thomas, B.M. (Ed.), Petroleum Geochemsitry in Exploration of the Norwegian Shelf. Norwegian Petrol. Soc. Graham & Trottman*, pp. 263–266, 1985.

[98] S. Planke, H. Svensen, M. Hovland, D. A. Banks, and B. Jamtveit. Mud and fluid migration in active mud volcanoes in Azerbaijan. *Geo-Mar. Lett.*, 23(3-4):258–268, DEC 2003. 7th International Conference on Gas in Marine Sediments/NATO Advanced Research Workshop on Seafloor Hydrocarbon Seeps, BAKU, AZERBAIJAN, OCT 07-11, 2002.

[99] B. Jamtveit, H. Svensen, Y. Y. Podladchikov, and S. Planke. Hydrothermal vent complexes associated with sill intrusions in sedimentary basins. In Breitkreuz, C and Petford, N, editor, *Physical Geology of High-Level Magmatic Systems*, no. 234 in Geological Society Special Publication,

pages 233–241,2004. International Workshop on the Physical Geology of Subvolcanic Systems, Freiberg, GERMANY, OCT 12-14, 2002.

[100] H. Svensen, B. Jamtveit, S. Planke, and L. Chevallier. Structure and evolution of hydrothermal vent complexes in the Karoo basin, South Africa. *J. Geol. Soc. London*, 163:671–682, 2006.

[101] R. S. J. Sparks, L. Baker, R. J. Brown, M. Field, J. Schumacher, G. Stripp, and A. Walters. Dynamical constraints on kimberlite volcanism. *J. Volc. and Geotherm. Res.*, 155(1-2):18–48, JUL 1 2006. Symposium on Explosive Mafic Volcanism held at the IAVCEI 2004 General Assembly, Pucon, CHILE, 2004.

[102] A. L. Walters, J. C. Phillips, R. J. Brown, M. Field, T. Gernon, G. Stripp, and R. S. J. Sparks. The role of fluidisation in the formation of volcaniclastic kimberlite: Grain size observations and experimental investigation. *J. Volc. and Geotherm. Res.*, 155(1-2):119–137, JUL 1 2006. Symposium on Explosive Mafic Volcanism held at the IAVCEI 2004 General Assembly, Pucon, CHILE, 2004.

[103] A. A. Jakubov, A. A. Ali-Zade, and M. M. Zeinalov. Mud volcanoes of the Azerbaijan SSR, Atlas (in Russian). *Azerbaijan Academy of Sciences, Baku*, 1971.

[104] L. I. Dimitrov. Mud volcanoes - the most important pathway for degassing deeply buried sediments. *Earth-Sci. Rev.*, 59:49–76, 2002.

[105] H. Svensen, D. A. Karlsen, A. Struz, K. Backer-Owe, D. A. Banks, and S. Planke. Processes controlling water and hydrocarbon composition in seeps from the Salton Sea geothermal system, California, USA. *Geology*, 35:85–88, 2007.

[106] A. Mazzini, H. Svensen, G. G. Akhmanov, G. Aloisi, S. Planke, A. Malthe-Sørenssen, and B. Istadi. Triggering and dynamic evolution of the LUSI mud volcano, Indonesia. *Earth and Planet. Sci. Lett.*, 261(3-4):375–388, SEP 30 2007.

[107] AJ Kopf. Significance of mud volcanism. *Revs. of Geophys.*, 40(2), SEP 2002.

[108] M. Tingay, O. Heidbach, R. Davies, and R. Swarbrick. Triggering of the Lusi mud eruption: Earthquake versus drilling initiation. *Geology*, 36(8):639–642, AUG 2008.

[109] Richard J. Davies, Maria Brumm, Michael Manga, Rudi Rubiandini, Richard Swarbrick, and Mark Tingay. The east java mud volcano (2006 to present): An earthquake or drilling trigger? *Earth and Planet. Sci. Lett.*, 272(3-4):627 – 638, 2008.

[110] H. Svensen, S. Planke, A. Malthe-Sørenssen, B. Jamtveit, R. Myklebust, T. R. Eidem, and S. S. Rey. Release of methane from a volcanic basin as a mechanism for initial Eocene global warming. *Nature*, 429(6991):542–545, JUN 3 2004.

[111] S. Planke, T. Rasmussen, S. S. Rey, and R. Myklebust. Seismic characteristics and distribution of volcanic intrusions and hydrothermal vent complexes in the Vøring and Møre basins. *Geol. Soc. London*, 2005.

[112] I. Aarnes, H. Svensen, S. Polteau, J. A. D. Connolly, and Y. Y. Podladchikov. The impact of large scale contact metamorphism on global climate. *Geochemica et Cosmochimica Acta*, 73(13, Suppl. S):A1, JUN 2009. 19th Annual VM Goldschmidt Conference, Davos, SWITZERLAND, JUN 21, 2009.

[113] I. Aarnes, H. Svensen, J. A. D. Connolly, and Y. Y. Podladchikov. How contact metamorphism can trigger global climate changes: Modeling gas generation around igneous sills in sedimentary basins. *Geochemica et Cosmochimica Acta*, 2010. Accepted.

[114] T. S. Woolsey, M. E. Macallum, and S. A. Schumm. Modelling of diatreme emplacement by fluidization. *Phys. Chem. of the Earth*, 9:29–45, 1975.

[115] C. R. Clement. The emplacement of some diatreme facies kimberlites. *Phys. Chem. of the Earth*, 9:51–59, 1975.

[116] V. Lorenz. Formation of phreatomagmatic maar-diatreme volcanoes and its relevance to kimberlite diatremes. *Phys. Chem. of the Earth*, pp. 17–29, 1975.

[117] V. Lorenz and S. Kurzlaukis. Root zone processes in the phreatomagmatic pipe emplacement model and consequences for the evolution of maar-diatreme volcanoes. *J. of Volc. and Geotherm. Res.*, 159:4–32, 2007.

[118] T. H. Torsvik, K. Burke, B. Steinberger, S. J. Webb, and L. D. Ashwal. Diamonds smapled by plumes from the core-mantle boundary. *Nature. accepted.*

[119] T. M. Gernon, R. S. J. Sparks, and M. Field. Degassing structures in volcaniclastic kimberlite: Examples from southern African kimberlite pipes. *J. of Volc. and Geotherm. Res.*, 174(1-3):186–194, JUN 20 2008. Workshop on Kimberlite Emplacement, Saskatchewan, CANADA, SEP 07-14, 2006.

[120] Ø . Hammer and K. E. Webb. Piston coring of Inner Oslofjord pockmarks, Norway: constraints on age and mechanism. *Norwegian J. of Geol.*, 1:79, 2010.

[121] P.K. Harrington. Formation of pockmarks by pore-water escape. *Geo-Mar. Lett.*, 5(3):193–197, 1985.

[122] J. B. Jensen, A. Kuijpers, O. Bennike, T. Laier, and F. Werner. New geological aspects for freshwater seepage and formation in Eckerførde Bay, western Baltic. *Cont. Shelf. Res.*, 22:2159–2173, 2002.

[123] V. Karpen, L. Thomsn, and E. Suess. Groundwater discharges in the Baltic Sea: survey and quantification using a schlieren technique application. *Geofluids*, 6:241–250, 2006.

[124] M. Hovland, H. Svensen, C. F. Forsberg, H. Johansen, C. Fichler, J. H. Fossaa, R. Jonsson, and H. Rueslaatten. Complex pockmarks with carbonate-ridges off mid-Norway: Products of sediment degassing. *Mar. Geol.*, 218:191–206, 2005.

[125] Ø. Hammer, K. E. Webb, and D. Depreiter. Numerical simulation of upwelling currents in pockmarks, and data from the Inner Oslofjord, Norway. *Geo-Mar. Lett.*, 29(4):269–275, AUG 2009.

[126] K. E. Webb, D. L. A. Barnes, and S. Planke Pockmars: Refuges for marine benthic biodiversity? *Limnol. and Oceanography*, 54(5):1776–1788, 2009.

[127] J. L. Moss and J. Cartwright. The spatial and temporal distribution of pipe formation, offshore namibia. *Mar. Pet. Geol.*, 27(6):1216 – 1234, 2010.

[128] S. F. Cox. Coupling between deformation, fluid pressures, and fluid flow in ore-producing hydrothermal systems at depth in the crust, pages 39–75. *Soc. of Econ. Geol.*, Littleton, Colorado, 2005.

[129] K. Terzaghi. *Theoretical soil mechanics*. John Wiley and Sons, New York, 1943.

[130] J. A. D. Connolly and Y. Y. Podladchikov. Compaction-driven fluid flow in viscoelastic rock. *Geodin. Acta*, 11(2-3):55–84, MAR-AUG 1998.

[131] http://www.thejakartaglobe.com/news/latest-mudflow-bubble-on-sidoarjo-roadway-raises-fears-of-explosion/370173.

Part II

Papers

Chapter 4

The Papers

Summary of Paper I

Experiments were conducted to investigate the behavior of partially gas-fluidized granular mixtures formed by injecting air upwards through a mixture of dry glass beads with two different sizes confined in a vertical Hele-Shaw cell. Partially fluidization, accompanied by size segregation, occurs when the air infiltration velocity is too small to fluidize all of the granular medium, but too large for all of the particles to remain stationary. The main focus was the formation of vertical bands like those reported by Gilbertson and Eames 2001 [72] as opposed to segregation into more-or-less horizontal layers. The gas injection velocity and the volume fraction of small particles in the binary mixture was systematically varied. Three different patterns, two of them leading to the formation of vertical structures and the third leading to vertical segregation into two horizontal layers, were investigated. The variety of patterns and their complex dynamics is a consequence of the interplay between fluidization, sedimentation, and inhomogeneities in the permeability field, occurring when solid-like and liquid-like phases coexist. The coupling between heterogeneities in the material properties, fluid flow, and fluid induced deformation may be relevant to a variety of geological processes.

My contribution to this work was the project leadership, I had the initial idea, in addition to designing, building and performing the experiments. I performed the quantitative analysis and contributed to the writing process.

Summary of Paper II

Piercement structures such as mud volcanoes, hydrothermal vent complexes, pockmarks and kimberlite pipes, forming during the release of pressurized fluids, are observed in a range of geological settings. The goal of this work was to predict under which conditions piercement structures form by using sand box experiments injecting compressed air through an inlet with width w at the base of a bed of glass beads of height h. At a critical velocity v_f, a fluidized zone consisting of a diverging cone-like structure formed with morphological similarities to those observed in nature. Dimensional analysis showed that v_f is correlated with h/w. We derived an analytical model to estimate the critical velocity v_f.

The model consists of a force balance between the weight of the fluidized zone and the seepage forces. The analytic model reproduces the observed correlation between v_f and h/w, but it slightly under-estimates the fluidization velocity. Our results suggest that seepage forces are the main triggering force for fluidization and that the commonly used proxy that the fluid pressure must equal or exceed the lithostatic weight, needs to be re-considered. Combining experiments and model we derived an expression for the critical pressure such that estimates of the critical pressure in a variety of geological environments could be made. The comparison between the estimated and the measured pressure prior to the initiation of the Lusi mud volcano (Indonesia) indicates that the presented model over-estimates the critical pressures.

My contribution to the project was the project leadership, I had the initial idea, in addition to designing, building and performing the experiments. I contributed to solving the analytic model and to the discussion, application and writing of the article.

Summary of Paper III

Piercement structures such as hydrothermal vent complexes, pockmarks, and mud volcanoes are found in a various geological settings but are often associated with faults or other fluid-focussing features. This article aims to investigate and understand the mechanism responsible for the formation of piercement structures in sedimentary basins and the role of strike-slip faulting as a triggering mechanism for fluidization. For this purpose four different approaches were combined: fieldwork, analogue experiments, and mathematical modeling for brittle and ductile rheologies. The result of this study may be applied to several geological settings, including the newly formed Lusi mud volcano in Indonesia.

Lusi became active the 29th of May 2006 on Java Island. Debates on the trigger of the eruption rose immediately. Was Lusi triggered by the reactivation of a fault after a 6.8 earthquake that occurred two days earlier? Or did a neighbouring exploration borehole induce a massive blow-out? Field observations reveal that the Watukosek fault crossing the Lusi mud volcano was reactivated after the 27th of May earthquake. Ongoing monitoring shows that the frequent seismicity periodically reactivates this fault with synchronous peaks of flow rates from the crater. Our integrated study demonstrates that the critical fluid pressure required to induce sediment deformation and fluidization is dramatically reduced when strike-slip faulting is active. The proposed shear-induced fluidization mechanism explains why piercement structures such as mud volcanoes are often located along fault zones.

Our results support a scenario where the strike-slip movement of the Watukosek fault triggered the Lusi eruption and synchronous seep activity witnessed at other mud volcanoes along the same fault. The possibility that the drilling contributed to trigger the eruption cannot be excluded. However, so far, no univocal data support the drilling hypothesis, and a blow-out scenario can neither explain the dramatic change that affected the plumbing system of numerous seep systems on Java after the 27th of May earthquake. To date (i.e. May 2010) Lusi is still active (April, 2010 [131]).

My contribution to this work was designing, building and performing the experiments. I performed the analytic work and contributed to the writing

process and the discussion on how to apply the experiments, the analytic and numerical analysis to the interpretation and understanding of the geological phenomena. I joined in on one of the field work missions to the Lusi mud volcano (Java, Indonesia).

Summary of Paper IV

Targeted sampling on the Dolgovskoy Mound (northern Shatsky Ridge) revealed the presence of spectacular laterally extensive and differently shaped authigenic carbonates. The sampling stations were selected based on sidescans sonar and profiler images that show patchy backscatter and irregular and discontinuous reflections in the near subsurface. The interpretation of acoustic data from the top part of the mound supports the seafloor observations and the sampling that revealed the presence of a complex subsurface plumbing system characterized by carbonates and gas. The crusts sampled consist of carbonate cemented layered hemipelagic sediments (Unit 1) associated with several centimetres thick microbial maths. Three different carbonate morphologies were observed: a) tabular slabs, b) subsurface cavernous carbonates consisting of void chambers up to 20 cm^3 in size and c) chimney and tubular conduits vertically oriented or forming a subhorizontal network in the subsurface. The methanogenic origin of the carbonates is established based on visual observations of fluids seepage structures, ^{13}C depletion of the carbonates (varying between -3.67% and -2.74%), and by thin carbonate layers present within the thick microbial mats. Laboratory experiments with a Hele-Shaw cell were conducted in order to simulate the gas seepage through contrasting grain size media present on the seafloor. Combined petrography, visual observations and sandbox simulations allowed a characterization of the dynamics and the structures of the plumbing system in the near subsurface. Based on sample observations and the experiments, three observed morphologies of authigenic carbonates are interpreted: a) Darcian porous flow through the finely laminated clayey/coccolith-rich layers, b) gas accumulation chambers at sites where significant fluid escape was impeded by thicker clayey layers forming the laminated Unit 1 and c) focussed vertical fluid venting and subhorizontal migration of overpressured fluids released from b). The Hele-Shaw cell experiments represent a promising tool for investigating the mechanics of shallow fluid flow pathways in marine systems.

My contribution to this project was through designing, building and performing of the experiments. I performed the dimensional analysis and joined in on the discussion of how to employ the concepts from the laboratory to the geological environments. In retrospect, concerning the formation of the gas-pockets between layers of contrasting permeabilities it seem questionable if the onset is controlled by the scaling relation given in the paper only. The formation of the cavernous features is an interesting physical problem in its own right. In addition to the cohesional effects within a layer, further studies could focus on the contrasting properties of the layered system including effects of permeability, density, elasticity and plasticity properties of the deforming sediments.

Paper I

Morphological Transitions in Partially Gas-Fluidized Granular Mixtures
Anders Nermoen, Christophe Raufaste, Simon D. deVilliers, Espen Jettestuen, Paul Meakin and Dag K. Dysthe
Physical Review E, **81**, 061305

Morphological transitions in partially gas-fluidized granular mixtures

Anders Nermoen,[1,*] Christophe Raufaste,[1,2] Simon Daniel deVilliers,[1] Espen Jettestuen,[1,3] Paul Meakin,[1,4,5] and Dag Kristian Dysthe[1]

[1]*Physics of Geological Processes, University of Oslo, Box 1048 Blindern, N-0316 Oslo, Norway*

[2]*Laboratoire de Physique de la Matière Condensée, UMR 6622, CNRS and Université de Nice–Sophia Antipolis, Parc Valrose, 06108 Nice Cedex 2, France*

[3]*International Research Institute of Stavanger, Prof. Olav Hessensvei 15, Stavanger, Norway*

[4]*Center for Advanced Modeling and Simulation, Idaho National Laboratory, Idaho Falls, Idaho 83415, USA*

[5]*Multiphase Flow Assurance Innovation Center, Institute for Energy Technology, Kjeller, Norway*

(Received 21 December 2009; revised manuscript received 10 May 2010; published 29 June 2010)

Experiments were conducted to investigate pattern formation during the defluidization of a partially fluidized bimodal granular mixture. Partial fluidization occurs when the system is driven at gas velocities that are insufficient to fluidize all of the constituent particles. Over time, the granular mixture evolves into a variety of patterns depending on the concentrations of large and small particles and the gas velocity. We show how vertically oriented pipes, containing large particles, grow at the interface between the fluidized and static zones. The heterogeneities in the permeability field focus the flow, causing localized fluidization, which in turn localizes the sedimentation of the large particles segregating the system. We discuss how the interplay between heterogeneities in material properties, fluid flow and fluid induced deformation may be relevant to a variety of geological processes.

DOI: 10.1103/PhysRevE.81.061305 PACS number(s): 45.70.Mg, 83.80.Fg, 47.55.Lm, 91.40.Ge

I. INTRODUCTION

Interest in the physics of granular materials has increased in recent decades because of their practical importance and nonintuitive physical behavior [1–4]. Depending on the nature of the particles, the particle-particle interactions, the properties of the interstitial fluids, and the energy imparted to the particles by flowing fluids or accelerating boundaries (shaking, vibrating etc.), they behave like solids, fluids, and exhibit behaviors unique to granular materials [5,6]. At rest, granular materials exhibit solidlike properties with well-defined cohesive and frictional strengths, and with a stress distribution that is concentrated onto a network of highly stressed particles.

Flowing granular materials display several nonintuitive phenomena such as intermittent flow [7,8] and convection patterns [9]. A major class of these phenomena is associated with the segregation of particles with differing physical properties such as density, angularity, size, and restitution coefficients. Segregation is observed in vibrated, avalanching, sedimenting and partially fluidized systems [1,10–16]. Size segregation, in particular, is common in nature and well-known examples include the "Brazil nut effect" [17], i.e., the upward migration of the larger particles occurring in shaken or vibrated granular beds [18,19], size segregation in avalanches in which the grain mobility increases with decreasing particle size [20] and the spontaneous formation of stratification layers of coarse and fine grains when mixtures flow down slopes [21]. Other examples of segregation phenomena include the patterns that form in ground subjected to freeze-thaw cycles [22] and the layering that occurs naturally in fluvial systems, desert dunes and beaches [23–25]. The natural segregation processes listed above have a large impact on sedimentary stratigraphy, which is important to the oil and gas industry [26].

In this paper, we focus on segregation processes occurring in a gas-fluidized system. Fluidization has been extensively studied because of its practical importance in industrial applications such as pharmaceuticals, chemical processing, oil and gas refining, drying, solid fuel gasification and combustion, and because of its intrinsic scientific importance in a number of disciplines including geology, physics, and materials science [27–44]. Gas fluidized beds have been used in applications in which both mixing and segregation is the goal. Good mixing of particles with different properties is desired in applications such as coal combustion, food, and pharmaceutical processing where segregation may reduce the quality and performance of the end product [4,45]. On the other hand, segregation by fluidization is needed to separate one solid phase from another in a variety of industrial, agricultural, mining, and waste management applications.

In nature, a variety of mechanisms generate interstitial fluid flow within the Earth. There are typically two fluid induced deformation mechanisms leading to an increase in the bulk permeability [46,47]: hydraulic fracturing leading to the growth of tensile cracks; and fluidization, which mobilizes all or parts of the granular material. Partial fluidization could play an important role in the formation of subconical pipelike piercement structures observed in geological systems. Examples include: a) hydrothermal vent complexes (HTVC) formed by magmatic intrusions into sedimentary basins leading to the rapid decomposition of liquid and solid organic substances, producing large amounts of gas, and rapid boiling of water, creating large quantities of steam and supercritical water [48,49]; b) vents formed by the expulsion of fluids in unconsolidated sea bed sediments, which can be observed as pockmarks on the sea floor. The fluid pressure may be formed, for example, by pore collapse in water bearing quick clay [50,51]; c) kimberlite volcanos formed due to the exsolution of fluids from ascending volatile-rich kimber-

*anderne@fys.uio.no

lite magma, as the pressure is reduced, resulting in deep rooted (down to ~200 km) explosions [52–58]; and d) mud volcanos most commonly formed in rapidly deposited, organic rich and water bearing sediments with a low geothermal gradient [59–61]. The physics of flow localization coupled with material deformation and segregation may be of relevance to several earth systems.

When the local fluid pressure gradient exceeds a critical threshold fluidization of the matrix occurs. Flow localization is expected in naturally occurring sediments due to variations in the permeability field caused by e.g., spatial variations in the distribution of grain sizes. Both static and fluidized regions may co-exist due to flow localization near the critical fluidization threshold. The co-existence of fluidized and static regions is referred to as a partially fluidized phase, which we observe for a range of imposed flow rates in the experiments described herein. Grains with varying sizes respond differently within the fluidized zones. For example, the smaller grains may remain fluidized while the larger particles sediment down leading to the development of a range of segregation patterns. The settling of the large grains into vertical pipes was first documented by Gilberton and Eames 2001 [1]. An extensive literature is available on segregation by size, shape and density in gas-fluidized systems, however a complete description of the segregation patterns formed between the flow rates resulting in incipient motion and full fluidization is not documented [29–40]. In this article we show that the localization of gas flow due to perturbations in the permeability field is coupled with localization of the fluidization, resulting in diverse segregation patterns.

We describe experiments performed on partially fluidized granular media consisting of particles of two sizes confined in a vertical Hele-Shaw cell (two parallel vertical glass sheets separated by a small gap and sealed along their vertical edges, which enclose the granular material). We present a quantitative characterization of the patterns formed and their dynamic evolution.

II. PHYSICAL PROCESSES WITHIN FLUIDIZED SYSTEMS

Mean field concepts on a macroscopic scale provide an approximate understanding of the behavior of fluidized systems. Relevant properties include the permeability k, the porosity ϕ, the gas filtration velocity v_f, and the bed density $\rho_b = \phi\rho_f + (1-\phi)\rho_s$, where ρ_f is the fluid density and ρ_s is the density of the solid particles.

The mechanical behavior of dry, noncohesive granular material depends upon the interaction between the constituent particles [26], the gas-particle interactions, and the effects of body forces such as Earth's gravitational field acting on the particles. Nonfluidized granular beds can often be described by Mohr-Coulomb frictional rheology,

$$\tau = \mu\sigma_n + C, \tag{1}$$

where τ is the material shear strength, σ_n is the normal load on an arbitrary shear plane, μ is the friction coefficient and C is the interpolated cohesion of the granular material. Figure 2(D) shows that dependence of the measured shear strength on the normal load is consistent with the linear relationship shown in Eq. (1) for several granular mixtures used in this work.

Cobbold and Castro [62] presented experiments showing how the shear strength is reduced by the gas pressure gradients that affect the stresses within a granular packing, a result which was later confirmed by, e.g. [63–65]. In the simplest case, when the normal load is generated by gravity acting on the particle masses, cohesion is negligible, and the fluid pressure gradient is vertical (parallel to σ_n), the shear strength at depth z is given by,

$$\tau(z) = \mu(z)\int_0^z \left[\rho_b(z')g + \frac{\partial P}{\partial z'}\right]dz', \tag{2}$$

where g is the gravitational acceleration. Under these conditions, the fluid pressure gradient ∇P simplifies to $\partial P/\partial z$, and Darcy's law for low-Reynolds number fluid flow through the granular medium can be replaced by

$$v_f = -\frac{k(x,y)}{\eta}\frac{\partial P}{\partial z}, \tag{3}$$

where η is the viscosity of the gas, v_f is the gas filtration velocity and $k(x,y)$ is the permeability field within the porous packing. For a homogeneous medium with no gradients in the material properties, $\mu(z)$ can be replaced by μ, $\rho_b(z)$ can be replaced by ρ_b and $k(x,y)$ can be replaced by k, and Eq. (2) simplifies to,

$$\tau = \mu z\left(\rho_b g - v_f\frac{\eta}{k}\right). \tag{4}$$

Fluidization is said to occur when the granular material changes from a static, solidlike behavior, to a liquidlike state in which the material cannot sustain shear stresses. In this case $\tau \approx 0$ and the critical velocity for fluidization (the velocity at which the weight of the bed is counteracted by the force exerted on the bed by the flowing gas) is given by

$$v_c = \frac{k}{\eta}\rho_b g. \tag{5}$$

The permeability of granular porous media is often estimated from the Carman-Kozeny equation,

$$k_{ck} = \frac{d^2}{4K}\frac{\phi^3}{(1-\phi)^2}, \tag{6}$$

and thus the critical fluidization velocity is given by,

$$v_c = \frac{d^2}{4K}\frac{\phi^3}{(1-\phi)^2}\frac{\rho_b g}{\eta}, \tag{7}$$

where K is an empirical constant. The critical velocity in Eq. (7) depends on d^2, because the permeabilities of geometrically similar porous media scale as d^2. Within the fluidized phase, segregation can occur because, under low-Reynolds number flow conditions, the viscous drag force acting on a particle scales as d and the gravitational force scales as d^3. Consequently a situation may arise in which larger particles sediment down while smaller particles remain fluidized.

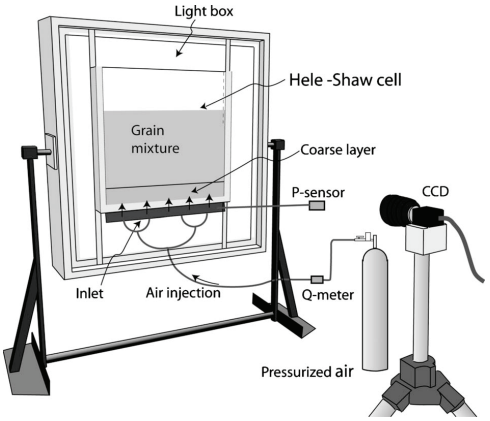

FIG. 1. Vertically oriented Hele-Shaw cell containing the grain mixtures with back lighting. The control parameters are the filtration velocity v_f and the weight concentration of small particles c. A LABVIEW program ensured quasicontinuous acquisition of CCD images, v_f and the inlet pressure P.

III. EXPERIMENTAL SETUP AND MATERIAL PARAMETERS

The experiments were performed by injecting dry air into the base of a vertically oriented Hele-Shaw cell (HS-cell) (Fig. 1) filled with a mixture of glass beads with a close to bi-modal size distribution [see Fig. 2(A)]. The mixture was characterized by the mass fraction of small beads c. We used Beijer (Beijer AS, Drammen, Norway) glass beads of type "AD" with diameters of $d_1=140\pm20$ μm and type 'C' with $d_2=320\pm35$ μm [see Fig. 2(A) for the particle size distribution (*PSD*)].

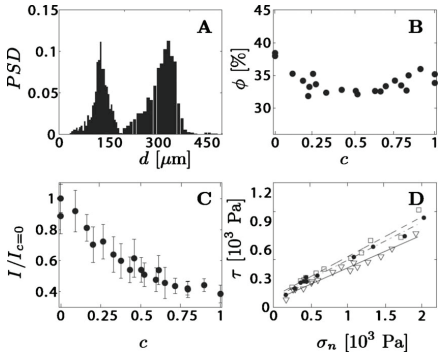

FIG. 2. Properties of the Beijer soda lime glass beads [66] with a specific density of 2.45 g/cm^3. A) Particle size distribution, *PSD*, for type AD and C grains. B) The porosity versus the weight fraction of small particles, c. C) Transmitted light intensity as a function of c scaled by the intensity with only large particles. D) The shear strength τ as a function of the normal load σ_n using a Hubbert-type apparatus [67] ($c=0$, 0.75, and 1 are represented by the dots, triangles and squares, respectively).

The HS-cell was constructed from two 1.2 cm thick glass plates with a width of 62.5 cm, a height of 55 cm and a gap spacing of 0.6 cm. The HS-cell was filled to a height of $h=35$ cm. The cell was illuminated from behind, and the transmitted light intensity decreased as the proportion of small particles increased [see Fig. 2(C)]. This effect was used to quantify the segregation dynamics and to characterize the static zones. Air was forced into the cell through an open pressure chamber constructed along the bottom of the cell, which was overlain by a metal mesh and a 9 cm deep porous layer made of lightly sintered large (type C) glass beads. The sintered layer provides a "flow diffusion" zone that creates a homogeneous flow boundary condition at the interface between this zone and the mobile particles. We found that the results did not change significantly if the depth of the flow diffusion zone was 9 cm or greater. The effect of this layer on the pressure measurement was calibrated so that the pressure difference across the grain mixture alone could be obtained, which was important to determine of the permeabilities of the granular media.

The inlet pressure P_{inlet} was measured using an Omega PX139–004 pressure sensor in the inlet and the flux Q was measured using an Omega FMA-1610 flux meter attached to the inlet tube. The experimental control parameters were the mass fraction of small beads, c, and the infiltration velocity $v_f=Q/(A\phi)$ where A is the cross sectional area of the HS-cell and ϕ is the pore volume fraction (porosity). Fluctuations in the pressure were less than ≈37 Pa ($\approx1\%$ of $\rho_b g h$), and the fluctuations in the mean filtration velocity v_f were ≤0.001 m/s. Since 95% of the pressure drop between the compressor and the atmosphere occurred across the reduction valve, variations in the gas influx were negligible throughout an experiment. The dynamics of fluidization and the development of the segregation pattern were captured as grayscale CCD images using a Jai CV-M4 camera at 20 frames per second.

Each experiment was performed according to the following procedure. The two grain types were mixed to the desired concentration, and the grain mixture was poured into the HS-cell from the top using a ~0.5 dl cup. This procedure produced horizontally striped patterns like that shown in Fig. 3(A). With this starting configuration, the valve was opened by hand to flush gas through the bed with a velocity v_f. To determine the morphology phase diagram (in Fig. 5) v_f was increased by steps of approximately 0.01–0.04 m/s to create the different partial or full fluidization regimes. For each step, the specific value of v_f was recorded and the resulting morphology was observed. Different morphologies were observed for different values of c and v_f [see Figs. 3(B)–3(D)]. The evolution of the granular system during the transient leading to a given morphology was investigated by refilling the cell with a given mixture and rapidly increasing v_f from zero to a value predetermined by the phase diagram. The patterns were characterized by analyzing the digital images and the dynamical measurements of the ratio $v_f/\Delta P$ [i.e., the permeability defined according to Eq. (8)].

Several experiments were performed to characterize the grains used in the experiments. The particle size distribution of the two grain types, obtained from analysis of microscope images, is shown in Fig. 2(A). The porosity as a function of

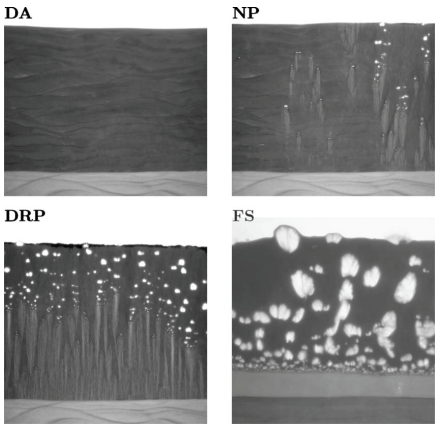

FIG. 3. Typical morphologies observed in the experiment. The lower 10% of each image shows the sintered, immobile grains, and the upper 90% of the images show the unconsolidated grain mixture (with $c=0.75$) at different values of v_f. Each image is 62 cm wide. Light gray zones correspond to areas with a higher fraction of large particles, while air bubbles are represented by the white regions. **DA**: No deformation is observed in the matrix at low velocities ($v_f < v_{f1}$). Darcian flow. **NP**: Vertical brighter structures (pipes) that nucleate within the bed ($v_f=0.07$ m/s). Air bubbles can be seen on top of the pipes. The pipes grow upward within the bed below the air bubbles. **DRP**: Vertical bright structures (pipes) rooted in the bottom of the bed correspond to static areas with larger quantities of large particles ($v_f=0.09$ m/s). Air bubbles nucleate at the upper tips of the pipes and move up to the top of the bed through the fluidized zone. The whole area above the pipes is fluidized. **FS**: The light gray stationary area above the sintered layer consists of large particles that have sedimented down out of the fluidized zone ($v_f=0.22$ m/s). The nonfluidized zone is characterized by its lack of vertical structure. The zone above is fully fluidized. Air bubbles nucleate at the bottom and travel up through the fluidized zone, depleted by large particles.

c is plotted in Fig. 2(B), where $\phi=1-M/\rho_s V$ is estimated from measurements of (V) the volume and (M) the corresponding mass. The light intensity transmitted through the HS-cell is plotted in Fig. 2(C) as a function of c, demonstrating how the brightness decreases as c increases.

Rheological experiments were performed with a Hubbert-type apparatus [67] to measure how the shear strength depends on the normal load. Each dot in Fig. 2(D) corresponds to a single failure experiment. Three sets of experiments were performed with $c=0$, 0.75, and 1. The linear increase in the shear strength τ with increasing normal stress σ_n enabled us to estimate the friction coefficient μ and the cohesion C (see Table I). The results show that the frictional coefficient for $c=0.75$ is lower than for the two end member cases $c=0$ and 1.

IV. RESULTS

A. Initial packing

The horizontally striped pattern observed in Fig. 3(A) is formed during the filling of the HS-cell. The observed segregation occurs due to documented processes [12,45] and results in an inhomogeneous permeability field. A two dimensional autocorrelation (AC) analysis was employed to characterize the pattern and determine the spatial correlation lengths. By fitting an ellipse to the zero level contour of the AC surface, a vertical correlation length (short axis) of ~1 cm was obtained. This value corresponds approximatively to the volume of the cup used to fill the cell with glass beads.

TABLE I. The glass beads exhibit a Mohr-Coulomb failure envelope where the shear strength varies in response to the normal load. The estimated frictional coefficient μ and cohesion C are given for three different small particle weight fractions.

c	μ	C (Pa)
0	0.39 ± 0.01	96 ± 15
0.75	0.34 ± 0.02	70 ± 16
1	0.41 ± 0.03	111 ± 28

B. Initial bed permeability

In the experiments, the bulk bed permeability k was estimated from the bulk measurements of ΔP and v_f using Darcy's law,

$$k = \frac{v_f}{\Delta P}\eta h, \tag{8}$$

where $\Delta P = P_{inlet} - P_{atm}$. Experiments were performed to measure how the bulk permeability k varied as a function of c (see black dots in Fig. 4) in the undeformed bed. These experiments were performed at low-filtration velocities in a

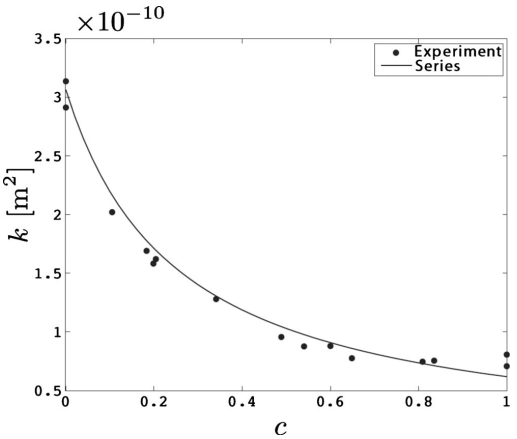

FIG. 4. Permeability k of the initial bed [see Fig. 3(A)] as a function of c. Black dots represent experiments while the solid line is predicted by the conductors in series model described in the text. Values of $\phi=0.35$ and $K=7.8$ were used in addition to the given values of d_1 and d_2.

smaller box, with a gap spacing equal to that of the Hele-Shaw cell, to ensure that bed deformation did not occur.

Good agreement with the measured permeability was obtained (see Fig. 4) using a conductor in series model to estimate the theoretical permeability (k_t^s),

$$\frac{1}{k_t^s} = \frac{c}{k_1} + \frac{(1-c)}{k_2}. \tag{9}$$

The model is consistent with the observed striped pattern with stripes perpendicular to the flow direction. The end member permeability k_1 and k_2 for $c=0$ and 1 respectively can be estimated from the Carman-Kozeny relation, assuming a constant porosity of $\phi=0.35$,

$$k_i = \frac{\langle d_i \rangle^2}{4K} \frac{\phi^3}{(1-\phi)^2}, \tag{10}$$

with grain sizes $\langle d_1 \rangle$ and $\langle d_2 \rangle$.

By combining Eqs. (10) and (9) an analytic model for the total permeability was obtained. This model predicts that

$$k_t(c) = \frac{1}{K} \frac{d_1^2 d_2^2}{c d_2^2 + (1-c) d_1^2} \frac{\phi^3}{(1-\phi)^2}, \tag{11}$$

and this relationship is represented by the solid line in Fig. 4.

C. Observations of dynamical pattern growth

The observed morphologies can be divided into four different groups: the Darcy flow (DA) regime in which the bed remains static; the Nucleation of Pipes (NP) regime in which pipes consisting of large particles grow in the wake of a localized fluidized zones; the deeply rooted pipes (DRP) regime in which vertical pipes consisting of large particles grow from the bottom of the cell; and the full separation (FS) regime in which complete separation of the large and small grains occurs. Each pattern forms in different regions of the control parameter space (c, v_f) (see Fig. 3).

Experiments were performed to quantify the transient dynamics of the pattern growth in the NP, DRP, and FS regimes. The different regimes occurred over a wide range of concentrations, but unless otherwise stated, the experiments were performed at $c=0.75$.

1. Darcy flow regime with an undeformed bed (DA)

At filtration velocities below the critical velocity, $v_f < v_{f1}(c)$, represented by the black stars in the morphology diagram (Fig. 5), the air seeps through the bed without deforming it. A linear relation between v_f and ΔP was observed, and the bulk bed permeability k is well defined by Eq. (8).

2. Nucleated pipes (NP)

At filtration velocities $v_{f1} < v_f < v_{f2}$ represented by the red diamonds in Fig. 5, local fluidization occurred within the bed. The growth of a single pipe in the wake of a localized fluidized zone is shown in Fig. 6 with the full system illustrated in Fig. 3(B).

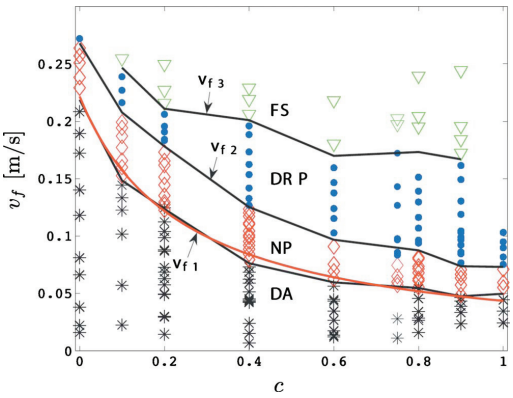

FIG. 5. (Color online) Experimental morphology diagram in a (v_f, c) cut through the parameter space. Black stars represent incipient motion without bed deformation; red diamonds indicate the nucleation of pipes pattern; blue dots represent the deeply rooted pipe pattern; and green triangles represent the full separation pattern. The red line is the calculated transition for v_{f1} based on Eq. (12) at the onset liquefaction.

The bulk behavior of the NP-pattern was studied by increasing v_f in a stepwise manner [Fig. 7(A)]. In Fig. 7(B) k is plotted as a function of time showing how the permeability k increased with increasing v_f, and remained essentially constant for essentially constant v_f. The evolution of the fluidized area A_f, obtained from image analysis, is indicated by the green (gray) line in Fig. 7(A). The plot shows that A_f increased rapidly as v_f was increased. For fixed v_f, the bed reorganized itself by sedimenting out the large grains resulting in a decreasing A_f.

By using the expression for k [Eq. (11)] into the equation for v_c [Eq. (5)], we can predict v_{f1} at the initiation of the NP-pattern as a function of c,

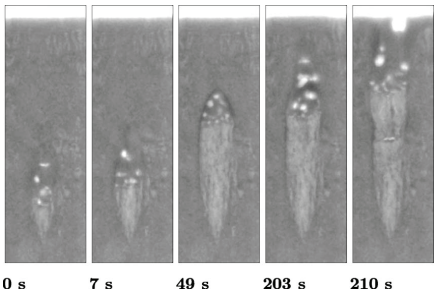

FIG. 6. The evolution of a single pipe nucleated 8 cm below the upper surface at constant in-flow conditions. The light gray area corresponds to a zone with a larger fraction of large particles, while the white zones are air bubbles, indicating fluidization. The bubbling nucleates on top of the vertical gray pipes. The pipe grew slowly upward by erosion at the upper tip of the fluidized zone and sedimentation of the large particles. The fluidized zone eventually breached the top surface after 210 s. The images are 2 cm wide.

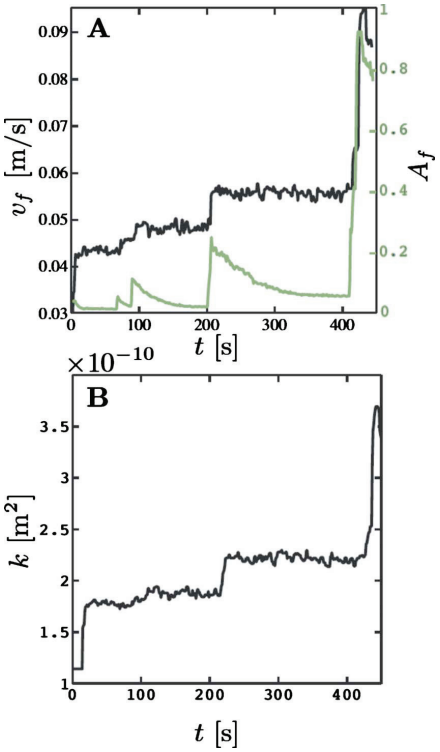

FIG. 7. (Color online) Bulk characterization of the NP-pattern for $c=75\%$.A) The imposed filtration velocity v_f, in black, and the fluidized area A_f, in green (gray), as a function of t. B) The corresponding evolution of the permeability k.

$$v_{f1}(c) = \frac{1}{4K}\frac{d_1^2 d_2^2}{c d_2^2 + (1-c) d_1^2}\frac{\phi^3}{(1-\phi)^2}\frac{\rho_b g}{\eta}, \qquad (12)$$

and a value of 3.6 for K matches the onset of the NP-regime in the morphology diagram (see the red line in Fig. 5).

The long time behavior of the NP pattern is characterized by individual fluidized regions that grow upwards and approach the upper surface where the unavailability of large particles prevents further growth. Alternatively, deeper pipes grow into regions of high permeability (other pipes) and they no longer support fluidization, except at the top of the pipes that they have merged with.

3. Deeply rooted pipes (DRP)

At filtration velocities $v_{f2} < v_f < v_{f3}$ the large particles settle out of an initially fluidized mixture forming a static zone that is not fluidized, and the DRP-pattern emerges (blue dots in Fig. 5). A video of the dynamic evolution of the DRP-pattern can be accessed as supplementary material [68]. The growth of pipes originating from the bottom of the cell is shown in Fig. 8, while the large (system) scale pattern is illustrated in Fig. 3(C). The brighter pipes consist of large beads [Fig. 2(C)] and act as regions of elevated permeability (Fig. 4).

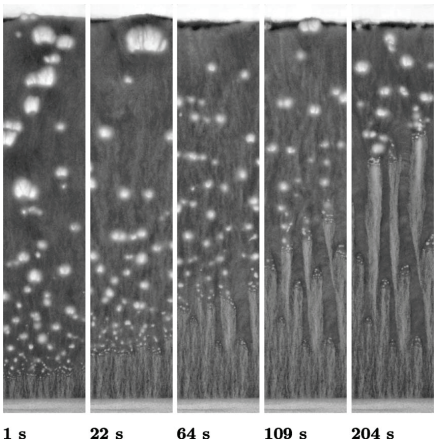

FIG. 8. Transient evolution of the DRP-pattern at a constant inlet flow velocity. Light gray areas correspond to static zones with a larger proportion of large particles (pipes), while the white regions in the fluidized zone above, are air bubbles. At the start of the experiment the whole bed was initially fully fluidized and bubbling occurred everywhere. The interface between the upper fluidized and the lower nonfluidized layer moved upward through time as large particles sediment out of the fluidized zone. Within the nonfluidized zone, just below the interface, the number of pipes decreased with time. In the rightmost pictures it can be seen that air bubbles nucleate only from the top of the three pipes. Each image is 7 cm wide and the bed height is 35 cm.

The dynamics of the granular system in the DRP regime differs from the dynamics in the NP regime in two important ways. First, the pipes grow from the bottom of the bed (from the top of the sintered layer), and second, the bed is initially fully fluidized. The fluidized region is characterized by intense bubbling, and the bubbles nucleate at the upper tips of the vertical pipes and rapidly rise to the upper surface. We observed a variety of phenomena in the fluidized phase, including the attraction between and coalescence of individual bubbles, the formation of a collapse structure in their centers, and acceleration of the bubbles during their ascent. These effects are not studied in this paper, but [69,70] (and references therein) give a description of related phenomena.

Quantitative characterization of the DRP-pattern was performed for a constant filtration velocity of $v_f = v_{f2} = 0.09$ m/s for $c=0.75$. The interface between the fluidized and defluidized zones was identified using image subtraction, and an example is shown by the cyan line in Fig. 9(A). The interface shifted upward as the large particles sedimented out of the fluidized mixture, and it was also observed that the interface coarsened during this process [Fig. 9(B)]. Typically, a local depression in the interface profile is associated with bubble nucleation on the tips of the pipes within the static zone [Fig. 9(A)].

The light intensity profile along the red line in Fig. 9(A), 1 cm below the moving fluidization interface (cyan) was

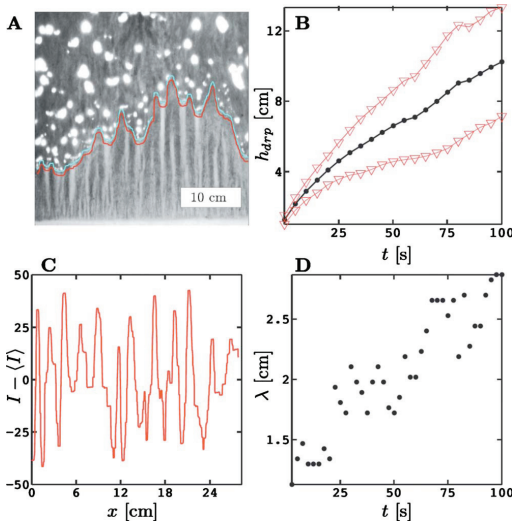

FIG. 9. (Color online) Characterization of the DRP-pattern for $c=75\%$ and $v_f=0.09$ m/s. A) Snapshot of the evolving pattern in the DRP regime. The interface between the static and fluidized zone is indicated by the upper (cyan) line. The light intensity profile was extracted from the image along the lower (red) line (just beneath the line indicating the interface). B) Plot of the evolution of the mean height and the standard deviation of the interface between the fluidized and static zone. The interface grows toward the surface while it roughens. C) Light intensity along the red line. D) Correlation length obtained from the light intensity signal within the static zone using a 1-dimensional auto correlation analysis. The horizontal correlation length λ in the light intensity coarsens as the pipes grow through time.

analyzed. The transmitted light intensity profile, shown in Fig. 9(C), was used to calculate the correlation length λ with a 1D auto correlation method. Figure 9(D) shows how λ increased from ~1 cm to ~3 cm during the first 100 s of the experiment, and this provides a measure of the increased distance between pipes and the dynamic coarsening of the system.

The evolution of the fluid velocity v_f and the ratio between the gas pressure difference across the granular material and the weight of the bed (the reduced pressure),

$$\tilde{P} = \Delta P/\rho_b g h, \tag{13}$$

under constant inlet conditions, differ for DRP patterns and NP patterns. For the NP-patterns k, the ratio between v_f and $\tilde{P}$, remained essentially constant for constant inlet conditions during the evolution of the NP patterns [Fig. 7(B), see the evolution between $t\sim200$ and ~400 sec]. For the DRP pattern measurements shown in Fig. 10, v_f remained more-or-less constant while the reduced pressure across the bed $\tilde{P}$ decreased. This corresponds to an increase in the bulk permeability as the DRP-pattern grows. The long time behavior of the DRP pattern is characterized by vertical pipes extending to a fixed distance from the top of the system above which a fluidized zone exist, depleted by large grains.

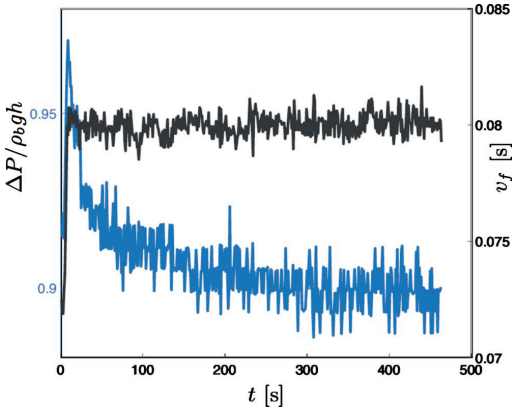

FIG. 10. (Color online) The reduced pressure difference [Eq. (13)] across the granular medium during evolution of the DRP pattern for $c=0.75$ (blue lower curve). The reduced pressure decreased while the interface between the fluidized and stagnant region rose toward the surface [see Fig. 9(B)]. v_f (the black upper curve) remained constant throughout the growth process.

4. Full separation (FS)

At filtration velocities $v_f > v_{f3}$, FS of the two grain sizes occurred (green triangles in Fig. 5) and no vertical structure was observed in the de-fluidized zone [Fig. 3(D)]. The bright zone of nonfluidized large particles grows upward through time, and bubble nucleation is evenly distributed along the interface between the fluidized and static zone.

In order to quantify the dynamics of the FS pattern, the variation of the interfacial growth rate as a function of c and h (Fig. 11) was investigated. An image subtraction method was used to track the vertical position of the interface (h_{fs}) between the fluidized and static zones. By scaling h_{fs} by the quantity of large particles $h(1-c)$, a data collapse was obtained for all four experiments (see Fig. 11). The long time behavior of the FS pattern is characterized by the full separation of the beads into a static zone beneath a fluidized bed of smaller particles.

5. Evolution from DA to FS

An experiment was performed to investigate how the relationship between the pressure difference across the granular bed ΔP and the filtration velocity v_f differed in the various regimes. For that purpose v_f was increased by small steps and ΔP was measured during the stationary regime subsequent to the velocity change. In Fig. 12, the corresponding reduced pressure, defined in Eq. (13), is plotted versus v_f showing that the reduced pressure and the pressure difference across the granular medium saturates at the initiation of the DRP pattern. Consequently the permeability, which is defined in Eq. (3) as the inverse of the local slope in the ΔP-v_f plot increases linearly with increasing infiltration

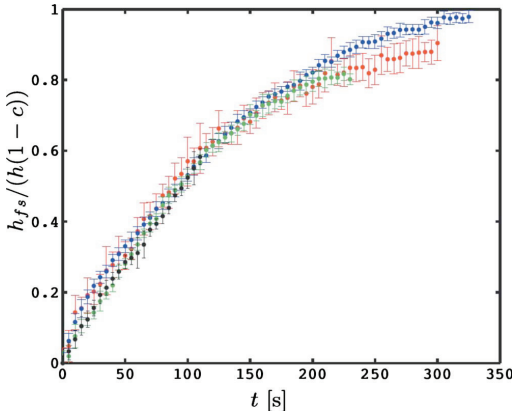

FIG. 11. (Color online) Scaled height of the interface between the static and fluidized zone for the FS-pattern through time from four different experiments with h=[0.31,0.23,0.35,0.30] and c =[0.83,0.60,0.75,0.70]. A data collapse was obtained. Determination of the slope from the initial linear regime can be used to deduce a characteristic time of $t_c \sim 200$ s required for the large particles to settle.

velocity for velocities exceeding v_{f2} (at the initiation of the DRP regime).

V. DISCUSSION

A. Experimental considerations

A number of observations not directly related to the pattern formation processes were made. At low-gas velocities $v_f < v_{f1}$ a depression, with a more-or-less parabolic profile (in the plane of the cell) formed in the top surface at the instant when gas was injected into the bed. The maximal depth of the depression was up to ~3 mm near the center of the HS cell. The abrupt formation of the depression and its parabolic profile suggest that out of plane bending of the glass plates occurred. Additional increase in the depth of the depression was observed on longer time scales at constant gas velocities, indicating that slow creep induced by grain re-organization was occurring. After 20 h an additional ~1 mm of compaction was observed in the center of the cell.

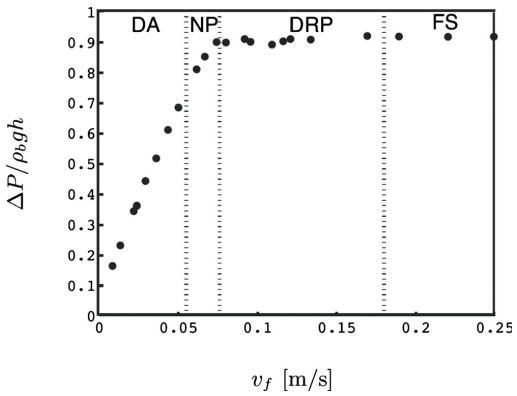

FIG. 12. Reduced pressure drop after relaxation to steady state for c=0.75. The reduced pressure drop $\tilde{P}$ [Eq. (13)] is plotted versus v_f for large times, i.e., in the steady state in which the growth rates for the different patterns (in Figs. 9 and 7) have approached zero.

The Janssen effect [71] occurring in constrained granular systems, in which wall friction reduces the vertical stress component deep in the granular material could have an influence on the initial fluidization criterion in Eq. (5). Further, anisotropy may occur in the fluidized phase due to differences between the particle-particle and particle-wall interactions. We speculate that these effects may be responsible for the localized bubbles observed at the top of vertical pipes in the NP-regime (see Fig. 6).

The filling procedure produced a layered structure (see Fig. 3, **DA**) which caused a spatial variation in the permeability field. The experimental results were insensitive to the cell filling procedure and the resulting heterogeneity, and the critical velocities $v_{f1,2,3}$ were reproducible. A thoroughly mixed bed, which can be produced by intense fluidization followed by a sudden stop of the imposed gas velocity, would have a higher permeability than the initial layered bed presented here. In such a bed, we expect a higher critical velocity v_{f1} due to reduced flow localization in the system, as predicted by Eq. (5). It is important to note that values of v_{f2}, the critical velocities marking the onset of the DRP pattern, would stay unaffected. This is due to the rapid reorganization of the initial granular medium when the system is first fully fluidized.

B. Patterns

The FS pattern has already been extensively discussed (cf Introduction) and thus we focus on the NP and DRP regimes in the following discussion.

1. Nucleated pipes (NP) pattern

A nucleated pipes (NP) pattern develops when fluidized zones nucleate within an initially static matrix at an imposed flow velocity of $v_{f1} < v_f < v_{f2}$. The heterogeneities in the bed induce variations in the local flow velocity and a corresponding localization of fluidization. Within the fluidized zones, the system reorganizes itself by sedimentation of the large particles while the fluidized zones propagates upwards leaving vertical pipes of elevated permeability behind. Focusing of the flow into the more permeable pipes maintains the localization of the fluidization.

Observations of the system scale behavior in the NP regime shows that increasing the infiltration velocity between v_{f1} and v_{f2} increases the area of fluidization and the number of nucleated pipes. The pipes nucleate progressively further down as v_f increases within the limits v_{f1} and v_{f2}.

Within geological systems the pore pressure is often considered to be the primary variable controlling the onset of a

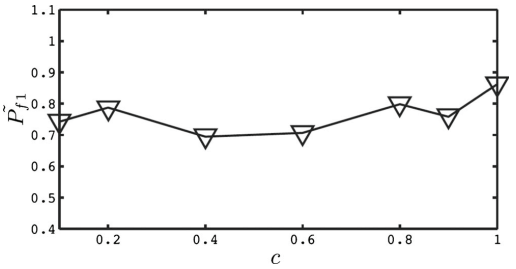

FIG. 13. Critical reduced pressure [$\tilde{P}_{f1}$, Eq. (13)] at the onset of the NP-pattern as a function of c. The reduced pressure is estimated from $v_{f1}(c)$ and $k(c)$ [Eq. (14)].

fluidized state. In order to compare the experiment to geological systems, the reduced pressure in Eq. (13), the ratio of the gas-pressure to the weight of the bed, was used. By substituting the measurements of the pressure difference across the granular bed ΔP in Eq. (13) by Darcy's law [Eq. (8)] the expression

$$\tilde{P} = \frac{v_f \eta}{\rho_b g k} \tag{14}$$

for the reduced pressure $\tilde{P}$ is obtained. $\tilde{P}=1$ if the total drag exerted on the bed by the flowing gas is equal to the weight of the bed.

The critical reduced pressure for the NP regime in Eq. (14) can be estimated using empirical data for $v_{f1}(c)$ (Fig. 5) and $k(c)$ (Fig. 4). Figure 13 shows how the critical reduced pressure, $\tilde{P}$, depends on the mass fraction of small particles, c. It is apparent that $\tilde{P}$ is essentially independent of c and all of the values of $\tilde{P}$ are consistent with a constant value of $\tilde{P}=0.76\pm0.05$. This value is significantly lower than the pressure required to lift the entire bed illustrating the importance of flow localization.

2. Deeply rooted pipe (DRP) patterns

DRP patterns develop when the large beads sediment out of an initially fully fluidized system [1]. For a monodisperse granular medium, balancing the gradient in the gas pressure and the bead density ρ_g (weight of beads per unit volume) yields,

$$\nabla P = -\rho_g g, . \tag{15}$$

By using Darcy's law [Eq. (3)] and the permeability as defined in Eq. (6) it can be seen that a critical diameter given by

$$d = \sqrt{4K \frac{v \eta}{\rho_g g} \frac{(1-\phi)^2}{\phi^3}}, \tag{16}$$

above which grains sediment, exists. For grains with equal density, restitution coefficient and shape, but different sizes, a situation may arise in which the large grains settle to the bottom of the cell while the remaining mixture, depleted of large grains, remains fluidized. The settling of the large grains shifts the interface between the fluidized and static regions upwards.

Fluidization is a prerequisite to grain rearrangement and the sedimentation of the large particles. The gas flow is focused through the brighter, more permeable vertical pipes inducing fluidization and bubbling at their tips. A feed back loop develops because the pipes focus the flow, which in turn focuses the fluidization and the resulting sedimentation of the large particles. The localized sedimentation enables further growth of the pipe.

C. Geological applications

The localization of fluid flow may be recorded in the rock mineralogy within the structure of geological systems. Important examples include carbonate minerals in sea bottom Pockmarks [51], zeolite minerals in hydrothermal vent complexes [49], and Kimberlite minerals in Kimberlites pipes [55].

There are always spatial variations of the grain size distribution in sedimentary rocks and unconsolidated sediment, and this causes nonuniform permeabilities leading to flow localization. As the fluid pressure builds up, and the shear strength decreases at depth, localized deformation may occur, leading to a variety of piercement structures. In many cases, the piercement structures form along the main pressure gradient, and they are thought to be responsible for fluid drainage, which may prevent large scale system failure. The analysis of the NP-pattern shows that the pressure at which these structures form can be significantly lower than the lithostatic pressure. This concept is termed under-fluidization and it may be of great relevance for evaluating the critical pressures required for the formation of the piercement structures mentioned in the introduction.

It has been proposed that the formation of vertical coarse grained pipes (on the cm to m scale), within large (up to km scale) Kimberlite pipes may be due to the sedimentation of the large grains during deceleration of the flow rate after the main emplacement fully fluidizes the system [58]. The proposed feed back mechanism for the DRP-pattern may also be relevant to a variety of other geologic settings in which the fluidization of, unconsolidated sediment or consolidated sediment after brecciation occurs. For example, in hydrothermal vent complexes, lithified cm-scale pipes are observed within the larger (tens to hundreds of meter scale) structure [48,49]. Another example of flow localization in fluidized systems is provided by mud volcanoes, which form and coexist over a range of scales including cm-scale gryphons and craters with diameters up to hundreds of meter [59–61].

VI. CONCLUSION

We have studied the dynamic growth of three patterns in partially fluidized bi-modal sized granular mixtures. Different segregation patterns form in different regions in the (c and v_f) control parameters space. NP patterns emerged at velocities in the range $v_{f1}<v_f<v_{f2}$. In this regime, pipes nucleate and grow within the bed due to the sedimentation of the large grains within localized fluidized zones. Deep rooted

pipes grow from the bottom of the bed, when $v_{f2} < v_f < v_{f3}$, and a DRP pattern is formed. The DRP-pattern emerges due to a feed back mechanism in which the interplay between flow localization, localized fluidization and localized sedimentation accelerates the further growth of the large grain pipes. FS patterns, formed when the two grain sizes segregate without any vertical structure in the static nonfluidized zone, were observed at imposed flow velocities exceeding $v_f > v_{f3}$. The dynamical growth of the three different patterns were characterized using image analysis in combination with the permeability deduced from the measurements of v_f and ΔP.

ACKNOWLEDGMENT

The project have been supported by a NRF grant to Physics of Geological Processes, UIO. Joachim Mathiesen is gratefully thanked for his constructive contributions. Two anonymous reviewers are thanked for their valuable comments.

[1] M. A. Gilbertson and I. Eames, J. Fluid Mech. **433**, 347 (2001).
[2] D. Gidaspow, *Multiphase Flow and Fluidization: Continuum and Kinetic Theory Descriptions* (Academic Press, New York, 1994).
[3] G. H. Ristow, *Pattern Formation in Granular Materials*, Springer Tracts in Modern Physics Vol. 164 (Springer Verlag, Berlin, 2000).
[4] J. Duran, *Sands, Powders and Grains* (Springe-Verlag, New York, 2000), Vol. 391.
[5] H. M. Jaeger, S. R. Nagel, and R. P. Behringer, Rev. Mod. Phys. **68**, 1259 (1996).
[6] P. G. de Gennes, Rev. Mod. Phys. **71**, S374 (1999).
[7] T. Le Pennec, K. Måløy, A. Hansen, M. Ammi, D. Bideau, and X. Wu, Phys. Rev. E **53**, 2257 (1996).
[8] C. T. Veje and P. Dimon, Phys. Rev. E **54**, 4329 (1996).
[9] J. B. Knight, E. E. Ehrichs, V. Y. Kuperman, J. K. Flint, H. M. Jaeger, and S. R. Nagel, Phys. Rev. E **54**, 5726 (1996).
[10] K. M. Hill, J. F. Gilchrist, J. M. Ottino, D. V. Khakhar, and J. J. McCarthy, Int. J. Bifurcation Chaos Appl. Sci. Eng. **9**, 1467 (1999).
[11] K. M. Hill, D. V. Khakhar, J. F. Gilchrist, J. J. McCarthy, and J. M. Ottino, Proc. Natl. Acad. Sci. U.S.A. **96**, 11701 (1999).
[12] N. Lecocq and N. Vandewalle, Phys. Rev. E **62**, 8241 (2000).
[13] J. M. Ottino and D. V. Khakhar, Annu. Rev. Fluid Mech. **32**, 55 (2000).
[14] J. M. Valverde, A. Castellanos, P. Mills, and M. A. S. Quintanilla, Phys. Rev. E **67**, 051305 (2003).
[15] R. V. Daleffe, M. C. Ferreira, and J. T. Freire, Braz. J. Chem. Eng. **25**, 83 (2008).
[16] A. B. Ezersky and F. Marin, Phys. Rev. E **78**, 022301 (2008).
[17] C. F. Harwood, Powder Technol. **16**, 51 (1977).
[18] E. Clement and J. Rajchenbach, EPL **16**, 133 (1991).
[19] A. Kudrolli, M. Wolpert, and J. P. Gollub, Phys. Rev. Lett. **78**, 1383 (1997).
[20] B. Cagnoli and G. P. Romano, J. Volcanol. Geotherm. Res. **193**, 18 (2010).
[21] J. P. Koeppe, M. Enz, and J. Kakalios, Phys. Rev. E **58**, R4104 (1998).
[22] M. A. Kessler and B. T. Werner, Science **299**, 380 (2003).
[23] M. G. Kleinhans, Earth-Sci. Rev. **65**, 75 (2004).
[24] J. M. N. T. Gray and K. Hutter, Continuum Mech. Thermodyn. **9**, 341 (1997).
[25] D. A. Robinson and S. P. Friedman. Physica A—Statistical Mechanics and its Applications **311**, 97 (2002).
[26] Y. M. Zhao and L. B. Wei, Fuel Process. Technol. **68**, 153 (2000).
[27] R. Jullien, P. Meakin, and A. Pavlovitch. EPL **22**, 523 (1993).
[28] M. Mourad, M. Hemati, and C. Laguerie, Powder Technol. **80**, 45 (1994).
[29] J. Leboreiro, G. G. Joseph, C. M. Hrenya, D. M. Snider, S. S. Banejee, and J. E. Galvin, Powder Technol. **184**, 275 (2008).
[30] K. G. Palappan and P. S. T. Sai, Chem. Eng. J. **139**, 330 (2008).
[31] L. H. Shen, M. Y. Zhang, and Y. Q. Xu, Chem. Eng. Sci. **50**, 1841 (1995).
[32] Y. Q. Feng, B. H. Xu, S. J. Zhang, A. B. Yu, and P. Zulli, AIChE J. **50**, 1713 (2004).
[33] M. J. Rhodes, X. S. Wang, M. Nguyen, P. Stewart, and K. Liffman, Chem. Eng. Sci. **56**, 2859 (2001).
[34] H. Umekawa, S. Furui, Y. Oshima, M. Okura, M. Ozawa, and N. Takenaka, Nucl. Instrum. Methods Phys. Res. A **542**, 219 (2005)
[35] O. Roche, M. A. Gilbertson, J. C. Phillips, and R. S. J. Sparks, Powder Technol. **166**, 167 (2006).
[36] G. Felix and N. Thomas, Phys. Rev. E **70**, 051307 (2004).
[37] B. Formisani, G. De Cristofaro, and R. Girimonte, Chem. Eng. Sci. **56**, 109 (2001).
[38] S. Y. Wu and J. Baeyens, Powder Technol. **98**, 139 (1998).
[39] D. Gauthier, S. Zerguerras, and G. Flamant, Chem. Eng. J. **74**, 181 (1999).
[40] A. Marzocchella, P. Salatino, V. Di Pastena, and L. Lirer, AIChE J. **46**, 2175 (2000).
[41] H. L. Lu, Y. R. He, G. Dimitri, L. D. Yang, and Y. K. Qin, Powder Technol. **134**, 86 (2003).
[42] J. L. Jacobsen, Phys. Rev. E **62**, R1 (2000).
[43] B. G. M. van Wachem, J. C. Schouten, C. M. van den Bleek, R. Krishna, and J. L. Sinclair, AIChE J. **47**, 1292 (2001).
[44] M. L. de Souza-Santos, Fuel **68**, 1507 (1989).
[45] P. Tang and V. M. Puri, Part. Sci. Technol. **22**, 321 (2004).
[46] E. Lemaire, P. Levitz, G. Daccord, and H. Van Damme, Phys. Rev. Lett. **67**, 2009 (1991).
[47] T. Hirata, Phys. Rev. E **57**, 1772 (1998).
[48] B. Jamtveit, H. Svensen, Y. Y. Podladchikov, and S. Planke, *Physical Geology of High-Level Magmatic Systems*, edited by C. Breitkreuz and N. Petford (Geological Society, London, 2004), pp. 233–241.
[49] H. Svensen, S. Planke, A. Malthe-Sørenssen, B. Jamtveit, R. Myklebust, T. R. Eidem, and S. S. Rey, Nature (London) **429**, 542 (2004).

[50] P. K. Harrington, Geo-Mar. Lett. **5**, 193 (1985).
[51] M. Hovland, M. Talbot, H. Qvale, S. Olaussen, and L. Aasberg, J. Sed. Petrology **57**, 881 (1987).
[52] C. J. N. Wilson, J. Volcanol. Geotherm. Res. **20**, 55 (1984).
[53] O. Roche, M. A. Gilbertson, J. C. Phillips, and R. S. J. Sparks, J. Geophys. Res., [Solid Earth] **109**, B10201 (2004).
[54] R. S. J. Sparks, L. Baker, R. J. Brown, M. Field, J. Schumacher, G. Stripp, and A. Walters, J. Volcanol. Geotherm. Res. **155**, 18 (2006).
[55] A. L. Walters, J. C. Phillips, R. J. Brown, M. Field, T. Gernon, G. Stripp, and R. S. J. Sparks, J. Volcanol. Geotherm. Res. **155**, 119 (2006).
[56] R. S. J. Sparks, R. J. Brown, M. Field, and M. Gilbertson, Nature (London) **450**, E21 (2007).
[57] T. M. Gernon, M. A. Gilbertson, R. S. J. Sparks, and M. Field, J. Volcanol. Geotherm. Res. **174**, 49 (2008).
[58] T. M. Gernon, R. S. J. Sparks, and M. Field, J. Volcanol. Geotherm. Res. **174**, 186 (2008).
[59] A. Mazzini, H. Svensen, G. G. Akhmanov, G. Aloisi, S. Planke, A. Malthe-Sørenssen, and B. Istadi, Earth Planet. Sci. Lett. **261**, 375 (2007).
[60] A. A. Jakubov, A. A. Ali-Zade, and M. M. Zeinalov, *Mud Volcanoes of the Azerbaijan SSR, Atlas* (Azerbaijan Academy of Sciences, Baku, 1971).
[61] S. Planke, H. Svensen, M. Hovland, D. A. Banks, and B. Jamtveit, Geo-Mar. Lett. **23**, 258 (2003).
[62] P. R. Cobbold and L. Castro, Tectonophysics **301**, 1 (1999).
[63] R. Mourgues and P. R. Cobbold, Tectonophysics **376**, 75 (2003).
[64] I. Eames and M. A. Gilbertson, J. Fluid Mech. **424**, 169 (2000).
[65] R. Mourgues and P. R. Cobbold, J. Struct. Geol. **28**, 887 (2006).
[66] www.glbeijer.no, tel: +47 32 82 90 80, email: firmapost@glbeijer.no, Internal product code: BEI037.
[67] M. K. Hubbert, Geol. Soc. Am. Bull. **62**, 355 (1951).
[68] See supplementary material at http://link.aps.org/supplemental/10.1103/PhysRevE.81.061305 for a movie of the dynamic evolution of the DRP-pattern.
[69] J. L. Vinningland, Ø. Johnsen, E. G. Flekkøy, R. Toussaint, and K. J. Maløy, Phys. Rev. E **76**, 051306 (2007).
[70] J. L. Vinningland, Ø. Johnsen, E. G. Flekkøy, R. Toussaint, and K. J. Maløy, Phys. Rev. Lett. **99**, 048001 (2007).
[71] H. A. Janssen, Z. Ver. Dtsch. Ing. **39**, 1045 (1895).

Paper II

Experimental and Analytic Modelling of Piercment Structures

Anders Nermoen, Olivier Galland, Espen Jettestuen, Kirsten Fristad, Yuri Podladchikov, Henrik Svensen, Anders Malthe-Sørenssen

Accepted in Journal of Geophysical Letters

Experimental and Analytic Modeling of Piercement Structures

A. Nermoen[1], O. Galland[1], E. Jettestuen[2,1], K. Fristad[1], Y. Podladchikov[1], H. Svensen[1], A. Malthe-Sørenssen[1]

Abstract. [1] Piercement structures such as mud volcanoes, hydrothermal vent complexes, pockmarks and kimberlite pipes, form during the release of pressurized fluids. The goal of this work is to predict under which conditions piercement structures form from the insights gained by sand box experiments injecting compressed air through an inlet of width w at the base of a bed of glass beads of height h. At an imposed critical velocity v_f, a fluidized zone consisting of a diverging cone-like structure formed with morphological similarities to those observed in nature. Dimensional analysis showed that v_f is correlated to the ratio of h over w. In addition, we derived an analytical model for v_f which are compared to the experimental data. The model consists of a force balance between the weight and the seepage forces imparted to the bed by the flowing gas. The analytic model reproduces the observed correlation between v_f and h/w, although a slight under-estimate was obtained. The results suggest that the gas-particle seepage force is the main triggering for fluidization and that the commonly used proxy, that the fluid pressure must equal or exceed the lithostatic weight, needs to be re-considered. By combining the experiments and the model, we derived critical pressure estimates which were employed to a variety of geological environments. Comparing the estimated and measured pressures prior to the Lusi mud volcano shows that the presented model over-estimates the critical pressures. The model paves the way for further investigations of the critical conditions for fluidization in Earth systems.

1. Introduction

[2] Piercement structures, the structures forming when fluids are forced through sediments and rocks, are common in nature and they manifest themselves in a variety cases ranging from pockmarks, mud volcanoes, hydrothermal vent complexes to kimberlite pipes. Despite their diverse origin, they show structural similarities consisting of circular pipes (and pipes within pipes) containing intensely deformed rocks, often brecciated, with a lack of internal structure [e.g., *Hovland et al.*, 1985; *Planke et al.*, 2003; *Jamtveit et al.*, 2004; *Svensen et al.*, 2006; *Sparks et al.*, 2006; *Walters et al.*, 2006].

[3] On seismic data, piercement structures are inferred from pipe-like domains marked by discontinuities of the seismic reflectors, with large height to width ratios [e.g., *Lancelot and Embley*, 1977; *Planke et al.*, 2005; *Hansen*, 2006; *Moss and Cartwright*, 2010]. Field data shows that the pipes contain brecciated elements with lithologies differing from the surrounding rocks. Moreover, mud volcanoes and hydrothermal vent complexes are normally surrounded by inward dipping strata suggesting a convective movement within the pipes, where rocks are transported upward in the centre and with a downward collapse of the adjacent margin (see Figure 1 and e.g. [*Planke et al.*, 2003; *Svensen et al.*, 2006; *Walters et al.*, 2006; *Svensen et al.*, 2007b]).

[4] In some hydrothermal vent complexes, e.g. the Witkop II and III complexes in the Karoo Basin (South Africa), pipes containing fine grained fluidized sand are observed and an occurrence of zeolites indicate that hydrothermal fluids are involved in their formation [*Svensen et al.*, 2007b]. In off-shore pockmarks, fluids are sometimes observed seeping out of the craters [e.g., *Hovland et al.*, 1987; *Karpen et al.*, 2006]. The observations listed above shows some of the evidences indicating the close association between pipes and localized zones of elevated fluid pressures, although the cause and effect at the formation of piercement structures is not obvious, e.g. how can circular pipes form when consolidated sediments are brecciated by pressurized fluids?

[5] The mechanism for fluid pressure build-up varies between the different geological cases:

a) The origin of the pressures for the formation of sea-floor pockmarks have been explained by several hypotheses [*Hovland et al.*, 1985] such as the rapid expulsion of various gases, especially methane, originating from depth. Alternative hypotheses suggests that pockmarks form in response to the pressure build-up due to rapid pore-collapse of water bearing quick clay [*Harrington*, 1985], or, that they form when ground water is expelled onto the sea-floor [e.g., *Jensen et al.*, 2002; *Karpen et al.*, 2006].

b) Mud volcanoes are regularly observed in settings with organic rich, water- bearing sediments with a high sedimentation rate and low geothermal gradient causing the build-up of fluid pressure at depth [e.g., *Jakubov et al.*, 1971; *Dimitrov*, 2002; *Planke et al.*, 2003; *Svensen et al.*, 2007a; *Mazzini et al.*, 2007].

c) Hydrothermal vent complexes form in volcanic basins during magmatic sill emplacement into sedimentary rocks [e.g., *Jamtveit et al.*, 2004; *Svensen et al.*, 2004; *Planke et al.*, 2005]. The heat transported into the sediments results in rapid maturation of the organic compounds and boiling of the pore water, leading to rapid buildup of the fluid over-pressure.

d) Kimberlite pipes form when ascending volatile-rich kimberlite magma is decompressed, causing exsolution of fluids out of the magma leading to magmatophreatic eruptions which result in deeply rooted explosions [e.g., *Woolsey et al.*, 1975; *Clement*, 1975; *Lorenz*, 1975; *Walters et al.*, 2006; *Lorenz and Kurszlaukis*, 2007].

[6] Despite the fact that the geological examples are of very different scales and origins, this study aims at explaining them within a unique framework. Whatever the details of the pressure build-up mechanism at depth, the overlying rocks deform, and the fluids are released through eruptions at fluid pressures exceeding a critical pressure. In this study we aim at understanding under which physical conditions, with a focus on the critical pressures at which, eruptions occur and piercement structures may form.

1.1. Mechanical Effects of Elevated Pore Fluid Pressure

[7] It is well known that the effective strength of rock is reduced by elevated fluid pressures [*Terzaghi*, 1943]. In addition, fluid pressure gradients within a porous material induces a fluid flow affecting

[1]Physics of Geological Processes, University of Oslo, P.O. Box 1048 Blindern, N-0316 Oslo, Norway

[2]International Research Institute of Stavanger (IRIS), Prof. Olav Hanssensvei 15, 4068 Stavanger, Norway

0148-0227/10/$9.00

the stress state in the solid matrix [e.g. *Paterson and Wong*, 2006]. Consequently, this effect changes the Mohr circle causing yielding in situations that would otherwise be stable [e.g., *Sibson*, 2003; *Cox*, 2005]. *Mourgues and Cobbold* [2003] demonstrate how seepage forces induced by gradients in the pressure changes the total stress state in a simple sand box model. *Cobbold and Rodrigues* [2007] use this concept to show how bedding-parallel veins of fibrous calcite may form under lithostatic conditions.

[8] If the local pore fluid pressure exceeds a critical threshold, given e.g. by the effective strength of the subjected material, fluid-induced deformation occurs that effectively expel the pressurized fluids onto the surface. Possible deformation mechanisms range from focused deformation generating tensile hydraulic fractures, to a deformation of a more diffuse, less focused nature, when the matrix moves together with the flowing fluid [*Lemaire et al.*, 1991; *Hirata*, 1998]. In addition to that, the localization of over-pressures may cause localized compaction that generate porosity waves that can significant alter to the flow pattern in a solid matrix [*Connolly and Podladchikov*, 1998; *Chauveau and Kaminski*, 2008].

[9] The matrix deformation mechanism that realizes itself in response to the injected fluids depends on the physical properties of both the infiltrated fluids, the properties of the subjected material and the stress state of the solid. It is un-clear how the different deformation mechanisms impedes or accelerate each other in the different cases. For example, the threshold between the different regimes can be related to a threshold permeability or porosity. In the case of a local reduction of porosity at the front of the porosity wave, the fluid pressure will increase such that fluidization may occur. On the contrary, however, fluidization may become easier at larger porosities.

[10] Another example include the history dependence within dynamically evolving systems. When the fluid pressure exceeds a critical limit e.g. *Rozhko et al.* [2007], hydro-fracturing and brecciation of consolidated materials may occur. If the pressure gradient is maintained, the brecciated elements may fluidize during later stages of the emplacement process. In this case, it might be the fluidization process that one observes within in piercement structures today (e.g. for the Venetia Kimberlite structure in South Africa [*Walters et al.*, 2006]). Fluidization/liquefaction is defined as the solid-liquid phase transition occurring when the matrix no longer can withstand any differential stresses imparted to the system. In this case shear strength drops to zero and the matrix starts moving in response to the interstitial flow of air [*Kunii and Levenspiel*, 1969; *Gidaspow*, 1994; *Dudukovic et al.*, 1999; *Wilhelm*, 2000]. See section 4.4.

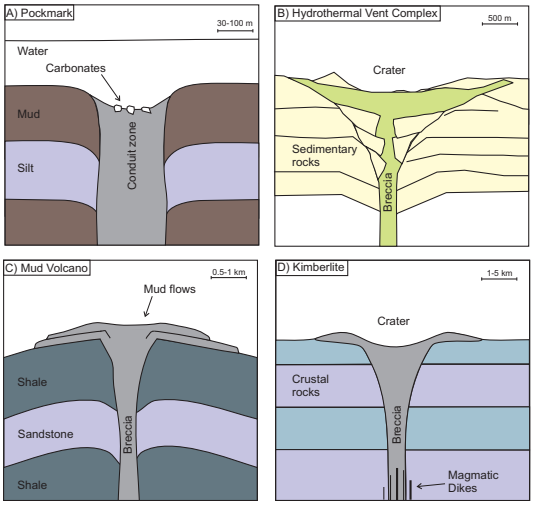

Figure 1. (Color online) A schematic drawing of different piercement structures in nature. a) Sub-marine pockmarks off-shore Norway, after *Hovland et al.* [1985]. b) Witkop II hydrothermal vent complex, Karoo Basin, South Africa, after *Svensen et al.* [2006]. c) Mud volcano Azerbaijan, after *Planke et al.* [2003]. d) Kimberlite pipe, Botswana, after *Walters et al.* [2006].

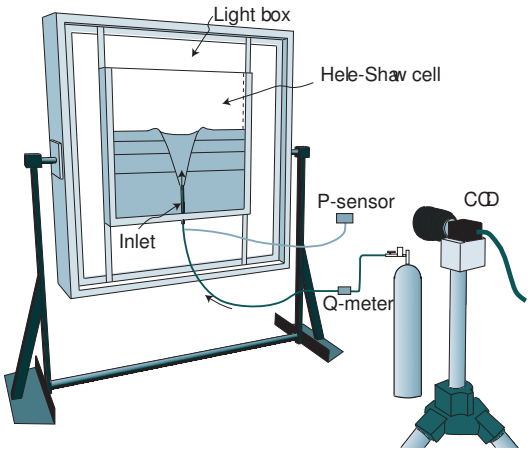

Figure 2. Sketch of the experimental setup used in this study consisting of a vertically oriented Hele-Shaw cell with back-lighting. Air was injected into the bed of glass beads through an inlet. Inlet area and/or filling height were varied for each experiment.

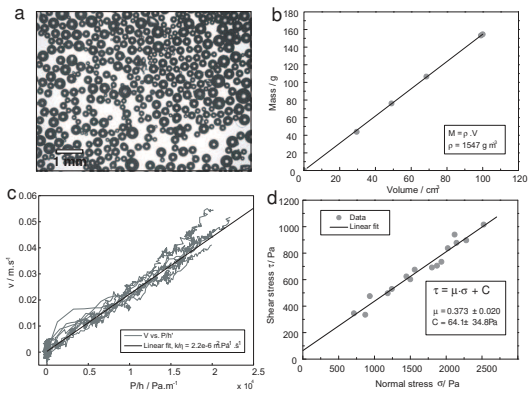

Figure 3. a) Microscope image of the glass beads ($d = 280 \pm 50\mu$m) used in the experiment. The white dot in the centre of each bead is caused by an illumination effects as the light is transmitted through the bead. b) Mass versus volume plot used to estimate the packing density ($\rho_b = 1547$ kg m^{-3}). c) Measurements of air velocity versus air pressure gradient ($\sim P/h'$) through a tube for varying filling heights h' of glass beads. The slope is defined as the k/η ratio. d) Plot of shear stress at failure versus applied normal stresses for the glass beads. The slope of the trend gives the friction coefficient μ of the packing of glass beads, while the intercept gives the cohesion C.

[11] The process of fluidization, when the previously static solid-like material changes to a flowing, liquid-like state, has been widely studied during the last decades. *Jaeger et al.* [1996] reviewed the phases and phase transitions of granular materials and showed how the solid-liquid transition can be induced by several mechanisms such as shaking, pouring and the interstitial flow of fluids [*de Gennes*, 1999].

[12] The physical conditions determining the onset of fluidization were studied by e.g. *Kunii and Levenspiel* [1969], who first defined the concept of the minimal velocity of fluidization. This concept is based on the quasi static approximation obtained when the fluid-particle viscous drag balances the buoyant weight of the matrix. This concept has been used in several experimental studies on fluidization applied to the emplacement of Kimberlite volcanoes [*Woolsey et al.*, 1975; *Freundt and Bursik*, 1998; *Walters et al.*, 2006; *Sparks et al.*, 2006]. However, a qualitative and quantitative application of fluidization to the formation of piercement structures in general has not yet been performed. In numerical continuum models, fluidization has been simulated by the use of e.g. Bingham rheologies where the effective rheological material properties depend on the subjected stress. In these models, fluidization is simulated by abrupt drop in the viscosity [e.g., *Mazzini et al.*, 2008], or the previously elastic material changes to a flowing viscous behaviour [e.g., *Gittings et al.*, 2006], when the differential stresses exceed a selected critical level.

[13] In geology, several different mechanisms lead to localized increased fluid pressures at depth. It is observed that in apparently similar geological settings the fluid pressure sometimes does, and other times does not, form piercement structures. For physical parameters below a critical limit, darcian flow is sufficient to bring the influx of fluids (related to the rate of fluid production) to the surface. Analogously, above the critical limit, darcian flow is insufficient as a fluid transport mechanism leading to unstable situations arise where the fluid pressure builds up, and highly permeable pathways represented by the piercement structures form. When the specific conditions are met, the piercement structures connect the pressure anomaly to the free surface causing rapid releases of the pressurized fluids. We use this scenario to explore the governing physical parameters and their internal quantitative relationship that determine the onset of fluidization.

[14] In this study we use the results from a well-defined experiment as a starting point to discuss the formation of piercement structures in some selected geological settings. When designing the experiments, a vertically oriented Hele-Shaw cell, equivalent to the ones used by e.g. *Rigord et al.* [2005] and *Johansen et al.* [2008] was used. We will show that the critical velocity increases with the ratio of the filling height by the inlet width as a power law with an exponent close to one. Then, we derive an expression for the venting number that enables us to estimate the critical fluid over-pressure for the formation of piercement structures in general. We apply our results to four specific geological cases where we estimate the critical pressure at formation. The cases are: the Lusi mud volcano (Indonesia), hydrothermal vent complexes in Karoo (South Africa), pockmarks (off-shore Norway) and kimberlites (Venetia Kimberlite structures, South Africa). We compare the calculated pressure estimates with the pore-pressure measurements in a nearby drilling well prior to the Lusi mud volcano eruption [*Mazzini et al.*, 2007].

2. Methods

2.1. Experimental Setup

[15] The experimental setup consisted of a vertically oriented Hele-Shaw cell (HS-cell) consisting of two parallel glass plates 0.8 cm apart. (see Figure 2). The 59 cm wide glass plates are sealed at the bottom and at the two sides and open at the top. A replaceable inlet is raised 7 cm into the cell to prevent the airflow to focus along the walls of the HS-cell. Four inlet widths w were used ($w = 3$, 9, 25, and 59 mm), each with breadth $b = 7$ mm. Each experiment was prepared by slowly pouring glass beads, through a funnel, from the top of the fixed HS cell to a desired filling height h, between 1 and 25 cm, measured from the upper tip of the inlet to the free surface. By using the funnel in the filling procedure we could control the filling height and make a bed with a flat surface. This produced a similar initial packing for each experiment, although some striped features in the transmitted light intensity were observed. The gradients in the transmitted light intensity is associated with local variations in bead size and porosity in the packing. This effect arise when differently sized beads segregate when poured into the cell [*Lebron and Robinson*, 2003]. The filling procedure, and thus the formation of the initial packing heterogeneities, was not varied systematically in the experiments, but this did not, as seen later, affect the reproducibility of the experiment. Therefore it is considered second order.

[16] Over-pressurized air was injected into the bead bed through the inlet placed within the bed. The inlet air flux (Q) was controlled by slowly opening a valve nearby a Omega FMA-1610 flow meter $\sim$ 1 m from the inlet. The air over-pressure was recorded in a T-junction (with an inner diameter of 2.45 mm) 10 cm from the inlet by a Omega PX139-004 DV pressure sensor (Figure 2). In the experimental setup we controlled the flux, whilst the pressure measurements varied as a proxy of the bulk permeability in the overlying bed. Digital grayscale images were captured at 20 frames per second by a high-resolution Jai CV-M4 CCD camera with a Nikon AF Nikkor 20mm lens. A Labview [*Labview*] program triggered the simultaneous logging of the pressure, flow measurements and the images. The inlet air flux was slowly increased until deformation of the overlying bed occurred. At this point in time, the critical values of flux and pressure were recorded.

2.2. The Material

[17] Beijer glass beads [*Beijer glass beads*, @] was used in the experiments. The glass beads had a close to spherical shape (Figure 3a), with a diameter in the range of $d = 280 \pm 50\mu$m. The porosity (ϕ) of the packing was estimated from measurements of the bed density ρ_b =1547 kg m^{-3} (Figure 3b) and the density of silica glass $\rho_g = 2460$ kg m^{-3}, yielding a bulk porosity of $\sim 37\%$ [e.g., *Bernal and Mason*, 1960; *Jaeger and Nagel*, 1992].

[18] The permeability k the packing of beads was estimated from the ratio of the measured air filtration velocity (v) and pressure difference (P) using Darcy's law,

$$k = -\frac{v\eta h}{P}, \tag{1}$$

where η is the viscosity of the gas, and h is the filling height. For the k-measurement we used a tube with a diameter of 3.5 cm filled with glass beads. Wall effects are expected to be negligible within these measurements since the diameter of the tube exceeds more than 25 particle diameters. This procedure was repeated for eight different filling heights (h' = 17, 24, 44, 44, 57, 65, 76 and 78 cm). Figure 3c shows how the measurements of the velocity versus the pressure gradient (P/h') collapses onto a common curve. The slope yields an estimate for the ratio of the permeability by the air viscosity k/η. The linear fit of the data gave $k/\eta = 6.8 \pm 0.4 \cdot 10^{-6}$ m^2 Pa^{-1}s^{-1}. Given an air viscosity at 20°C, of $1.76 \cdot 10^{-5}$ Pa s this yields a permeability of $1.2 \pm 0.4 \cdot 10^{-10}$ m^2. These experiments were performed at very low fluxes to prevent non-linear effects of turbulence, dynamic pressure and dynamic permeability induced by deformation of the matrix. The measured value is comparable to the Carman-Kozeny estimate [*Carman*, 1937] of the permeability given by the measurements of the mean particle diameter and the porosity,

$$k = \frac{\langle d \rangle^2}{45} \frac{\phi^3}{(1-\phi)^2} \simeq 2.2 \cdot 10^{-10} m^2. \tag{2}$$

[19] In order to characterize the mechanical properties of the packing we estimated the cohesion (C), the frictional coefficient (μ) and internal angle of friction (γ) using a classical Hubbert-type

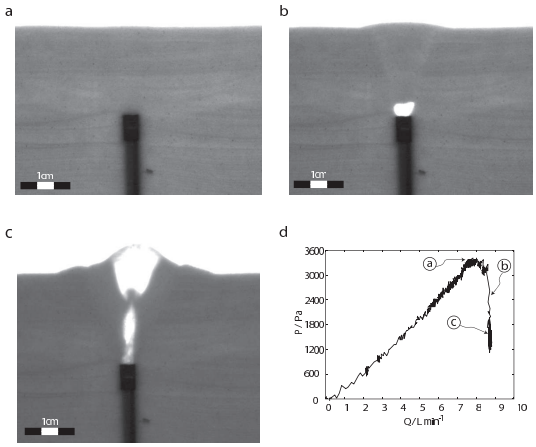

Figure 4. (a) to (c) Pictures of the experiment 11 at three stages (w = 0.9cm and h = 7cm). Picture (a) shows the initial configuration of the bed. In picture (b) and (c) a bubble form above the inlet that instantaneously grows to the surface triggering the onset of fluidization. Dilation can be seen as brighter region extending upwards at an angle from the inlet onto the surface in picture (b). A distinct crater formed on top in picture (c). (d) Plot of the measurements of the pressure P versus volumetric flux Q, with the pictures indicated along the measurement. At fluidization, the pressure drops from ∼3400 to ∼1500±300 Pa while Q remains constant.

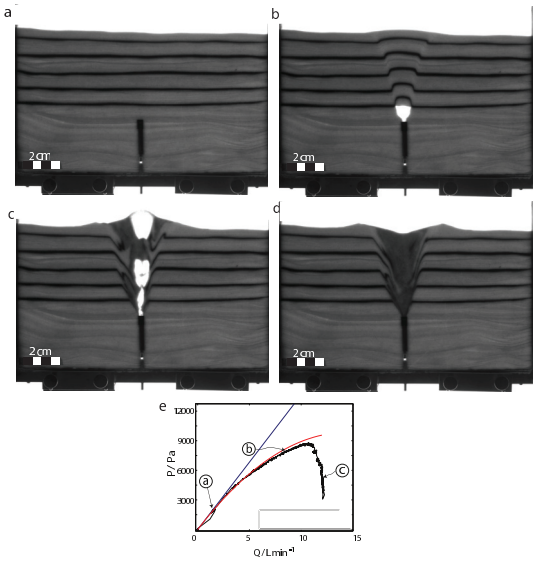

Figure 5. (a) to (d) Picture of an experiment at four different stages ($w = 0.9$ cm and $h = 17$ cm). The passive markers are spray painted glass beads. Picture (a) shows the starting configuration. In picture (b) a tiny static bubble forms above the inlet. In picture (c) the bubble rapidly grows to the surface and a fluidized cone (trapezoid) develops. In picture (d) the air supply is switched off. A distinct crater has formed and the passive markers dip inward along the margin of the zone. (e) Plot of measurements of the pressure P versus the inlet flux Q during the evolution of the experiment, with the pictures indicated along the plot. The curved red line shows the pressure corrected by the dynamic pressure described in section 4.2.1. At fluidization (c) the pressure drops from ∼8000 to ∼4000±1000 Pa while the inlet flux remains constant.

apparatus [*Hubbert*, 1951; *Schellart*, 2000; *Galland et al.*, 2007]. For each shear test experiment, the shear stress (τ) required for failure under a given normal stress (σ) was measured. The normal stresses ranged from 700 Pa to 2500 Pa and the measured shear stresses are plotted in Figure 3d where the linear trend defines the Mohr-Coloumb (M-C) envelope. The slope of the M-C envelope is defined as the frictional coefficient, with the internal angle of friction defined as $\gamma = \arctan(\mu)$. By extrapolating of the failure envelope down to zero normal stress the cohesion of the glass beads could be estimated. The best linear fit of the M-C envelope gave $\mu = 0.37 \pm 0.02$ and $\gamma = 20 \pm 1°$ with a cohesion of $C = 64 \pm 34$ Pa. The relatively large value of C is discussed in section 4.1.

3. Results

[20] Each experiment started with a static granular bed in the Hele-Shaw cell as seen in Figure 4a and 5a. The imposed air flux was slowly increased by manually opening a valve to a chamber containing compressed air. The pressure and flux were increased slowly until fluid induced deformation were observed in the matrix. At the initiation of deformation the critical conditions for flow velocity and pressure were recorded.

[21] In the high filling experiments with $h > 14$ cm, a tiny bubble formed on top of the inlet at critical values of pressure P_b and air flux Q_b (Figure 5b). The bubble did not evolve through time at a constant inlet flux, although by increasing the inlet flux the size of the bubble increased. This observation, and the fact that we increased the flux slowly, supports the idea that our experiment evolved via equilibrium states. Observations show that the presence of the bubble induced both lateral compaction of the matrix and a gentle lift-up in the centre, generating two steeply dipping reverse shear bands (Figures 4b and 5b) originating on each side of the inlet. The uplift shear zone produces a cone-like structure with an angle $\alpha \sim 65 \pm 6°$ to horizontal. Although there is scattering in the experiments, observations show that α decreases towards the top of the bed into a diverging trumpet-like structure and that the mean angle is positively correlated with the filling height [*Nermoen*, 2006].

[22] When increasing the inlet flux and pressure to values exceeding a second critical threshold (P_f and Q_f), full fluidization of the bed occurred. Full fluidization occurred for all experiments, although the system behaved differently up until fluidization for different filling heights. In the experiments with $h < 14$ cm the transition from diffusive flow to full fluidization occurred directly, without the static bubble phase (such that $Q_b = Q_f$) (Figure 4). In contrast, in the experiments with $h > 14$ cm (Figure 5) the static bubble formed at Q_b, and by increasing the imposed velocity further to Q_f, the bubble rapidly rose to the surface initiating the fluidization. The fluidization morphology is characterized by convective movement where the grains are transported upward together with rapidly ascending gas bubbles in the centre, whilst flowing downward along the sides (Figure 5c and d). Consequently, the lateral sides of the fluidized zone exhibited inward dipping beds (Figure 5d). The fluidization was mainly constrained in-between the pre-existing shear bands imposed by the bubble described above, although some lateral growth of the fluidized zone was observed with time. The ejected material formed a crater at the rim of the fluidized zone as the materials were spewed onto the surface. Due to the (close to) preservation of the dip angle of the shear bands, the diameter of the crater increased with h.

[23] For all the experiments, we plotted P as a function of Q.In experiments with $h < 14$ cm, the relation between the air flux and the pressure was nearly linear before fluidization (Figure 4d).

Subsequently, at the onset of fluidization, the pressure suddenly dropped whereas the flux remained constant (Figure 4d). In experiments with $h > 14$ cm, the evolution of P vs. Q was more complex (Figure 5e). At low fluxes, the relation between the air flux and the pressure was linear. As the flux increased and a static bubble formed, and the pressure values became smaller than the values expected for a linear trend. The size of the bubble increased for increasing air flux, which increased the bulk permeability, and further decreased the pressure measurements. Finally, similarly to the low filling height experiments, at the onset of fluidization the pressure abruptly dropped while the flux remained constant. At fluidization the pressure dropped.

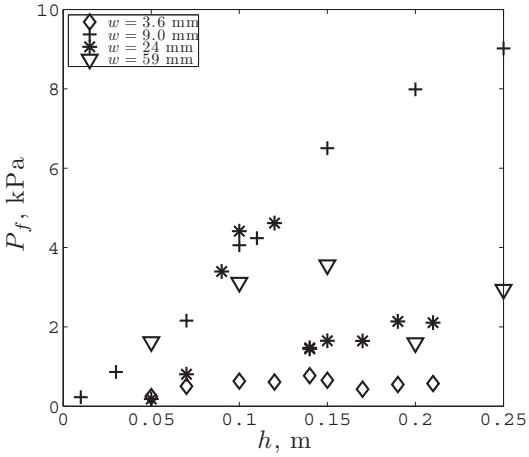

Figure 6. Plot of the measurements of P_f versus the filling height h for all experiments. Scattering is observed within each series. In general, larger filling heights require larger P_f, but there is no clear correlation between P_f and the inlet size w.

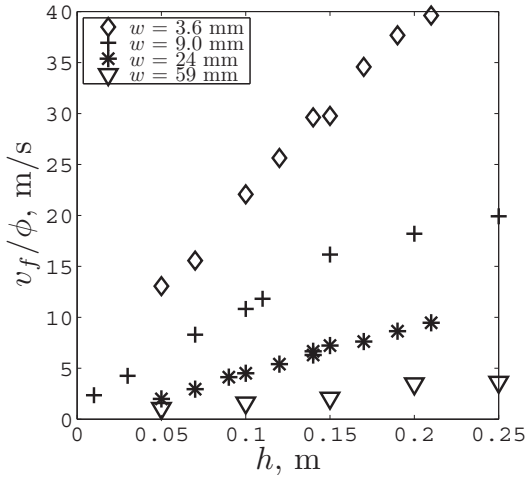

Figure 7. Plot of the critical fluidization velocity v_f/ϕ (in the bed) versus the filling height h for all experiments. A positive correlation is observed for increasing filling height at constant inlet size w. Smaller inlets require larger v_f and vice versa.

[24] By going through the recorded images and selecting the time at which the onset of fluidization occurred, we collected the values of $v_f = Q_f/(wb)$ and P_f for all experiments (see Figure 6 and 7). The experiments were organized into four series corresponding to the inlet widths w. In general, the required critical fluidization velocity increased for the narrower inlet widths and increasing h. Within each series of experiments the fluidization velocities v_f exhibited almost a linear correlation with h. It is important to note that the scaling in the fluidization velocity does not change whether the static stable bubble (observed for $h > 14$ cm) exists or not. This observation indicates that the static bubble phase does not affect the critical conditions for fluidization, which means that the dynamic permeability effects induced by the presence of the bubble plays no major role in the experiment. We will come back to the scaling of v_f in section 4.3. The pressure at fluidization P_f is positively correlated to the filling height except in the case of the smallest inlet $w = 3.6$ mm. We will discuss in detail the use of the pressure measurements in section 4.2.

4. Discussion

4.1. Cohesion Measurements

[25] The glass beads used in the experiment are cohesion-less like dry sand. However, the shear test experiments provided an estimate of $C \sim 65$ Pa, (Figure 3d). This value is high compared with recent cohesion estimates of dry sand where they show that the Mohr-Coulomb envelope bends downward for normal stresses below 200-300 Pa [*Schellart*, 2000; *Mourgues and Cobbold*, 2003]. In our shear tests, the smallest value of normal stress was ~ 700 Pa such that we might have missed this effect. The extrapolation of normal stresses from 700 down to 0 Pa may, therefore, have caused the large errors and the over-estimate of the cohesion value (similarly to *Krantz* [1991]).

4.2. Pressure Measurements

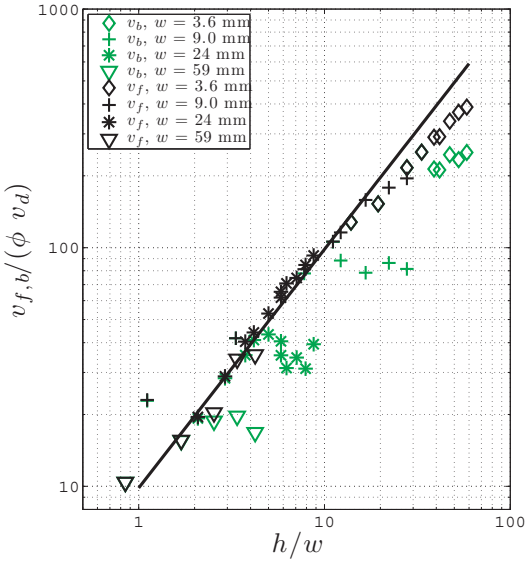

Figure 8. (Color online) Phase diagram for all experiments showing the velocity at fluidization v_f/ϕ (in black) and the bubbling velocity v_b/ϕ (in green/gray) normalized by the intrinsic Darcy velocity v_d versus the aspect ratio h/w. The solid line represents the scaling relation fitted to the measurements of $v_f/(v_d\phi)$ (with the parameters β and ξ).

[26] The evolution of the bulk bed permeability between the inlet and the free surface was captured by the dynamics of the pressure and velocity measurements through Equation (1). We notice that in Figure 4d, the P versus Q curve is linear until fluidization, whereas in Figure 5e the curve bends downward at higher fluxes. We can relate this difference to two effects in the experiment: dynamic pressure and bulk permeability changes caused by grain reorganization.

4.2.1. Dynamic Pressure Effects

[27] The pressure measurements were taken in the T-junction $\sim$10 cm from the inlet (Figure 2). At the T-junction, the inner area of the pipe decreased to $\sim 5\,\mathrm{mm}^2$, while the area of the injection was e.g. $\sim 63\,\mathrm{mm}^2$ for the $w = 9$ mm inlet. Due to flux conservation the flow velocity increased by the ratio of the two areas. At these velocities, Bernoulli's law predicts the increasing importance of the dynamic pressure $P_{dyn} = \rho v_T^2/2$. In Figure 5e the dynamic pressure is subtracted from the Darcian linear trend extrapolated from small velocities. The resulting calculated pressures correspond with the measured pressures at higher imposed velocities (Figure 5e). We can thus infer that for high fluid velocities, the dynamic component of the pressure becomes increasingly important, causing a potential under-estimate of the actual gas pressure above the inlet.

4.2.2. Bulk Permeability effects

[28] During some of the experiments, we often observed abrupt jumps in the pressure measurements synchronously with reorganization of the grains above the inlet (Figure 4d). For a packing of spheres with porosity close to random close packing any reorganization lead to both dilation along shear bands and also potential compaction, which will affect the bulk permeability of the bed.

[29] The experiments with filling heights $h > 14$ cm, the formation of the static bubble above the inlet rearranges the grains such that the bulk permeability between the inlet and the free surface is affected. The bulk permeability is expected to increase because: a) the distance between the tip of the bubble and the surface is reduced compared to the initial distance from the inlet to the surface, b) the permeability in the bubble (free space) is significantly higher than the permeability in the porous packing and c) dilation of the packing occurs along two shear bands originating from the inlet onto the surface at an angle α. As explained in section 3, the geometry and size of the bubble depends on the imposed flux. Increasing in-flux increases the bubble size, with a subsequent increase in the bulk permeability such that the measured pressure decreases further compared to the expected linear trend.

[30] To summarize, the non-linearity of the P versus Q curve is potentially explained by a combination of dynamic pressure effects in the T-junction and the dynamic bulk permeability k increase due to lateral compaction, dilation along the shear bands and the reduced height to the surface from the bubble tip. The measured fluid pressure is thus not a relevant proxy for constraining the physical processes in the experiments. Any variation in k caused by the listed effect resulted in variations in P whilst the flux $v = Q/(wb)$ remained unaffected. Therefore, we will use and discuss v as the controlling parameter for the onset of deformation, similarly to what is done by e.g. *Kunii and Levenspiel* [1969], *Freundt and Bursik* [1998] and *Sparks et al.* [2006].

4.3. Dynamics of Fluidization

[31] In all experiments, two steeply dipping reverse shear bands formed either during the bubble phase or at the onset of fluidization. In Figure 5b, the shear bands are clearly visible due to the deformation of the passive markers. For experiments without the passive markers, shear bands can be seen as brighter zones due to dilation in the packing (Figure 4b). The shear bands accommodated uplift of the bed above the inlet. The force resulting from the injection of the air into the bed exceeded both the weight and the apparent strength of the bed. Similar processes have been observed in other experiments such as e.g. *Walter and Troll* [2001], *Galland et al.* [2007], and *Galland et al.* [2009], who simulated the inflation of shallow magma intrusions in the upper crust.

[32] One might expect that the formation of the static stable bubble affect the dynamics of fluidization. As discussed above, the formation of the bubble modifies the local permeability, and thus the pore pressure distribution. However, we noticed that the existence of the static stable bubble above the inlet at high sediment thickness does not affect the scaling of the fluidization velocity v_f (Figure 6). On that basis we infer that the static bubble forming on top of the inlet prior to fluidization plays a minor role for the critical fluidizationconditions, and we will not consider it in the following analytic development.

4.3.1. Governing Parameters

[33] The relevant parameters in the system were assumed to be the permeability of the bed k, the air viscosity η, the filling height h, the inlet width w, the gravity g, the density of the air ρ_f and the glass beads ρ_s. The cohesion of the bed is assumed negligible in the further discussion due to its relatively low value compared to the weight of the bed, $C \ll ((1-\phi)(\rho_s - \rho_f)gh)$. Thus, we treat the experiments as an example of fluid flow through a cohesion-less density controlled deformable porous media. Dimensional analysis reduces the number of parameters to two dimensionless parameters, h/w and $v_f/(\phi v_d)$, where v_f is the inlet fluid velocity at fluidization (and v_f/ϕ is approximately the gas velocity within the bed) and v_d is the intrinsic Darcy velocity given by the parameters listed above,

$$v_d = \frac{k}{\eta}(1-\phi)(\rho_s - \rho_f)g \simeq 0.11 m/s. \tag{3}$$

[34] By plotting the scaled critical fluidization velocities $v_f/(\phi v_d)$ versus the aspect ratio h/w, we obtain a data collapse of all our measurements onto a master curve (Figure 8). The curve seems to follow a power law of the form,

$$v_f/v_d = \beta \left(\frac{h}{w}\right)^{\xi}, \tag{4}$$

with the parameters $\beta = 12.4 \pm 0.3$ and $\xi = 0.88 \pm 0.03$. No systematic dependency is observed to the existence, or non-existence, of the bubble phase.

[35] A combination of Equation (3) and (4) yielded a semi-empirical expression for the critical velocity,

$$v_f = \phi \frac{k}{\eta}(1-\phi)(\rho_s - \rho_f)g\beta \left(\frac{h}{w}\right)^{\xi}, \tag{5}$$

where, the first part on the right hand side, k/η, corresponds to the diffusivity of the grain packing, i.e. the ability of the fluid to flow through the porous bed. Increasing diffusivity increases the critical velocity at which fluid-induced deformation occurs. The second part of this equation, $(1-\phi)(\rho_s - \rho_f)g$, represents the weight of the bed corrected by buoyancy effects. Decreasing the difference in density between the injected fluid and the bed lowers the critical velocity. The third part of the equation, the aspect ratio $(h/w)^{\xi}$, quantifies the geometrical effect of the setting on the fluidization velocity. Increasing aspect ratio, (the ratio of the sediment thickness to the inlet width) increases the critical fluidization velocity v_f. Finally, β is a constant of proportionality.

4.4. A Lower Bound for v_f

[36] In order to understand and predict the initiation of fluidization and the experimental scaling of $v_f/(\phi v_d)$ we present an analytical model inspired by the minimal velocity of fluidization *Kunii and Levenspiel* [1969]. We evaluate the model predictions with the experimental results of β and ξ. The analytical model setup is shown in Figure 9 and consists of a HS-cell with lateral domain width $2l_x$, filled with a granular media with permeability k and sediment thickness h. A fluid of viscosity η is injected through the bottom at a velocity v_{in} through a central inlet of width w. Above the inlet, we define a truncated wedge that represents the fluidized zone. The

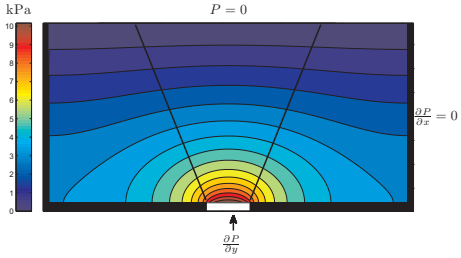

Figure 9. (Color online) Calculated pressure field within the HS-cell. The boundary conditions are: along the top surface $P = 0$, along the two sides we allow no horizontal gradients in the pressure field (i.e. no flux boundaries), and along the bottom we impose a constant influx only through the central inlet $\partial P/\partial y = \eta v_{in}/k\phi = const$ (no vertical flux elsewhere). The plot shown here is of filling height $h = 30$ cm, inlet width $w = 3$ cm and inlet flow velocity $v_{in} = 1$ m/s. The truncated wedge is denoted between the two solid lines originating from the inlet onto the surface at an angle α.

wedge is bounded by two shear planes originating from the inlet sides at an angle α with the horizontal. In the proceeding analysis we make the approximation that the angle α of the initial shear zone is constant throughout the domain and for all filling heights.

[37] Along the lines of *Kunii and Levenspiel* [1969] and *Gidaspow* [1994] the minimum velocity of fluidization is calculated from the quasi-static approximation implying that fluidization occurs when the seepage force F_d equals the buoyant weight of the bed F_g integrated over the whole truncated wedge (see Figure 9). In Appendix A we calculated the pressure field analytically by solving the Laplace equation ($\nabla^2 P = 0$) with boundary conditions similarly to those in the experiment (see Figure 9),

$$P(x,y) = \frac{\eta}{k}\frac{v_{in}}{\phi}\left[\frac{w}{l_x}(h-y) + \sum_{n=1}^{\infty}\frac{2\sin(k_n w/2)}{n\pi k_n \cosh(k_n h)}\cos(k_n x)\sinh(k_n(h- \quad (6)$$

where the origin of the co-ordinate system is placed at the inlet and $k_n = 2n\pi/l_x$. A plot of the 2D pressure field is shown in Figure 9.

[38] The weight of the truncated wedge is estimated by $F_g = (1-\phi)(\rho_s - \rho_f)gV$ with the volume $V = h(w + 2\cot(\alpha))$. The total seepage force transmitted from the fluid onto the solid m atrix can be found by integrating the vertical gradients in the pressure over the total volume V of the truncated wedge,

$$F_d(v_{in}, h, w) = \int \frac{\partial P(x, y, v_{in}, h, w)}{\partial y} dV, \quad (7)$$

where $P(x, y)$ is given in Equation (6). The critical inlet velocity was found by; calculating the y-derivative of the pressure field in equation (6) as a function of the inlet velocity, integrating up $\partial P/\partial y$ throughout the truncated wedge and comparing the weight and the seepage force, and then increasing v_{in} if the integrated value of F_d is lower (or higher) than F_g. At fluidization, we employ the quasi-static approximation, that the total weight and the viscous drag balance out ($F_d = F_g$), such that $v_{in} = v_f$ could be uniquely defined. A systematic use of the procedure above for the experimental variations in h and w, generate the analytic phase diagram shown in red (gray) in Figure 10.

4.4.1. Comparing the experimental and analytic results for $v_f/(\phi v_d)$

[39] In Figure 10 the fluidization velocities obtained from the experimental and the analytic models are plotted together. The results of the analytic model are consistent with the experimental results: an identical trend is observed with similar scaling factors ($\xi_{exp} = 0.88$ versus $\xi_{ana} = 1.02$). However, the analytic model underestimates the experimental results since $\beta_{ana} \simeq 6.8$ while $\beta_{exp} \simeq 12.4$ suggesting that additional effect can be included in the full theoretical analysis. The consistency between the experimental and analytic scaling indicate that the main triggering force for fluidization are the bulk seepage force ($\partial P/\partial y$) integrated over the entire truncated wedge, and not only the pressure at the inlet.

[40] This result, together with the consistency of the scaling of v_f, has implications for interpreting the influence of the static bubble prior to fluidization occurring only in the high filling experiments. The effects of the local dynamic permeability at the bubble are small compared to the forces integrated over the rest of the system. Consequently, the discrepancy between the analytic and experimental models (in Figure 10) cannot be explained by dynamic permeability effects.

[41] The under-estimate in the theoretical prediction could be caused by frictional effects in the experiment causing additional dissipation of the energy imparted to the system by the imposed flow. Examples include friction along the side walls *Janssen* [1895] and shear resistance within the packing. Gas-induced fluidization is defined by the transition from the static solid-like behaviour, where the packing can sustain differential stresses, to a liquid-like behaviour where any non-zero differential stresses induce flow. In weight dominated and cohesion-less systems the shear strength of the material is given by the frictional coefficient and the normal-stress onto a shear plane, $\tau_s = \mu\sigma_n$. The normal stress onto the plane directed in the α direction can be calculated by $\sigma_n = \sigma_v(\kappa \sin^2\alpha + \cos^2\alpha)$, in plane stress conditions where κ is the coefficient of side stresses related to the Poisson ratio by $\kappa = \nu/(1-\nu)$. If now the vertical stress is reduced by the increasing seepage forces driven by the vertical gradients in the pressure field,

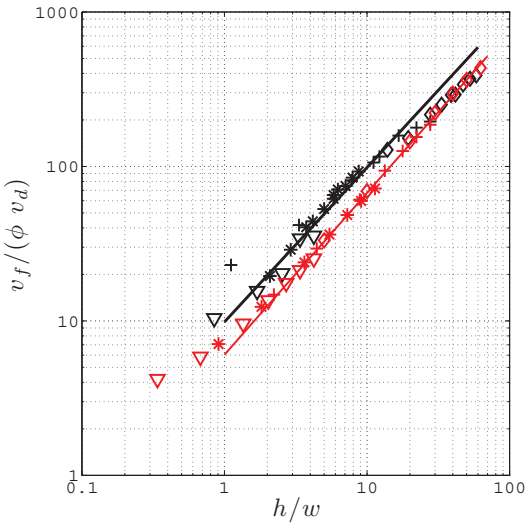

Figure 10. (Color online) Plot of the analytic model of $v_f/(\phi v_d)$ in red (gray) for values of h/w corresponding to those in the experiment (black). The black solid line represents the experimental data of the critical velocity at fluidization plotted in Figure 8 with $\beta_{exp} = 12.4$ and $\xi = 0.88$. In the analytic model the corresponding values are $\beta_{ana} = 6.8$ and $\xi_{ana} = 1.02$.

$$\sigma_v(y) = \int_0^y (\rho_b g - \frac{\partial P}{\partial y})dy, \quad (8)$$

we approach the condition for fluidization when $\sigma_v \rightarrow 0$ which leads to both σ_n and the shear strength $\tau_s \rightarrow 0$. If the shear strength is negligible, that indicates the frictional dissipation within the grain package drops to zero. This, however, is a mean field argument, which does not exclude the existence of local frictional effects still being present within the system. An additional argument is that the planar area, which the shear force acts over at initiation, is small compared to the total system size.

[42] In the experiment the gas is flushed into the cell through the inlet raised 7 cm into the bed. This effect is not taken into account in the analytic boundary conditions where the inlet is placed at the bottom of the cell. This difference could presumably also lead to an under-estimate of the analytic prediction of v_f since the gas can also flow downwards at both sides of the inlet.

4.5. Predicting Critical Fluid Pressures

[43] In the experiment, we controlled the fluid velocity while the pressure measurements varied in response to variations in the bulk permeability caused by deformation of the bed. By dimensional analysis we obtained a data collapse of all critical fluidization velocities onto a master curve. Such a master curve was not obtainable for the critical pressures since the velocity, and not the pressure, was the controlling parameter in the experiments. The pressure dropped abruptly at fluidization such that an uniquely critical pressure could not be defined. However, based on theory [e.g., *Kunii and Levenspiel*, 1969; *Terzaghi*, 1943; *Rozhko et al.*, 2007], experiments [e.g., *Mourgues and Cobbold*, 2003; *Walters et al.*, 2006; *Freundt and Bursik*, 1998; *Sparks et al.*, 2006] and field observations [e.g., *Cobbold and Castro*, 1999; *Jamtveit et al.*, 2004; *Planke et al.*, 2005; *Svensen et al.*, 2006], pore fluid pressure is expected to be the controlling parameter for the formation of piercement structures in geological environments. We will therefore use the analytic model for the pressure field in combination with both the experimental and analytic scaling relation for v_f to predict the critical pressures. Combining the pressure equation in equation (6), the scaling relation in equation (5) and the definition of the Darcian velocity the critical over-pressure above the inlet ($y = x = 0$) is written,

$$P_c^{op} = (\rho_b - \rho_f)g\beta \left(\frac{h}{w}\right)^{\xi} \left[\frac{wh}{l_x} + \sum_{n=1}^{\infty} \frac{2\sin(k_n w)\tanh(k_n h)}{n\pi k_n}\right], \quad (9)$$

where, β and ξ can be replaced by the experimental and analytical values.

[44] In a natural setting there is no lateral box-size l_x such that by letting $l_x \rightarrow \infty$ the sum is replaced by an integral,

$$P_c^{op} = (\rho_b - \rho_f)g\beta \left(\frac{h}{w}\right)^{\xi} \frac{2}{\pi} \int_0^{\infty} \frac{\sin(\tilde{k}w)\tanh(\tilde{k}h)}{\tilde{k}^2} d\tilde{k}. \quad (10)$$

This expression is used to estimate the critical pressure in selected geological settings (see section 4.6). Equation (10) can be interpreted to be a quantification of how the localization of the pressure anomaly effects the critical pressure at fluidization.

[45] By normalizing the over-pressure by the hydrostatic pressure we obtain the definition of the venting number proposed by *Jamtveit et al.* [2004],

$$\begin{aligned} Ve &= \frac{P_c^{op}}{\rho_f g h} \\ &= \frac{\rho_b - \rho_f}{\rho_f}\beta \left(\frac{h}{w}\right)^{\xi} \int_0^{\infty} \frac{2\sin(\tilde{k}w)\tanh(\tilde{k}h)}{\tilde{k}^2} d\tilde{k}, \end{aligned} \quad (11)$$

where the solution of the integral evaluated is evaluated numerically. This relation can be used as a predictive tool to estimate the critical fluid pressures needed to form the piercement structures in geological systems.

4.6. Geological Implications

[46] There are close morphological similarities between our experiments and the piercement structures observed in nature (see the Intro and Figure 1. Some primary similarities are;

1. the apparent conical shape observed in e.g. shallow hydrothermal vents in the Eastern Karoo [*Svensen et al.*, 2006] and kimberlite pipes [*Walters et al.*, 2006] with a dipping angle $\alpha \sim 65^o$;

2. the bedding in the vicinity of the vents exhibit inward dipping structures [e.g., *Walters et al.*, 2006; *Svensen et al.*, 2006].

3. the evidence of intense fluid-assisted deformation within the vents, i.e. brecciation and fluidization.

For these reasons we infer that the experiments simulate the key processes involved in the formation of piercement structures in general. We use equation (10) to obtain crude estimates of critical fluid over-pressures in some selected geological cases.

4.6.1. The Lusi Mud Volcano

[47] *Mazzini et al.* [2007] documented the prehistory and birth of the Lusi mud volcano (East Java, Indonesia). Prior to the eruption, pore pressure data was recorded in a drilling site ∼150 m away of the main eruption site. The origin of the ejected fluids have been estimated by comparing the ejected mud with drilling samples to a depth of $h \sim 1200$ m. At this depth the fluid over-pressure is ∼27 MPa (see Figure 2 in *Mazzini et al.* [2007]).

[48] We can compare this value to the critical pressure estimated from the analytic and experimental models (equation (10)). The missing parameter in the model is the width w of the pressure source. Seismic profiles (see Figure 6A and B in *Mazzini et al.* [2009]) suggest that the Lusi mud volcano is rooted at the top of a diapiric like structure. If we consider the diapir as an effective 'inlet', the parameter w can be taken as the width of the diapir. We assume in the following that $w \simeq 600$ m. By estimating the bulk bed density of the country rock to $\rho_b = 2000$ kg m^{-3} and the mud to $\rho_f = 1200$ kg m^{-3} we find critical fluid over-pressures of 66 MPa and 113 MPa from the analytic and experimental models, respectively (see Table 3). This number is an over-estimate of the measured fluid pressure.

4.6.2. HTVC, Kimberlites and Pockmarks

[49] For the HTVC in the Karoo Basin, the fluids involved in the process are likely to be aqueous fluids with a density of $\rho_f \sim 1000$ kg m^{-3}. The bed density of the country rock can be approximated to $\rho_b \sim 2100$ kg m^{-3}. Typical values extracted from the geological observation are of the order of $h \sim 500$ m and a roughly estimated width of the feeder zone is $w \sim 50$ m [*Svensen et al.*, 2006]. These values provide critical pressure estimates of 84 MPa and 113 MPa from the analytic and experimental models, respectively. Similarly, estimates of P_f for kimberlites and pockmarks with the geometrical assumptions shown in Table 3 are 246 MPa and 1.2 MPa from the analytic model and 364 MPa and 2.1 MPa from the experimental model, respectively. This is consistent with their respective geological settings, as pockmarks are shallower than Witkop II & III vents, which are shallower than the kimberlitic structures. The estimated values of P_f based on both the experiment and analytic prediction are summarized in Table 3.

[50] These values are much larger than the lithostatic stresses at the depth of fluidization (Table 3). This suggests that the models over-estimate the critical fluid pressure. Further experimentation and theoretical modeling needs to be performed in order to better constrain the critical pressures of fluidization.

5. Summary and Conclusion

[51] Piercement structures, such as pockmarks, mud volcanoes, hydrothermal vent complexes and kimberlites, are common features

Table 1. Notation

Variable	Definition	Unit
b	Inlet breadth	[m]
C	Inter particle cohesion	[Pa]
d	Bead diameter	[m]
F_d	Seepage (drag) force	[Pa m^2]
F_g	Buoyant weight	[Pa m^2]
F_s	Integrated shear force	[Pa m^2]
g	Constant of gravity	[m s^{-2}]
h	Bed filling height	[m]
k	Bed permeability	[m^2]
P	Fluid pressure	[Pa]
P_d	Dynamic pressure	[Pa]
P_f, P_f	Pressure at fluidization / bubbling	[Pa]
P^{op}	Fluid over-pressure	[Pa]
P^{hyd}	Hydrostatic pressure	[Pa]
Q	Inlet air flux	[m^3 s^{-1}]
Q_f, Q_b	Air flux (fluidization / bubbling)	[m^3 s^{-1}]
v_f, v_b	Critical inlet air velocity at fluidization and bubbling	[m s^{-1}]
v_d	Darcian velocity (in the bed)	[m s^{-1}]
v_{in}	Inlet air velocity	[m s^{-1}]
Ve	Venting number	[1]
w	Inlet width	[m]
α	Angle of shear zone	[°]
$\beta_{ana,exp}$	Constant of proportionality in equation (4)	[1]
η	Air viscosity	[Pa s]
γ	Internal angle of friction	[°]
ϕ	Porosity	[1]
κ	Coefficient of side stresses	[1]
μ	Frictional coefficient	[1]
ρ_f	Air density	[kg m^{-3}]
ρ_b	Bed density	[kg m^{-3}]
ρ_g	Glass density	[kg m^{-3}]
σ	Normal stress	[Pa]
τ	Shear stress	[Pa]
ξ	Power law exponent in equation (4)	[1]

on earth. These structures form in response to the build-up of fluid pressures at depth. The goal of this work was to predict the conditions at which piercement structures form in general.

[52] We designed an experimental setup to study fluidization processes. The setup consisted of a vertically oriented Hele-Shaw cell filled with glass beads, in which compressed air was injected. We varied the inlet width w and depth h. Our main conclusions from the experiments are:

1. At a critical air velocity, fluidization occurred within a cone, with morphological characteristics similar to those observed in nature.

2. The inlet velocity is the main proxy for initiation of fluidization in the presented experiments. Our results show that $v_f/(\phi v_d)$ almost scales linearly with h/w.

[53] We proposed an analytic model for v_f defined when the weight is balanced by the seepage force integrated over the fluidized zone. The main conclusions from the analytic model are:

1. The model predicts the scaling observed in the experiments between v_f and h/w.

2. The analytical model under-estimates the experimental results. This discrepancy could be related to the artificial constraints imposed by the walls of the HS-cell, localized frictional effects at fluidization , the position of the inlet, and turbulence effects leading to non-linear seepage forces.

[54] In geological systems the pore fluid pressure is commonly used as the primary proxy for fluid-induced deformation, fluidization and the formation of the piercement structures in general. By converting the critical velocities obtained from the models, we derived an analytical equation for the critical pressure for fluidization. We employed this expression to a variety of geological settings such as pockmarks, mud volcanoes, hydrothermal vent complexes and kimberlites. The values obtained from the model seem to overestimate the critical pressures, notably so at the Lusi mud volcano (Indonesia) where the pore fluid pressures were measured prior to the eruption.

Table 2. Table of the measurements of the critical pressures P_f and critical flow velocities v_c at the onset of fluidization for the given filling height h and inlet width w.

Exp	w, mm	h, cm	v_c, ms^{-1}	P_f, Pa
1	3.6	5	5.6	244
2	3.6	7	6.7	2032
3	3.6	10	9.5	633
4	3.6	12	9.3	609
5	3.6	14	12.7	3246
6	3.6	15	12.8	2674
7	3.6	17	14.9	431
8	3.6	19	16.2	548
9	3.6	21	17.0	573
10	9.0	1	0.9	183
11	9.0	3	1.6	805
12	9.0	7	3.0	3395
13	9.0	10	4.0	3981
14	9.0	11	4.3	4411
15	9.0	15	5.9	6981
16	9.0	20	6.6	8023
17	9.0	25	7.2	9047
18	24	5	0.7	340
19	24	7	1.1	951
20	24	9	1.5	3328
21	24	10	1.7	4451
22	24	12	2.0	4768
23	24	14	2.2	4216
24	24	14	2.5	8689
25	24	14	2.3	8720
26	24	15	2.7	9872
27	24	17	2.8	9735
28	24	19	3.2	12831
29	24	21	3.5	12610
30	59	5	0.4	1924
31	59	10	0.6	3056
32	59	15	0.8	5403
33	59	20	1.3	9312
34	59	25	1.3	17250

Table 3. Example of estimated critical pressures in some selected geological cases using equation (10) and the experimental and analytic values of β and ξ. We use data for the Lusi mud volcano from [*Mazzini et al.*, 2007]; Pockmarks from [*Hammer*, 2008]; Witkop II & III hydrothermal vent complexes from [*Svensen et al.*, 2006]; and Kimberlites from [*Lorenz and Kurszlaukis*, 2007]. The input values are rough order of magnitude estimates which will vary significantly from case to case. The estimate of P_f fits within order magnitude to the experiments ($\sim$ 10 kPa in the experiment) but over-estimates the measured pore fluid pressure prior to eruption for the Lusi mud volcano (27 MPa see Figure 2 in *Mazzini et al.* [2007]).

Setting	ρ_f	ρ_b	h	w	$P_{f,mod}$	$P_{f,exp}$	P_{lith}	
Lusi	1200	2100	1200	600	66.3 MPa	113 MPa	24 MPa	W
Pockmarks	1000	1700	30	30	1.2 MPa	2.1 MPa	0.5 MPa	
Witkop II & III	1000	2100	500	50	84 MPa	113 MPa	10 MPa	
Kimberlites	1500	2500	2000	400	246 MPa	364 MPa	49 MPa	
Experiments	1.3	1540	0.1	0.024	17 kPa	26 kPa	1.5 kPa	

Appendix A: Calculating $P(x, y)$

[55] In the appendix we sketch the derivation of the pressure field used in equation (6) calculated from the Laplace equation $\nabla^2 P = 0$ with the boundary conditions noted in Figure 9. First assume that the pressure can be written as a product of two functions $P = e(x)f(y)$, such that by using the Laplace equation,

$$\frac{1}{e}\frac{\partial^2 e}{\partial x^2} = -\frac{1}{f}\frac{\partial^2 f}{\partial y^2} = -k^2, \tag{A1}$$

Table 4. Table of the experimentally measured variables.

Variable	Value
μ	0.37
C	64 Pa
α	70±5°
γ	20±1°
ϕ	37%
η	$1.76 \cdot 10^{-5}$ Pa s
k	$1.2 \cdot 10^{-10}$ m^2
ρ_s	2450 kg m^{-3}
ρ_f	1.3 kg m^{-3}
d	280 μm
b	0.7 cm
β_{exp}	12.4
ξ_{exp}	0.88
β_{ana}	6.8
ξ_{ana}	1.02

since e is only a function of x and f is only a function of y implies that k is constant, such that,

$$\frac{\partial^2}{\partial x^2}e = -k^2 e \tag{A2}$$

$$\frac{\partial^2}{\partial y^2}f = k^2 f \tag{A3}$$

Which has the basic solutions $e_1 = \sin(kx)$, $e_2 = \cos(kx)$, $f_1 = \exp(ky)$ and $f_2 = \exp(-ky)$, where $k > 0$. The $k = 0$-term is treated separately. Now since the left and right side walls have zero flux conditions, i.e. $\partial P/\partial x = 0$ at $x = 0$, from this we can omit the e_1-solution. We find k by evaluating $\partial e/\partial x = -k\sin(kx) = 0$ at $x = \tilde{l}_x$ which is satisfied only if $k_n = n\pi/\tilde{l}_x$.

[56] For $k = 0$ equation (A1) reads,

$$\frac{\partial^2 e}{\partial x^2} = 0 = \frac{\partial^2 f}{\partial y^2} \tag{A4}$$

which shows that $e(x)$ and $f(y)$ are linear functions in x and y respectively. Inserting the right and left hand boundary conditions we note that $e(x)$ is constant.

[57] The general solution of the Laplace equation with zero flux at the left and right hand boundaries is the linear combination of the above derived basic solutions,

$$P(x,y) = a_0 y + b_0 + \sum_{n=1}^{\infty} \cos(k_n x)\left(a_n \exp(k_n y) + b_n \exp(-k_n y)\right). \tag{A5}$$

On the top boundary, $y = h$, we impose zero pressure. Since this is valid for all x we get,

$$a_n \exp(k_n y) + b_n \exp(-k_n y) = 0, \text{ for all } n \geq 1 \tag{A6}$$

$$a_0 y + b_0 = 0, \tag{A7}$$

and we obtain the solution

$$P(x,y) = c(h-y) + \sum_{n=1}^{\infty} d_n \cos(k_n x)\sinh(k_n(h-y)) \tag{A8}$$

where $d_n = -2a_n \exp(kh)$.

[58] Until now we have not used the bottom boundary condition such that both c and d_n are still unconstrained. The full solution of the pressure equation is obtained by considering the bottom boundary condition $g(x)$.

[59] Consider the case,

$$\frac{\partial}{\partial y}P(x, y=0) = g(x) = \begin{cases} \frac{\eta}{k}\frac{v_{in}}{\phi} & \text{if } 0 < x < \tilde{w} = w/2 \\ 0 & \text{if } \tilde{w} < x < \tilde{l}_x = l_x/2 \end{cases} \tag{A9}$$

when the origin of the co-ordinate system is placed on top of the inlet. We now want to express this condition as a cosine expansion,

$$g(x) = \sum_{n=0}^{\infty} c_n \cos(k_n x). \tag{A10}$$

The coefficients in the cosine expansion are found by using the orthogonality of the basis functions,

$$\int_0^1 \cos(n\pi u)\cos(m\pi u)du = \frac{1}{2}\delta_{n,m}, \tag{A11}$$

where $\delta_{n,m}$ is the Kronecker delta function. Equation (A10) is multiplied by $\cos(k_m x)$ and integrated from $x = 0$ to $x = \tilde{l}_x$, and by using that $g(x) = \frac{\eta}{k}\frac{v_{in}}{\phi}$ up to $\tilde{w}$ and zero elsewhere, we obtain

$$\frac{\eta}{k}\frac{v_{in}}{\phi}\int_0^{\tilde{w}} \cos(k_m x)dx = \sum_{n=0}^{\infty} c_n \int_0^{\tilde{l}_x} \cos(k_n x)\cos(k_m x)dx, \tag{A12}$$

so that,

$$\frac{\eta}{k}\frac{v_{in}}{\phi}\frac{\sin k_m \tilde{w}}{k_m} = \frac{1}{2}\sum_{n=0}^{\infty} c_n \tilde{l}_x \delta_{n,m} = \frac{1}{2}c_m \tilde{l}_x \tag{A13}$$

After inserting for the expression for $\tilde{l}_x$ and and $\tilde{w}$ we get

$$c_0 = \frac{\eta}{k}\frac{v_{in}}{\phi}\frac{w}{l_x} \tag{A14}$$

$$c_{n\geq 1} = 2\frac{\eta}{k}\frac{v_{in}}{\phi}\frac{\sin(k_n w/2)}{\pi n}. \tag{A15}$$

Comparing the cosine expansion of $g(x)$ and $(\partial P/\partial y)$ evaluated at $(x, y = 0)$ we obtain that

$$-c = c_0 \tag{A16}$$

$$-d_n \cosh(k_n h)k_n = c_n \text{ , for } n \geq 1. \tag{A17}$$

Inserting the above coefficients into the equation (A8) we obtain the analytic solution of the pressure,

$$P(x,y) = \frac{\eta}{k}\frac{v_{in}}{\phi}\cdot \left[\frac{w}{l_x}(y-h) - \sum_{n=1}^{\infty}\frac{2\sin(k_n w/2)}{n\pi k_n \cosh(k_n h)}\cos(k_n x)\sinh(k_n(h-y))\right],$$

where $k_n = n\pi/\tilde{l}_x = 2n\pi/l_x$.

Acknowledgments. [61] The study was supported by grants from the Norwegian Research Council to B. Jamtveit, A. Malthe-Sørenssen, and H. Svensen through a Centre of Excellence and PetroMaks grant to Physics of Geological Processes (PGP). We have benefited from fruitful discussions from our colleagues of PGP, especially Dag K. Dysthe, Simen Bræck, Sean Hutton, Simon D. deVilliers, Øyvind Hammer, Galen Gisler and Adriano Mazzini. Two anonymous reviewers are thanked for their insightful and valuable input improving the quality of the article.

References

www.beijer.no.

Bernal, J. D., and J. Mason (1960), Co-ordination of randomly packed spheres, *Nature*, *188*, 910–911.

Carman, P. C. (1937), Fluid flow through granular beds, *Trans. Inst. Chem.*, *15*, 150.

Chauveau, B., and E. Kaminski (2008), Porous compaction in transient creep regime and implications for melt, petroleum, and CO2 circulation, *JOURNAL OF GEOPHYSICAL RESEARCH-SOLID EARTH*, *113*(B9), doi:10.1029/2007JB005088.

Clement, C. R. (1975), The emplacement of some diatreme facies kimberlites, *Phys. and Chem. of the Earth*, *9*, 51–59.

Cobbold, P., and L. Castro (1999), Fluid pressure and effective stress in sandbox modelling, *Tectonophysics*, *301*, 1–19.

Cobbold, P. R., and N. Rodrigues (2007), Seepage forces, important factors in the formation of horizontal hydraulic fractures and bedding-parallel fibrous veins (’beef’ and ’cone-in-cone’), *Geofl.*, *7*, 313–322.

Connolly, J., and Y. Podladchikov (1998), Compaction-driven fluid flow in viscoelastic rock, *GEODINAMICA ACTA*, *11*(2-3), 55–84.

Cox, S. F. (2005), *Coupling between deformation, fluid pressures, and fluid flow in ore-producing hydrothermal systems at depth in the crust*, pp. 39–75, Soc. of Econ. Geol., Littleton, Colorado.

de Gennes, P. G. (1999), Granular matter: a tentative view, *Rev. Mod. Phys.*, *71*, 374–382.

Dimitrov, L. I. (2002), Mud volcanoes - the most important pathway for degassing deeply buried sediments, *Earth-Sci. Rev.*, *59*, 49–76.

Dudukovic, M. P., F. Larachi, and P. L. Mills (1999), Multiphase reactors - revisited, *Chem. Eng. Sci.*, *54*, 1979–1995.

Freundt, A., and M. Bursik (1998), Pyroclastic density currents. J.S. Gilbert, R.S.J. Sparks (eds.), *The Physics of Explosive Volcanic Eruptions, Geol. soc. London Spec. Publ.*, *145*, 145–182.

Galland, O., P. Cobbold, J. B. d’Ars, and E. Hallot (2007), Mechanical interactions between compressional tectonics and magmatism: constraints by analogue modelling, *J. of Geoph. Res.*, *112*, doi:10.1029/2006JB004604, b06402.

Galland, O., S. Planke, E.-R. Neumann, and A. Malthe-Sorenssen (2009), Experimental modelling of shallow magma emplacement: Application to saucer-shaped intrusions, *Earth and Planetary Science Letters*, *277*(3-4), 373–383, doi:10.1016/j.epsl.2008.11.003.

Gidaspow, D. (1994), *Multiphase flow and fluidization*, Academic Press, INC.

Gittings, M. L., R. P. Weaver, M. Clover, T. Betlach, N. Byrne, and *et. al.* (2006), The rage radiation-hydrodynamic code, *Los Alamos unclassif. Rep.*, lA-UR.06-0027.

Hammer, O. . (2008), pers. Comm.

Hansen, D. M. (2006), The morphology of intrusion-related vent structures and their implications for constraining the timing of intrusive events along the NE Atlantic margin, *J. Geol. Soc. London*, *163*, 789–800.

Harrington, P. K. (1985), Formation of pockmarks by pore-water escape, *Geo.-Mar. Lett.*, *5*, 193–197.

Hirata, T. (1998), Fracturing due to fluid intrusion into viscoelastic materials, *Physical Review E*, *57*(2, Part A), 1772–1779.

Hovland, M., M. Talbot, S. Olaussen, and L. Aasberg (1985), Recently formed methane-derived carbonates from the North Sea floor, *In: Thomas, B.M. (Ed.), Petroleum Geochemsitry in Exploration of the Norwegian Shelf. Norwegian Petrol. Soc. Graham & Trottman*, pp. 263–266.

Hovland, M., M. Talbot, H. Qvale, S. Olaussen, and L. Aasberg (1987), Methane-related carbonate cements in pockmarks of the North Sea, *J. Sed. Petrol.*, *88*, 881–892.

Hubbert, M. (1951), Mechanical basis for certain familiar geologic structures, *Geol. Soc. of Amer. Bull.*, *62*, 355–372.

Jaeger, H. M., and S. R. Nagel (1992), Physics of the granular state, *Science*, *255*(1523).

Jaeger, H. M., S. R. Nagel, and R. P. Behringer (1996), Granular solids, liquids and gases, *Rev. of Mod. Phys.*, *68(4)*, 1259–1273.

Jakubov, A. A., A. A. Ali-Zade, and M. M. Zeinalov (1971), Mud volcanoes of the Azerbaijan SSR, Atlas (in Russian), *Azerbaijan Acad. of Sci., Baku*.

Jamtveit, B., H. Svensen, Y. Podladchikov, and S. Planke (2004), Hydrothermal vent complexes associated with sill intrusions in sedimentary basins, *Geol. Soc. London*, *234*, 233–241.

Janssen, H. A. (1895), Versuche uber getreidedruck in Silozellen, *Zeitschr. d. Vereines deutscher Ingenieure*, *39(35)*, 1045–1049.

Jensen, J. B., A. Kuijpers, O. Bennike, T. Laier, and F. Werner (2002), New geological aspects for freshwater seepage and formation in Eckerførde Bay, western Baltic, *Cont. Shelf. Res.*, *22*, 2159–2173.

Johansen, O. ., R. Toussaint, K. J. M. løy, E. G. F. y, and J. Shmittbuhl (2008), Coupled air/granular flow in a linear Hele-Shaw cell, *Phys. Rev. E*, *77*, 011,301, dOI: 10.1103/PhysRevE.77.011301.

Karpen, V., L. Thomsn, and E. Suess (2006), Groundwater discharges in the Baltic Sea: survey and quantification using a schlieren technique application, *Geofluids*, *6*, 241–250.

Krantz, R. W. (1991), Measurements of friction coefficients and cohesion for faulting and fault reactivation in laboratory models using sand and sand mixtures, *Tectonophys.*, *188*, 203–207.

Kunii, D., and O. Levenspiel (1969), *Fluidization Engineering*, Wiley and Sons, New York.

Labview, http://www.ni.com/labview/.

Lancelot, Y., and R. W. Embley (1977), Piercement structures in deep oceans, *The Am. Assoc. of Pet. Geol. Bull.*, *61*(11), 1991–2000.

Lebron, I., and D. A. Robinson (2003), Particle size segregation during hand packing of coarse granular materials and impacts on local pore-scale structure, *Vadose Zone Journal*, *2*, 330–337.

Lemaire, E., P. Levitz, G. Daccord, and H. Vandamme (1991), From viscous fingering to viscoelastic fracturing in colloidal fluids, *Physical Review Letters*, *67*(15), 2009–2012.

Lorenz, V. (1975), Formation of phreatomagmatic maar-diatreme volcanoes and its relevance to kimberlite diatremes, *Phys. and Chem. of the Earth*, pp. 17–29.

Lorenz, V., and S. Kurszlaukis (2007), Root zone processes in the phreatomagmatic pipe emplacement model and consequences for the evolution of maar-diatreme volcanoes, *J. of Volc. and Geotherm.l Res.*, *159*, 4–32.

Mazzini, A., H. Svensen, G. G. Akhmanov, G. Aloisi, S. Planke, A. M.-S. renssen, and B. Istadi (2007), Triggering and dynamic evolution of the Lusi mud volcano, Indonesia, *Earth and Plan. Sci. Lett.*, *261*, 375–388.

Mazzini, A., A. Nermoen, M. Krotkiewski, Y. Podladchikov, H. Svensen, and S. Planke (2008), Fault shearing as efficient mechanism for overpressure release to trigger the Lusi mud volcano, Indonesia, *Marine and Pet. Geol.*, submitted.

Mazzini, A., A. Nermoen, M. Krotkiewski, Y. Podladchikov, S. Planke, and H. Svensen (2009), Strike-slip faulting as a trigger mechanism for overpressure release through piercement structures. Implications for the Lusi mud volcano, Indonesia, *Marine and Petroleum Geology*, *26*(9), 1751–1765, doi:10.1016/j.marpetgeo.2009.03.001.

Moss, J., and J. Cartwright (2010), The spatial and temporal distribution of pipe formation, offshore Namibia , *Marine and Petroleum Geology*, doi:10.1016/j.martpetgeo.2009.12.013, Article in press.

Mourgues, R., and P. R. Cobbold (2003), Some tectonic consequenses of fluid overpressures and seepage forces as demonstrated by sandbox modelling, *Tectonophysics*, *376*, 75–97.

Nermoen, A. (2006), Piercement structures in granular media, Master Thesis, http://folk.uio.no/anderne/Masterthesis.pdf.

Paterson, M. S., and T.-F. Wong (2006), *Experimental rock deformation: The brittle field*, 346 pp., Springer, Berlin.

Planke, S., H. Svensen, M. Hovland, D. A. Banks, and B. Jamtveit (2003), Mud and fluid migration in active mud volcanoes in Azerbaijan, *Geo-Marine Lett.*, *23*, 258–268.

Planke, S., T. Rasmussen, S. S. Rey, and R. Myklebust (2005), Seismic characteristics and distribution of volcanic intrusions and hydrothermal vent complexes in the Vøring and Møre basins, *Geol. Soc. London*.

Rigord, P., A. Guarino, V. Vidal, and J. C. Géminard (2005), Localized instability of a granular layer submitted to an ascending liquid flow, *Granular Matter*, *7*, 191–197.

Rozhko, A. Y., Y. Podladchikov, and F. Renard (2007), Failure patterns caused by localized rise in pore-fluid overpressure and effective strength of rocks, *Geophys. Res. Lett.*, *34*, doi:10.1029/2007GL031696.

Schellart, W. P. (2000), Shear test results for cohesion and friction coefficients for different materials: scaling implications for their usage in analogue modelling, *Tectonophys.*, *324*, 1–16.

Sibson, R. H. (2003), Brittle-failure controls on maximum sustainable overpressure in different tectonic regimes, *AAPG Bulletin*, *87*, 901–908.

Sparks, R. S. J., L. Baker, R. J. Brown, M. Field, J. Schumacher, G. Stripp, and A. L. Walters (2006), Dynamcial constraints on kimberlite volcanism, *J. of Volc. and Geotherm. Res.*, *155*, 18–48.

Svensen, H., S. Planke, A. M.-S. renssen, B. Jamtveit, R. Myklebust, T. R. Eidem, and S. S. Rey (2004), Release of methane from a volcanic basin as a mechanism initial Eocene global warming, *Nature*, *429*, 542–545.

Svensen, H., B. Jamtveit, S. Planke, and L. Chevallier (2006), Structure and evolution of hydrothermal vent complexes in the Karoo basin, South Africa, *J. Geol. Soc. London*, *163*, 671–682.

Svensen, H., D. A. Karlsen, A. Struz, K. Backer-Owe, D. A. Banks, and S. Planke (2007a), Processes controlling water and hydrocarbon composition in seeps from the Salton Sea geothermal system, California, USA, *Geology*, *35*, 85–88, doi:10.1130/G23101A.1.

Svensen, H., S. Planke, L. Chevallier, A. M.-S. renssen, F. Corfu, and B. Jamtveit (2007b), Hydrothermal venting of greenhouse gases triggering Early Jurassic global warming, *Earth Planet. Sci. Lett.*, *256*, 554–566.

Terzaghi, K. (1943), *Theoretical soil mechanics*, 528 pp., John Wiley and Sons, New York.

Walter, T. R., and V. R. Troll (2001), Formation of caldera periphery faults: an experimental study, *Bulletin of Volc.*, *65*(2-3), 191–203.

Walters, A. L., J. Phillips, R. J. Brown, M. Field, T. Gernon, G. Stripp, and R. S. J. Sparks (2006), The role of fluidisation in the formation of volcaniclastic kimberlite: Grain size observations and experimental investigation, *J. of Volc. and Geotherm. Res.*, *155*, 119–137.

Wilhelm, T. (2000), Piping in saturated granular media, Ph.D. thesis, Leopold-Franzens-Universitat Innsbruck.

Woolsey, T. S., M. E. Macallum, and S. A. Schumm (1975), Modelling of diatreme emplacement by fluidization, *Phys. Chem. of the Earth*, *9*, 29–45.

Anders Nermoen, Physics of Geological Processes, University of Oslo, Sem Selands vei 24, NO-0316 Oslo, Norway, Email: anderne@fys.uio.no

Paper III

Strike-slip Faulting as a Trigger Mechanism for Overpressure Release Through Piercement Structures. Implications for the Lusi Mud Volcano, Indonesia

Adriano Mazzini, Anders Nermoen, Marcin Krotkiewski, Yuri Y. Podladchikov, Sverre Planke, Henrik Svensen

Marine and Petroleum Geology 26 (2009) 1751-1765

Paper IV

Complex Plumbing Systems in the Near Subsurface: Geometries of Authigenic Carbonates from Dogolovskoy Mound (Black Sea) Constrained by Analogue Experiments

Adriano Mazzini, Michael K. Ivanov, Anders Nermoen, Andre Bahr, Gerhard Bohrmann, Henrik Svensen, Sverre Planke

Marine and Petroleum Geology 25 (2008) 457-472
